KfK 5067
Dezember 1992

# Neutron Capture in $^{148,150}$Sm: A Sensitive Probe of the s-Process Neutron Density

K. Wisshak, K. Guber, F. Voß, F. Käppeler, G. Reffo
Institut für Kernphysik

Kernforschungszentrum Karlsruhe

KERNFORSCHUNGSZENTRUM KARLSRUHE
Institut für Kernphysik

KfK 5067

# NEUTRON CAPTURE IN $^{148,150}$Sm: A SENSITIVE PROBE OF THE s-PROCESS NEUTRON DENSITY.

K. Wisshak, K. Guber, F. Voß, F. Käppeler, and G. Reffo*

*Permanent address: E.N.E.A. Bologna, Viale Ercolani 8, I-40138 Bologna, Italy

Kernforschungszentrum Karlsruhe GmbH, Karlsruhe

Kernforschungszentrum Karlsruhe GmbH
Postfach 3640, 7500 Karlsruhe 1

ISSN 0303-4003

## ABSTRACT

The neutron capture cross sections of $^{147,148,149,150,152}$Sm were measured in the energy range from 3 to 225 keV at the Karlsruhe Van de Graaff accelerator using gold as a standard. Neutrons were produced via the $^{7}$Li(p,n)$^{7}$Be reaction by bombarding metallic Li targets with a pulsed proton beam. Capture events were registered with the Karlsruhe $4\pi$ Barium Fluoride Detector. Several runs have been performed under different experimental conditions to study the systematic uncertainties in detail. For the first time, data were recorded with an ADC system that allows to register gamma-ray energy and time-of-flight of the individual detector modules. The cross section ratios were determined with an overall uncertainty of ~1 %. This is an improvement by about a factor of five compared to the existing data. Severe discrepancies were found to the results of previous measurements.

Maxwellian averaged neutron capture cross sections were calculated for thermal energies between kT = 10 to 100 keV by normalizing the cross section shape up to 700 keV neutron energy reported in literature to the present data. These stellar cross sections were used in an s-process analysis. The ratio of the values of the s-process current $\langle\sigma\rangle N_s$ (Maxwellian-averaged neutron capture cross section times s-process abundance) for the s-only isotopes $^{148,150}$Sm is 0.882±0.009 rather than unity as expected by the local approximation. The corresponding branching in the s-process path is analysed in the framework of the classical approach. The resulting mean neutron density, $n_n = 3.4 \pm 0.6 \times 10^8$ cm$^{-3}$, is the most stringent limit obtained so far. Finally the new cross sections are used to derive constraints for a stellar model.

## ZUSAMMENFASSUNG

NEUTRONENEINFANG IN $^{148,150}$Sm: EIN EMPFINDLICHER INDIKATOR FÜR DIE NEUTRONENDICHTE IM s-PROZESS

Die Neutroneneinfangquerschnitte von $^{147,148,149,150,152}$Sm wurden im Energiebereich von 3 bis 225 keV am Karlsruher Van de Graaff Beschleuniger relativ zu Gold als Standard bestimmt. Neutronen wurden über die $^{7}$Li(p,n)$^{7}$Be-Reaktion durch Beschuß metallischer Li-Targets mit einem gepulsten Protonenstrahl erzeugt. Einfangereignisse wurden mit dem Karlsruher $4\pi$ Barium Fluorid Detektor nachgewiesen. Die Messung wurde unter verschiedenen experimentellen Bedingungen durchgeführt, um systematische Unsicherheiten detailliert zu untersuchen. Zum ersten Mal wurde ein ADC-System bei der Datenaufnahme verwendet, mit dem die Gamma-Energie und die Flugzeit der einzelnen Detektor-Module aufgezeichnet werden kann. Die Verhältnisse der Wirkungsquerschnitte wurden mit einer Gesamtunsicherheit von ~1 % bestimmt. Dies bedeutet eine Verbesserung um einen Faktor fünf im Vergleich zu den existierenden Daten.

Die stellaren Einfangquerschnitte wurden für thermische Energien von kT=10 bis 100 keV berechnet. Dazu wurde der Verlauf des Wirkungsquerschnitts bis 700 keV Neutronenenergie, wie er aus der Literatur bekannt ist, auf die vorliegenden Daten normiert. Diese Ergebnisse wurden für eine genauere Untersuchung des s-Prozesses verwendet. Für das Verhältnis des s-Prozeß-Flusses, $\langle\sigma\rangle N_s$ (Maxwell gemittelter Wirkungsquerschnitt mal s-Prozeß Häufigkeit), ergab sich für die reinen s-Kerne $^{148}$Sm und $^{150}$Sm ein Wert von 0.882±0.009 . Dieser Abweichung von der lokalen Approximation entspricht eine Verzweigung des s-Prozeß Pfades, die im Rahmen der klassischen Methode analysiert wurde. Diese Analyse liefert eine mittlere Neutronendichte von $n_n = 3.4 \pm 0.6 \times 10^8$ cm$^{-3}$. Dies ist die bisher genaueste Eingrenzung. Die neuen Querschnitte wurden ausserdem verwendet, um die Vorhersagen eines stellaren Modells zu diskutieren.

CONTENTS

## I. INTRODUCTION

The simultaneous availability of an improved setup for the accurate determination of neutron capture cross sections [1,2] and refined stellar model descriptions [3,4] make studies of the synthesis of heavy elements in the so called s- (slow neutron capture) process a promising tool for the diagnostics of the stellar plasma of Red Giant stars. The analysis and interpretation of the isotopic pattern of the observed solar system abundances may yield the physical conditions during the s-process, that is temperature, neutron density and matter density [5].

A first experiment on tellurium isotopes [6] confirmed the old prediction for the s-process by Clayton et al. [7] of a 'local approximation' (that the product of neutron capture cross section $\langle\sigma\rangle$ and s-process abundance $N_s$ is constant for neighboring isotopes) with an uncertainty of ~1 %. This result strongly supports the idea to interpret (mostly small) deviations from this behaviour as branchings in the neutron capture path of the s-process. It is the analysis of such branchings that yields information on the physical conditions during the s-process [5,6].

A prominent example is the branching in the samarium region that is illustrated in Fig. 1. Neutron capture in the unstable isotopes $^{147}$Nd and $^{147,148,149}$Pm causes a small part of the s-process flow to bypass $^{148}$Sm. This implies that the ratio $N_s\langle\sigma\rangle(^{148}\mathrm{Sm})/N_s\langle\sigma\rangle(^{150}\mathrm{Sm})$ is slightly lower than unity, an effect that is determined mainly by the neutron density. It is obvious that a small deviation from unity can be determined reliably only if the respective cross sections $\langle\sigma\rangle$ and abundances $N_s$ of $^{148}$Sm and $^{150}$Sm are known with sufficient accuracy. As can be seen from Fig. 1, $^{148}$Sm and $^{150}$Sm are s-only isotopes since they are shielded from contributions of the r-process by their stable neodymium isobars. Thus the abundance ratio $N_s(^{148}\mathrm{Sm})/N_s(^{150}\mathrm{Sm})$ is identical to the isotopic ratio that is known to a precision of 0.1 % [8]. Consequently, it is the uncertainty in the cross section ratio $\langle\sigma\rangle(^{148}\mathrm{Sm})/\langle\sigma\rangle(^{150}\mathrm{Sm})$, which determines the accuracy by which the s-process flow and, hence, the neutron density can be determined.

A detailed discussion of this branching was given by Winters et al. in 1986 [9]. In their work, the cross section ratio was determined with an uncertainty of ~4 % resulting in an estimated strength for the neutron density of $(3.0 \pm 1.2)\times 10^8$ cm$^{-3}$. The new experimental setup established at the Karlsruhe 3.75 MV Van de Graaff accelerator allows to determine

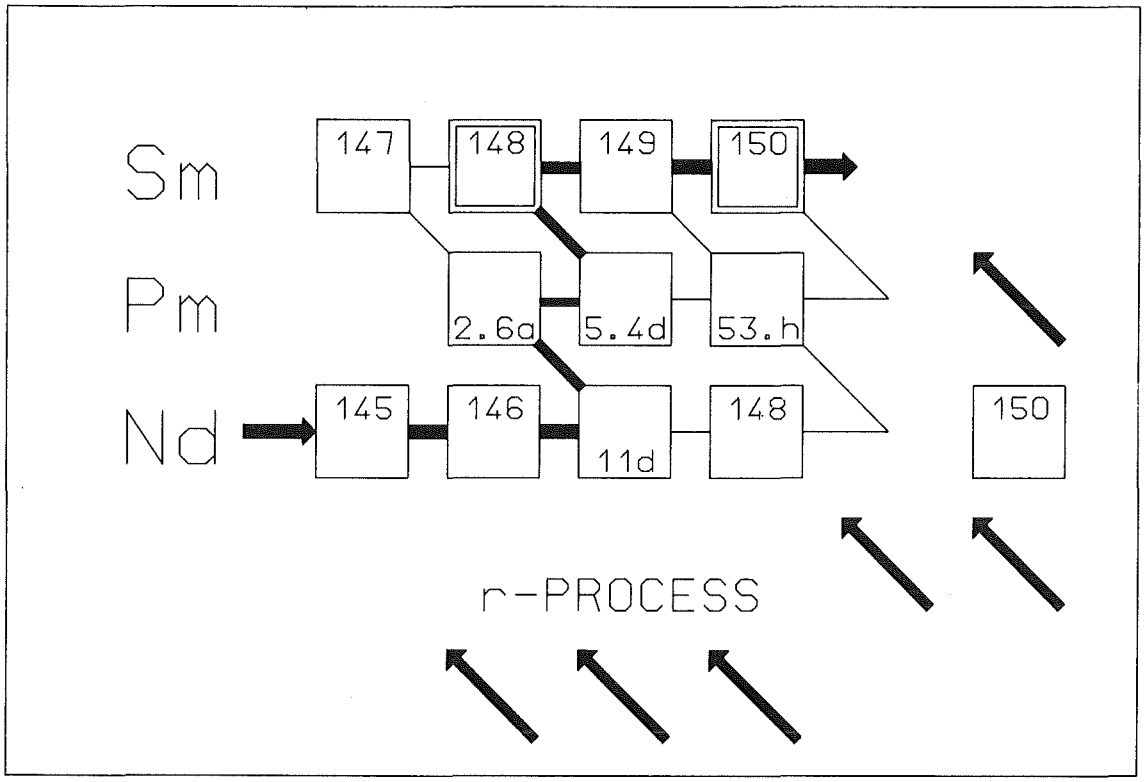


Fig. 1 The s-process path in the region of the samarium isotopes. The s-only isotopes $^{148,150}$Sm are shielded from the r-process by the stable isobars $^{148}$Nd and $^{150}$Nd. The unstable nuclei $^{147}$Nd and $^{147,148,149}$Pm are possible branching points.

this ratio with an uncertainty of ~1 %, and thus to derive a more stringent limit of the neutron density.

In addition, the absolute samarium cross sections are of general interest. Recently, it became obvious [10] that neutron capture cross section measurements in the rare earth region were severely affected by the absorption of water in the oxide samples used in most experiments. This leads to a systematic overestimation of the cross section, and could explain that previous results are varying up to factors of two [11]. This finding calls for new measurements with very well characterized samples.

The aim of the present investigations was to derive improved neutron capture cross sections of the s-only samarium isotopes $^{148}$Sm and $^{150}$Sm. These data, together with the respective results on tellurium and barium isotopes that are already available [6] or presently under evaluation, will allow to define the $\langle\sigma\rangle N_s$-curve in the region of the magic neutron shell, N=82. Secondly, the accurate determination of the cross section ratio will allow to reanalyse the branchings at A=147-149 in the framework of the classical s-process approach and

with a stellar model to derive new constraints for the s-process neutron density.

In the following we describe the experiment, the sample preparation and data evaluation in Sections II and III. The differential cross sections are presented in Sec. IV, while the uncertainties are discussed in Sec. V. Section VI is devoted to the determination of stellar cross sections, and the implications for the classical s-process approach are given in Sec. VII. A detailed discussion of the consequences for current stellar models will be the topic of a forthcoming publication.

## II. EXPERIMENT

### A. EXPERIMENTAL METHOD

The neutron capture cross sections of the samarium isotopes 147 to 150 and 152 were measured in the energy range from 3 to 225 keV using gold as a standard. The experimental method has been published in detail in Refs. [1] and [2]. Here, only the most essential features are repeated and changes or improvements that were introduced since our measurement on the tellurium isotopes [6] are described. Neutrons were produced via the $^{7}Li(p,n)^{7}Be$ reaction by bombarding metallic Li targets with the pulsed proton beam of the Karlsruhe 3.75 MV Van de Graaff accelerator. The neutron energy is determined by time of flight (TOF), the samples being located at a flight path of 78 cm. The important parameters of the accelerator are: pulse width ~1 ns, repetition rate 250 kHz, and average beam current 1.5 - 2 μA. In different runs, the energy of the proton beam was adjusted 30 and 100 keV above the reaction threshold of the $^{7}Li(p,n)^{7}Be$ reaction at 1.881 MeV. This yields continuous neutron spectra in the energy range of interest for s-process studies, i.e. 3 - 100 keV, and 3 - 200 keV, respectively. The use of different spectra allowed to optimize the signal to background ratio in different neutron energy regions (see Sec. III).

The Karlsruhe 4π Barium Fluoride Detector was used for the registration of capture gamma-ray cascades. This detector (a comprehensive description is given in Ref. [1]) consists of 42 hexagonal and pentagonal crystals forming a spherical shell of $BaF_2$ with 10 cm inner radius and 15 cm thickness. It is characterized by a resolution in gamma-ray energy of 7 % at 2.5 MeV, a time resolution of 500 ps, and a peak efficiency of 90 % at 1 MeV. Capture events are registered with ~95 % probability.

In one run of the present experiment, a newly implemented ADC system was used for data acquisition [12,13]. This system is based on CAMAC modules of type FERA (Le Croy). It allows to store the gamma-ray energy and TOF information of the individual detector modules that have fired in a particular event. A special preprocessing procedure rejects events in selectable sum energy and TOF regions; this decision is made within 4μs. The hardware trigger is made by a combination of ALU- (arithmetic logic unit) and MLU- (multiplicity logic unit) modules. Accepted events are transmitted from a data stack to a set of two memorys that are mutually used for input and output. The ADC-system in conjunction with the preprocessing is able to accept count rates up to 60 kHz. The recorded events are transmitted from the experiment computer (Data General MV 4000) to a workstation (Silicon Graphics IRIS) via ethernet file transfer. There, the events are stored either on optical disc or on DAT tape for further evaluation.

The purpose of the ADC system is fourfold. (i) It allows to measure capture cascades and capture gamma-ray spectra directly. This information is necessary to determine the detector efficiency for capture events and had to be taken from theoretical calculations before [2]. (ii) It allows for a deeper understanding of the capture process, e.g. by determining angular or multiplicity distributions of capture gamma-rays. (iii) It reduces significantly the recorded event rate by rejecting events in sum energy and TOF regions that are not needed for the evaluation of the cross section (see Sec. III). (iv) It allows to improve the resolution in gamma-ray sum energy by off-line corrections of the nonlinearity of individual detector modules.

The main advantages of using a $4\pi$ $BaF_2$ detector in combination with a Van de Graaff accelerator are the following: The entire capture cascade is detected with good energy resolution. Thus, ambiguities in the detection efficiency due to different cascade multiplicities are avoided, and neutron capture events can be separated from gamma-ray background and background due to capture of sample scattered neutrons by selecting events with appropriate sum energy. The high granularity of the detector allows for a further separation of capture events and background by means of the recorded event multiplicity . The short primary flight path and the inner radius of the detector guarantee that part of the TOF spectra is completely undisturbed by background from sample- scattered neutrons (see Sec. III). This range with optimum signal to background ratio can be used to normalize the cross section. The high detection efficiency allows the use of small samples avoiding large multiple scattering corrections. Finally, the $^7Li(p,n)$-reaction yields neutrons exactly and exclusively in the range of interest for s-process studies.

## B. SAMPLES

Isotopically enriched samples have been prepared from $Sm_2O_3$ powder. The relevant parameters of the eight samples are compiled in Table I . In addition to the five samarium samples a gold sample, a graphite sample, and an empty position in the sample changer frame was used in all runs. In one run, the small gold sample (Au I) and in the two others the larger sample (Au II) was used. The respective sample masses were selected according to the expected cross sections in order to obtain similar capture yields in all cases. The sample masses could be reduced by factors of 3 to 4 compared to those used by Winters et al. [9]. Hence, sample-related uncertainties, i.e. for multiple scattering and self-shielding corrections, are significantly smaller. The isotopes $^{147}Sm$, $^{149}Sm$, and $^{152}Sm$ were included in the measurement to correct the data for the s-only isotopes $^{148}Sm$ and $^{150}Sm$ for isotopic impurities.

**TABLE I.** Compilation of relevant sample data.

| Sample[a] | Thickness [mm] | Thickness[b] [$10^{-3}$ A/barn] | Weight [g] | Water[c] content [%][f] | Canning[d] [mg ] | Impurity[e] [%][f] | Neutron binding energy [MeV] |
|---|---|---|---|---|---|---|---|
| Au I | 0.26 | 1.5067 | 0.8708 | | 5.4 | | 6.513 |
| Au II | 0.4 | 2.2474 | 1.2989 | | 7.2 | | |
| Graphite | 4.0 | 34.320 | 1.2096 | | | | |
| $^{147}Sm$ | 0.6 | 0.9255 | 0.3993 | 0.23 | 7.2 | <0.2 | 8.141 |
| $^{148}Sm$ | 2.6 | 4.5331 | 1.9694 | 0.17 | 8.9 | <0.2 | 5.872 |
| $^{149}Sm$ | 1.0 | 1.7294 | 0.7563 | 0.14 | 7.3 | <0.2 | 7.986 |
| $^{150}Sm$ | 2.2 | 3.0603 | 1.3474 | 0.22 | 8.1 | <0.2 | 5.597 |
| $^{152}Sm$ | 1.9 | 3.2253 | 1.4387 | 0.14 | 8.0 | <0.2 | 5.867 |

[a] samples of 15 mm diameter

[b] for samarium samples: sum of all Sm isotopes ( oxygen not included ), chemical composition $Sm_2O_3$.

[c] as determined from the increase in weight of the samples

[d] polyethylene foil ($CH_2$)

[e] Impurity of other elements except oxygen

[f] % of weight

The exact characterization of the sample is a severe problem for accurate cross section measurements [14]. This was particularly difficult in the present case since samarium oxide is hygroscopic. The absorption of water in the samples can severely deteriorate capture cross section measurements [10]. Therefore, the pellets pressed from oxide powder were heated to 1000 deg under a steady flow of dry air, and their weight determined immediately afterwards. Then, the pellets were kept in a dry atmosphere until they were welded into thin polyethylene foils to avoid further absorption of water. During the heating, there was a significant loss in weight. After a slight increase during the first days, the samples were very stable over the measuring period of ~6 month. The changes in weight during the individual steps are compiled in Table II with the weight immediately after the heating procedure taken for normalization. The observed increase in weight was assumed to be due to absorption of water at the surface of the samples. The respective contamination is given in the fifth column of Table I.

After the experiment, the material was carefully analysed to confirm the low contamination with water and to look for possible deviations from the assumed stoichiometry. In a first analysis part of the sample material was dissolved in diluted nitric acid to a concentration of about 30 mg/ml. The exact samarium concentration was determined by means of the method of K-edge densitometry [15,16]. A well collimated beam of X-rays with a continuous energy distribution passes the liquid sample filled in a well defined geometry. The X-ray spectrum (see Fig. 2) is observed with a HP-Ge detector and the concentration is determined from the step at the K-edge. For calibration two types of standard solutions have been prepared covering the concentration range of the actual solutions. One set was prepared from natural $Sm_2O_3$ by producing pellets in exactly the same way as for the enriched samples. The other set was prepared from samarium metal that was handled in a clove box filled with argon. The result is shown in Fig. 3, where the ratio of measured and calculated concentration is plotted versus concentration. The concentration was calculated under the assumption that the dissolved material is pure $Sm_2O_3$ or Sm, respectively. For calibration, the average of the eight standard solutions prepared from natural samarium was set to unity. The uncertainties of the individual measurements are 0.4 %, mainly determined by filling the volumetric flasks of 10 ml used for preparation of the solutions. From the results of Fig. 3 the following conclusions can be drawn: The average of the four measurements with standard sources prepared from samarium metal (open triangles in Fig. 3) or samarium oxide (open squares in Fig. 3) agree within 0.17 %. This is strong evidence that the oxide samples contain no water or other impurities at the time immediately after heating, when the weight was determined; the same holds for the enriched samples, as well. The results

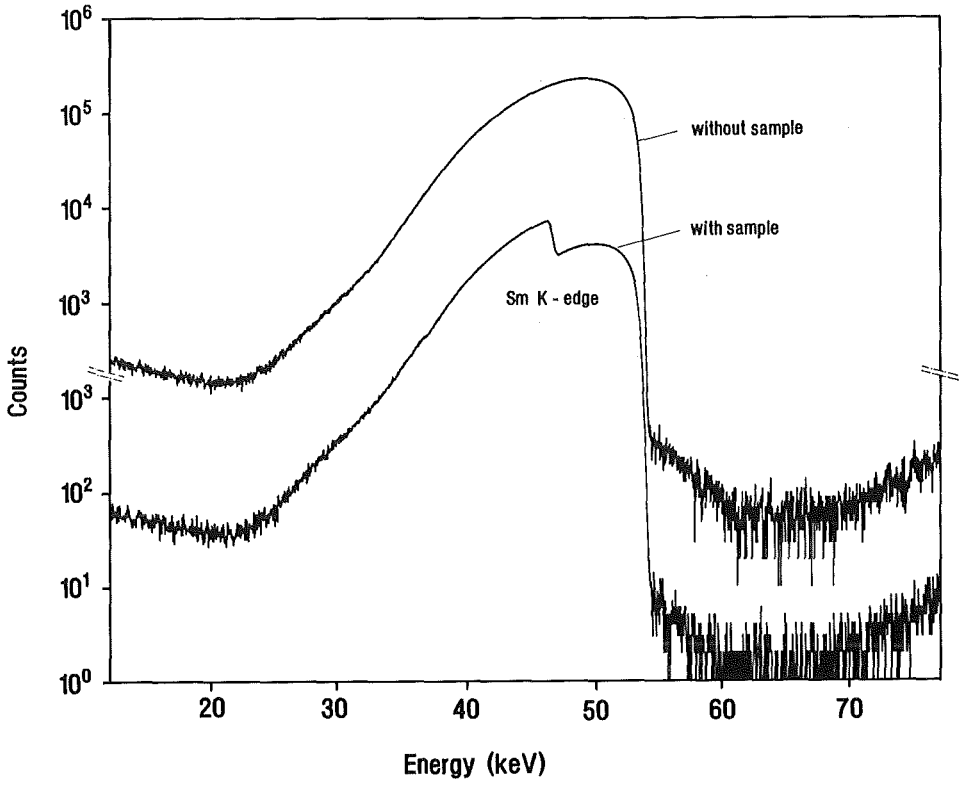


Fig. 2 X-ray spectra measured with and without sample. The samarium concentration is determined from the jump in intensity at the K-edge

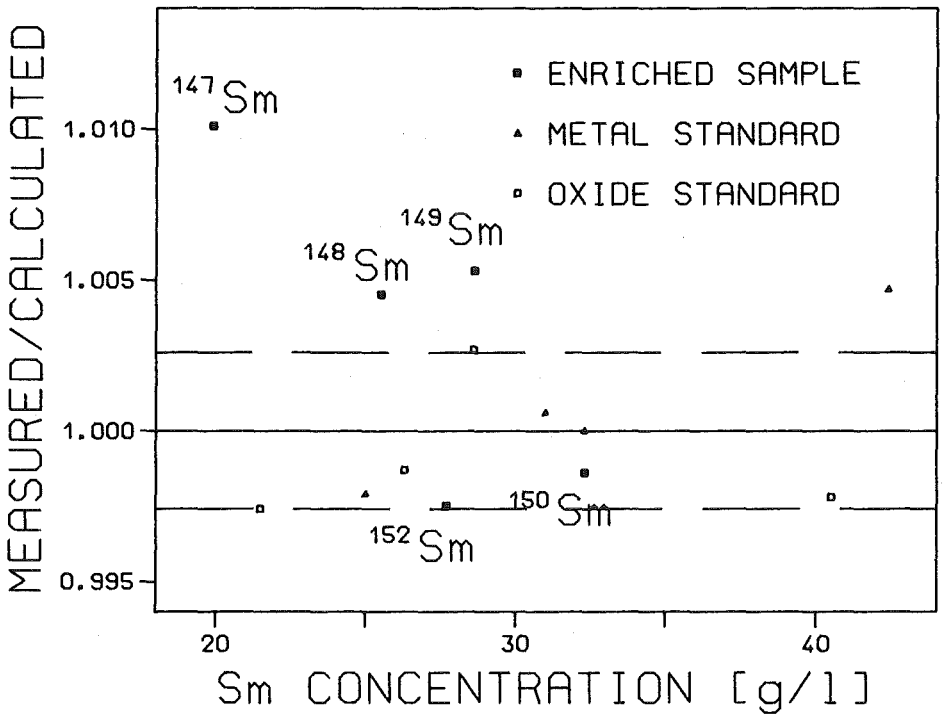


Fig. 3 Ratio of measured and calculated samarium concentration. The average of the eight standard solutions was set to unity.

**TABLE II.** Weight of the samarium samples versus time (normalized to the weight determined immediately after heating the pellets to 1000 deg.).

| | | Pellet before heating | Pellet after heating | Pellet bevor canning | Pellet after experiment |
|---|---|---|---|---|---|
| Sample | $^{147}$Sm | 1.137 | 1 | 1.0016 | 1.0029 |
| | $^{148}$Sm | 1.015 | 1 | 1.0013 | 1.0020 |
| | $^{149}$Sm | 1.072 | 1 | 1.0011 | 1.0016 |
| | $^{150}$Sm | 1.036 | 1 | 1.0019 | 1.0026 |
| | $^{152}$Sm | 1.047 | 1 | 1.0011 | 1.0016 |
| Time | | -1 d | 0 | 60 d | 210 d |

for the enriched samples are compatible with unity within their uncertainty of 0.4 %. The only exception is the result for $^{147}$Sm where the measured concentration is too high by about 1 %. This could be explained only if the specified stoichiometry of the material was incorrect, e.g. by a samarium excess in the sample.

A second batch of the sample material was analysed in the analytic laboratory of the material research department at KfK for its water content. According to the coulometric method of Fischer, the water was extracted from the samples at 900 deg in a stream of nitrogen gas and collected in a coulometric measuring cell. The amount of water was then determined by titration. The samarium content was determined for a second time by X-ray fluorescence analysis using the method of borax discs. The respective results are completely independent from the X-ray absorption experiment and slightly more accurate. The measurement was calibrated by preparing standard disks from high purity natural samarium in exactly the same way as for the enriched isotopes. The results of these analyses are compiled in Table III. With the quoted uncertainties the results of the water and samarium determination add up to 100 %. The amount of water found in the samples is well in agreement with the increase in sample weight given in Table II. A deviation in stoichiometry of the $^{147}$Sm sample was not observed in this analysis.

**TABLE III.** Chemical analyses of the samples performed after the experiment.

| | | Water content [%][a] | Samarium content [%][a] | $Sm_2O_3$ content [%][a] | Sum [%][a] |
|---|---|---|---|---|---|
| Sample | $^{147}Sm$ | 0.38 ± 0.08 | 85.82 ± 0.11 | 99.83 ± 0.15 | 100.21 |
| | $^{148}Sm$ | 0.14 ± 0.01 | 85.97 ± 0.23 | 99.91 ± 0.27 | 100.05 |
| | $^{149}Sm$ | 0.13 ± 0.01 | 86.04 ± 0.17 | 99.89 ± 0.20 | 100.02 |
| | $^{150}Sm$ | 0.17 ± 0.01 | 85.73 ± 0.26 | 99.44 ± 0.30 | 99.61 |
| | $^{152}Sm$ | 0.17 ± 0.01 | 86.26 ± 0.32 | 99.88 ± 0.37 | 100.05 |

[a] percent of the weight

There is still one drawback that has to be discussed in more detail. Canning of the samples in thin polyethylene foils, helped to prevent further absorption of water during the experiment, but is certainly not ideal as it adds hydrogen to the samples, as well. The polyethylene weights are given in Table I , and seem to be significant compared to the total sample masses. However, one has to keep in mind that neutron scattering in hydrogen goes mainly in forward direction with a maximum scattering angle of 45 deg. Thus, only neutrons scattered in the front part of the canning will hit the sample. The weight of this part is 1.8 mg corresponding to 2.3 mg water. This is about 0.2 % of the sample mass and thus of the same size as the water content of the samples given in Table I. The contribution of these cannings to the uncertainty of the measured data will be discussed in Section V.

As a third step in characterizing the samples, the isotopic composition was redetermined at KfK. The results are compiled in Table IV together with the data provided by the suppliers. Very good agreement is found between the various data sets.

The diameter of the samples was 15 mm. As can be seen from Table I, the thickness of some samples is comparatively large, and the transmission decreases down to 0.90 (see Table V). Since accurate data for the total cross section of the samarium isotopes were not available from literature, the spectra measured with the neutron monitor at 260 cm flight path did not allow to check the normalization of the neutron flux as in our first measurement (Ref. [2]). However, since the scintillator of this neutron monitor is completely shaded by the sample, the measured TOF spectra can in turn be used for a rough determina-

**TABLE IV.** Isotopic enrichment of the samarium samples [%].

| Sample | Isotope 144 | 147 | 148 | 149 | 150 | 152 | 154 | |
|---|---|---|---|---|---|---|---|---|
| $^{147}$Sm | 0.05 | 98.29 | 0.85 | 0.36 | 0.11 | 0.21 | 0.13 | ORNL |
| | 0.05 | 98.27 | 0.85 | 0.36 | 0.11 | 0.22 | 0.14 | KfK |
| $^{148}$Sm | 0.10 | 1.00 | 95.40 | 2.60 | 0.30 | 0.40 | 0.20 | USSR |
| | 0.08 | 1.00 | 95.31 | 2.61 | 0.37 | 0.42 | 0.21 | KfK |
| $^{149}$Sm | 0.10 | 0.20 | 0.80 | 96.90 | 1.40 | 0.40 | 0.20 | USSR |
| | 0.05 | 0.22 | 0.82 | 96.70 | 1.51 | 0.48 | 0.22 | KfK |
| $^{150}$Sm | --- | 0.40 | 0.50 | 1.10 | 95.00 | 2.30 | 0.70 | USSR |
| | 0.06 | 0.41 | 0.46 | 1.14 | 94.87 | 2.38 | 0.68 | KfK |
| $^{152}$Sm | --- | 0.10 | 0.15 | 0.12 | 0.14 | 99.00 | 0.50 | USSR |
| | 0.02 | 0.10 | 0.15 | 0.12 | 0.15 | 98.88 | 0.58 | KfK |

**TABLE V.** Transmission of the samples [a].

| Sample | Neutron energy [keV] | | | | |
|---|---|---|---|---|---|
| | 10 | 20 | 40 | 100 | 200 |
| Au I | 0.976 | 0.979 | 0.982 | 0.985 | 0.988 |
| Au II | 0.964 | 0.969 | 0.973 | 0.978 | 0.982 |
| $^{147}$Sm | 0.960 | 0.969 | 0.976 | 0.983 | 0.988 |
| $^{148}$Sm | 0.894 | 0.905 | 0.916 | 0.928 | 0.937 |
| $^{149}$Sm | 0.945 | 0.956 | 0.964 | 0.972 | 0.978 |
| $^{150}$Sm | 0.915 | 0.927 | 0.939 | 0.952 | 0.960 |
| $^{152}$Sm | 0.932 | 0.939 | 0.945 | 0.952 | 0.957 |

[a] Monte Carlo calculation with SESH code

tion of the total cross section. Though the accuracy of this method is inferior to that obtained in a dedicated experiment, the data are sufficient for the reliable calculation of the multiple scattering corrections (see Sec. III).

## C. MEASUREMENTS

The samples were moved cyclically into the measuring position by a computer controlled sample changer. The data acquisition time per sample was about 10 min, a complete cycle lasting about 1.5 h. From each event, a 64 bit word was recorded on magnetic tape containing the sum energy and TOF information together with 42 bits indicating those detector modules that have contributed. As mentioned above, two runs have been performed using neutron spectra with different maximum energy. The essential parameters are compiled in Table VI. For the first time, the data in run III were recorded with an ADC system. In this case gamma-ray energy and TOF were stored for all detector modules. An automatic offset suppression guarantees, that only those modules which contributed significantly to an event were read out. The maximum neutron energy was chosen at 200 keV as in run II. In this way, both methods could be checked against each other under identical experimental conditions. In runs I and II , 120 high density tapes of data containing roughly 20 Gbyte of information were recorded, in run III, where the information to be stored per event is much larger, the total amount of data was 8 Gbyte. The increased amount of information stored per event is compensated by the preprocessing that rejects about 50 % of the events. The spectra of the two neutron monitor detectors were stored on magnetic disk.

**TABLE VI.** Parameters of the individual measurements.

| Run | Flight path [mm] | Time calibration [ns/channel] | Number of cycles | Maximum neutron energy [keV] | Measuring time [h] | Average beam current [μA] | Sum energy threshold [MeV] |
|---|---|---|---|---|---|---|---|
| I | 785.8 | 0.7353 | 210 | 100 | 345 | 1.5 | 2.4 |
| II | 785.8 | 0.7353 | 258 | 200 | 351 | 2.0 | 2.5 |
| III | 785.5 | 0.7150 | 192 | 200 | 440 | 1.7 | 2.4 |

## III. DATA EVALUATION

### A. TOTAL CROSS SECTIONS

The total cross sections of the samarium isotopes were determined in the neutron energy range from 10 to 200 keV from the TOF spectra measured with the lithium glass neutron monitor at a flight path of 260 cm. As shown in Fig. 4, the difference of the count rates recorded with and without sample are small, but statistics are excellent due to the large acquisition time of the capture measurement. The countrate in each TOF channel t is composed of three parts ${}^{x}C(t) = {}^{x}C1(t) + {}^{x}C2(t) + {}^{x}C3$, where index x counts the samples, x=0 being the empty position. C1 is the measured effect due to primary neutrons reacting in the lithium glas, while C2 is a time-dependent background caused by neutrons scattered from the detector material into the scintillator. C3 is a time-independent background due to moderated neutrons. The transmission T and the total cross section $\sigma$ of sample x with thickness n is simply given by the relation :

$$ {}^{x}T = e^{-n(x)\sigma(x)} = {}^{x}C1/{}^{o}C1 $$

While the time-independent background can easily be determined from the countrate at very large TOF right of the prompt gamma-ray peak (see Fig. 4), certain assumptions had to be made for the time-dependent background C2. We assumed that C2 at energy E is proportional to the integral number of neutrons hitting the sample in the energy interval from E to $E_{max}$, and that this flux is proportional to the average transmission $\langle T(E-E_{max})\rangle$ in this energy interval. If, as for the present samples, the transmission is very high, it is to first approximation energy-independent (see Table V). Thus the background C2 is proportional to T(E) like the countrate C1, and can, therefore, be neglected. In other words, with the assumptins made above, the transmission is independent of C2.

$$ \frac{{}^{x}C1(E)+{}^{x}C2(E)}{{}^{o}C1(E)+{}^{o}C2(E)} = \frac{{}^{x}C1(E)+\langle {}^{x}T(E-E_{max})\rangle * \alpha}{{}^{o}C1(E)+ \quad 1 \quad * \alpha} = \frac{{}^{x}C1(E) + {}^{x}T(E)*\alpha}{{}^{o}C1(E) + \quad \alpha} = \frac{{}^{x}C1(E) + {}^{x}C1(E)/{}^{o}C1(E)*\alpha}{{}^{o}C1(E) + \quad \alpha} = \frac{{}^{x}C1(E)}{{}^{o}C1(E)} $$

The simplification $\langle {}^{x}T(E-E_{max})\rangle = {}^{x}T(E)$ used above is justified since the background is much smaller than the measured effect (C1>>C2).

The resulting total cross sections of all samples are given in Table VII. They were calculated using the total cross section for oxygen from the JEF- (Joint Evaluated File) evaluation [17]. The results for the carbon sample are systematically lower by three percent compared to the data from JEF. This deviation was adopted as a reasonable systematic uncertainty of the present experiment for a sample with 86 % transmission. In all other samples the

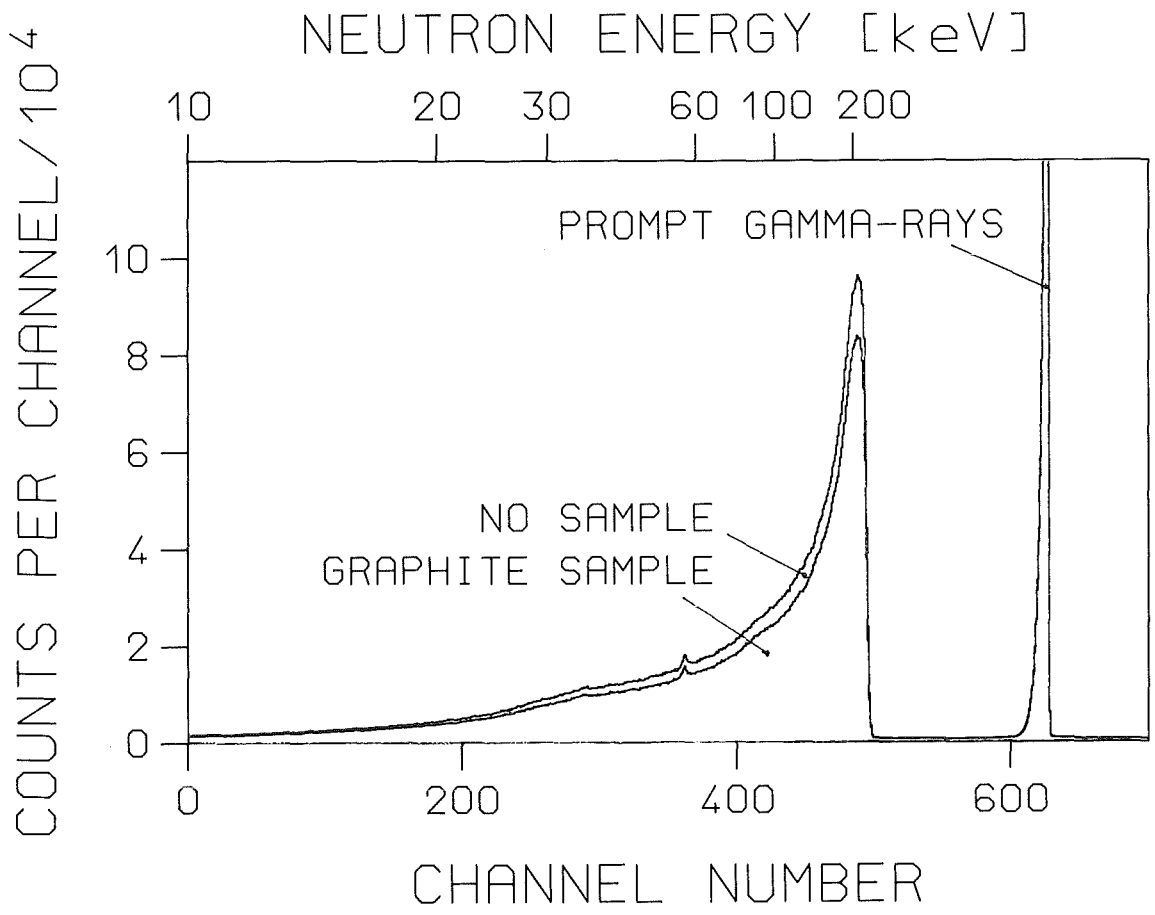


Fig. 4 Spectra of the neutron monitor measured with and without sample used for the determination of the total cross section

absorption A = 1-T is much smaller, and consequently higher systematic uncertainties are quoted in Table VII assuming a 1/A dependence. Compared to that effect, statistical uncertainties can be neglected. The total cross section of elemental samarium calculated from our isotopic cross sections is found in reasonable agreement with the data of Ref. [18]. The gold cross section is systematically larger as given in Ref. [18], but in the energy range from 10 to 100 keV the available data were from an experiment made in 1965 [19]. The total cross sections are important for the proper correction of neutron multiple scattering effects in the capture experiment (see below).

### B. EVALUATION OF THE CAPTURE CROSS SECTIONS

The data evaluation has been described in detail in Ref. [2]. All events stored on magnetic tape were sorted into two-dimensional sum energy versus TOF spectra according to event multiplicities (evaluation 1). In evaluation 2, this procedure was repeated by rejecting those events, where only neighboring detector modules contributed to the sum energy signal, in

**TABLE VII.** The total cross sections determined from the countrate of the $^{6}Li$ glass neutron monitor at 260 cm flight path. .

| Neutron Energy [keV] | Total Cross Section [b] | | | | | | |
|---|---|---|---|---|---|---|---|
| | $^{147}Sm$ | $^{148}Sm$ | $^{149}Sm$ | $^{150}Sm$ | $^{152}Sm$ | C | $^{197}Au$ |
| 10 - 15 | 36.0 | 19.4 | 25.5 | 24.8 | 15.2 | 4.39 | 18.9 |
| 15 - 20 | 25.9 | 17.6 | 22.1 | 21.7 | 12.8 | 4.40 | 16.6 |
| 20 - 30 | 25.4 | 16.6 | 19.9 | 18.0 | 14.9 | 4.51 | 17.1 |
| 30 - 40 | 23.6 | 15.5 | 17.9 | 16.1 | 11.7 | 4.36 | 14.9 |
| 40 - 60 | 20.4 | 12.9 | 16.1 | 15.5 | 11.8 | 4.48 | 14.7 |
| 60 - 80 | 17.0 | 12.8 | 13.3 | 13.9 | 10.5 | 4.35 | 13.1 |
| 80 - 100 | 14.8 | 12.8 | 13.4 | 11.7 | 9.7 | 4.13 | 12.4 |
| 100 - 150 | 15.0 | 10.3 | 11.6 | 11.7 | 9.5 | 4.17 | 11.5 |
| 150 - 200 | 11.8 | 9.3 | 10.1 | 11.2 | 8.9 | 4.10 | 10.5 |
| uncertainty | 18 % | 5 % | 11 % | 6 % | 7 % | 3 % | 13 % |

**TABLE VIII.** Matrix for the isotopic correction [%][a].

| Corrected Spectrum | Measured Spectrum | | | | | Corrected Sample Thickness [$10^{-3}$ At/barn] |
|---|---|---|---|---|---|---|
| | $^{147}Sm$ | $^{148}Sm$ | $^{149}Sm$ | $^{150}Sm$ | $^{152}Sm$ | |
| $^{147}Sm$ | 100 | -0.2107 | -0.1832 | -0.0324 | -0.0586 | 0.9095 |
| $^{148}Sm$ | -4.9493 | 100 | -7.0138 | -0.4068 | -0.5407 | 4.3326 |
| $^{149}Sm$ | -0.3486 | -0.3977 | 100 | -0.8305 | -0.1959 | 1.6750 |
| $^{150}Sm$ | -1.2870 | -0.8746 | -1.9396 | 100 | -2.1944 | 2.9066 |
| $^{152}Sm$ | -0.3260 | -0.5180 | -0.1908 | -0.1512 | 100 | 3.1929 |

[a] using the approximation $\sigma(^{144}Sm)=0$ and $\sigma(^{154}Sm)=1.10\times\sigma(^{148}Sm)$

order to reduce background from the natural radioactivity of the $BaF_2$ crystals and from capture of scattered neutrons in the scintillator material. These spectra were normalized to equal neutron flux using the count rate from the lithium glass monitor, which was located close to the neutron target; these normalization factors are in general well below 1 %.

The calculation of the two-dimensional spectra from the data recorded with the ADC system is slightly more complicated. The energy and TOF scales of the 42 detector modules were calibrated before and after the experiment. In addition, we used sources of $^{228}$Th, Am+Be, and Pu+$^{13}$C to determine possible deviations of the energy calibration from linearity for each detector module. During the sorting procedure, events were accepted only, if energy and TOF information were recorded from the contributing detector modules. The gamma-ray energies of the individual modules were corrected for the respective nonlinearity. Then, the measured offset was subtracted and the gain was transformed to the average value of all modules. Finally, the sum energy of the event could be calculated by adding the individual gamma-ray energies of the cascade. The TOF information of all modules was similarly transformed to a mean time calibration and a common position of the prompt gamma-ray peak that indicates the zero point of the time measurement. The shortest TOF value of all contributing modules was taken as representative for the event . Thus gamma-rays scattered from one detector module into another do not deteriorate the time resolution.

In the next step, the spectra measured without sample were subtracted to remove the sample-independent background. The remaining time-independent background was determined at very long flight times (~3.9 µs), where no time-correlated events are expected. Two-dimensional spectra of runs I and III containing all events with multiplicity >2 are shown in Fig. 5. Note, that in the spectra of run III the events at low sum energy and large TOF are suppressed by the hardware trigger of the ADC system.

At this point, the spectra contain only events that are correlated with the sample. The next correction to be made was for isotopic impurities. In contrast to neutron capture experiments without resolution in gamma-ray energy [9], the contribution to isotopic impurities has to be eliminated from the measured spectra before evaluating the correction for scattered neutrons or determining the capture yield. This is important, since the respective events are located predominantly at different sum energies. Therefore, the spectra of the impurity isotopes were subtracted after normalizing them to their respective abundance in the sample under investigation. These coefficients are compiled in Table VIII. The isotopes $^{144}$Sm and $^{154}$Sm were not included in the present experiment. The effect of $^{144}$Sm was neglected

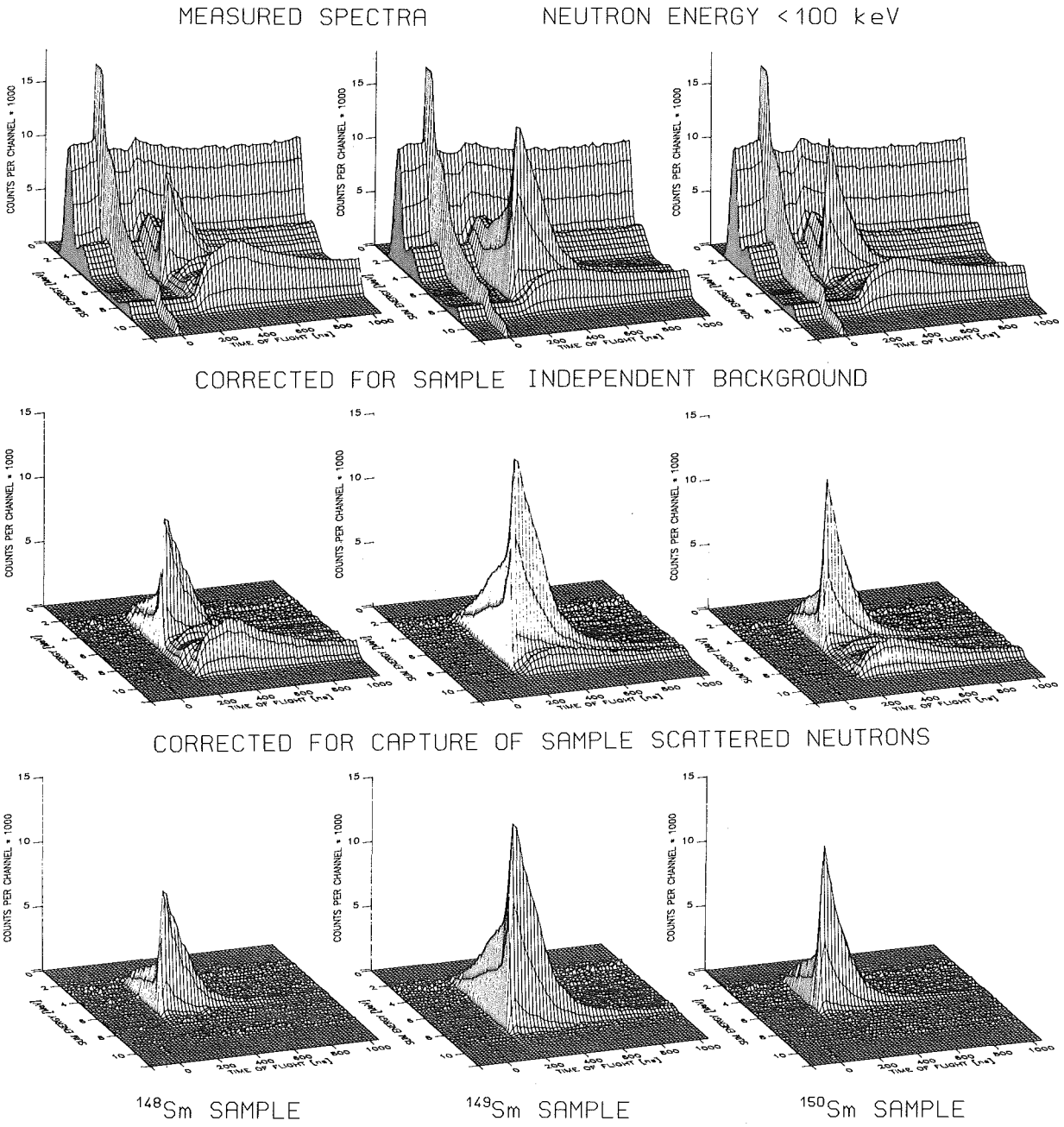


Fig. 5a The different steps of background subtraction in the two dimensional sum energy × TOF spectra. The data are shown for three samarium isotopes measured in run I with 100 keV maximum neutron energy. ( The original resolution of 128×2048 channels was compressed in the plots into 64×64 channels )

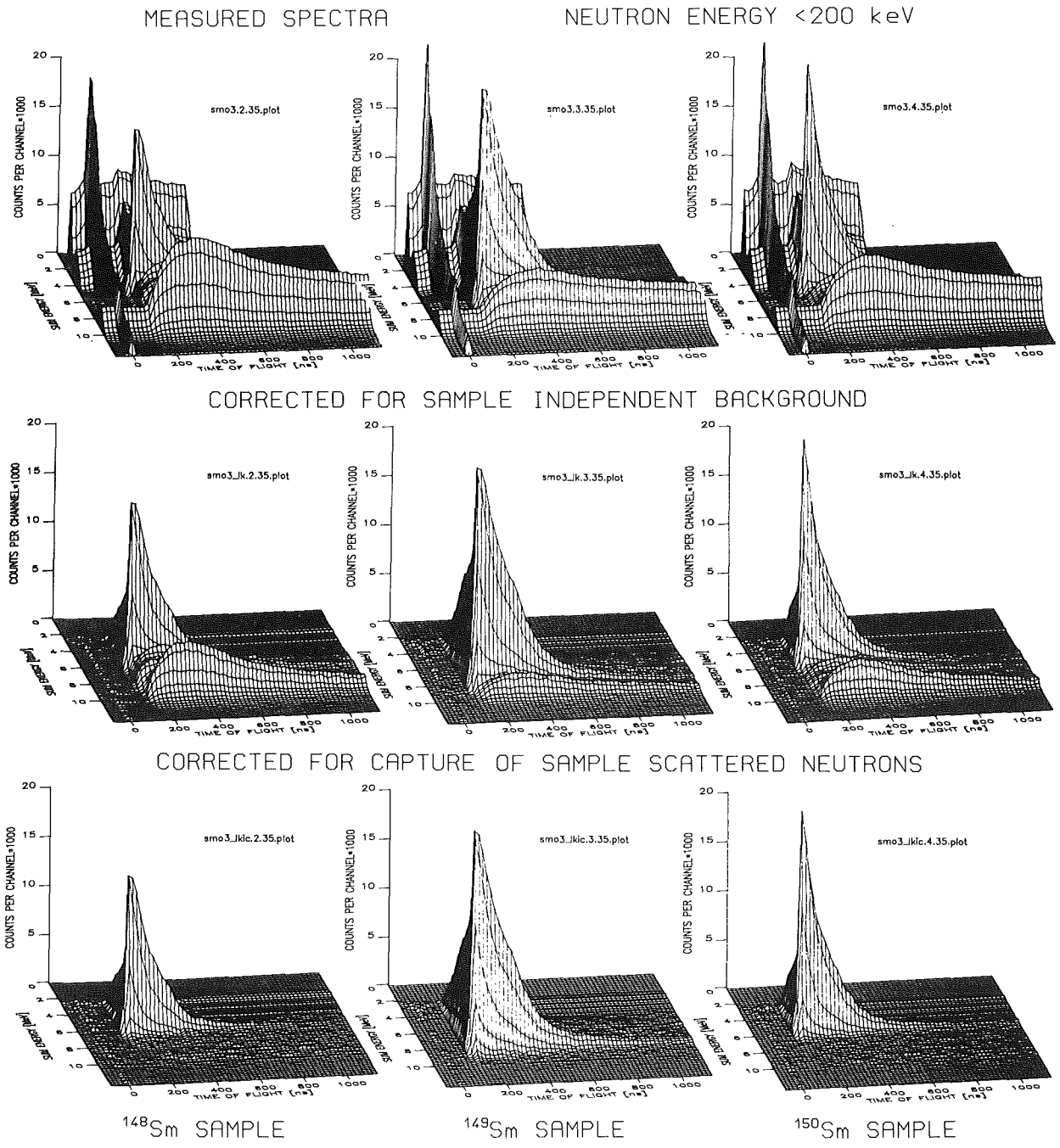


Fig. 5b The same as Fig. 2a but for run III with a maximum neutron energy of 200 keV. These data were recorded with the ADC system. Note that events with low sum energy and large TOF are suppressed by the preprocessing of the data.

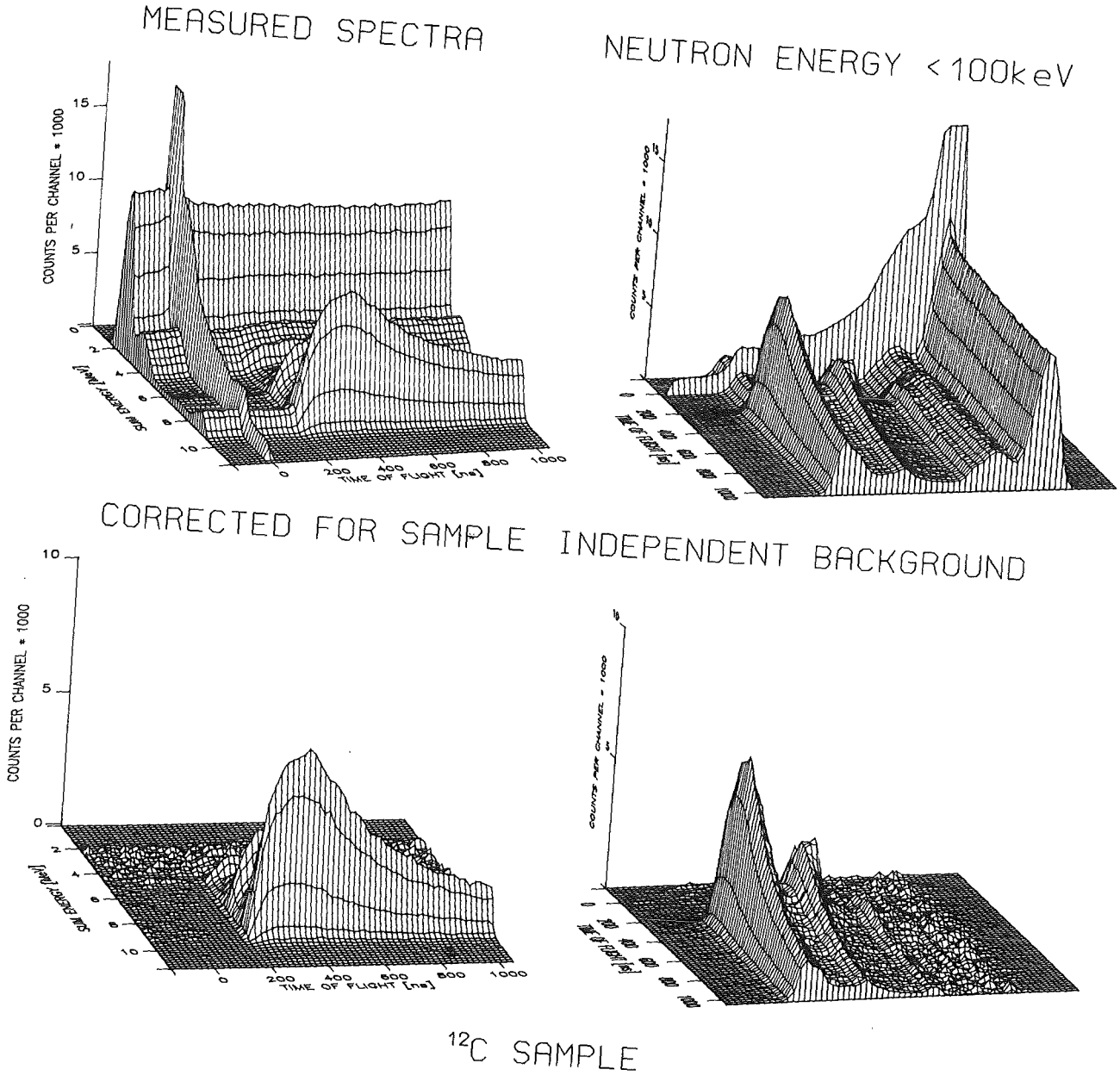


Fig. 5c The respective spectra measured with the carbon sample in run I to simulate the background due to capture of sample scattered neutrons in the $BaF_2$ scintillator. The sum energy × TOF plane is shown from two different viewpoints.

in the analysis since the respective impurities are less or equal to 0.1 % in all samples (see Table IV), and since the cross section is at least a factor of 3 smaller than for all other isotopes [11]. The correction for $^{154}$Sm was treated as for $^{148}$Sm, since this isotope has about the same binding energy, but the abundance was scaled by a factor 1.1 to account for the slightly larger cross section. The impurity of this isotope is always smaller than one percent; therefore, this assumption does not affect the results. The coefficients in the correction matrix are in general of the order of 1 % or less. The worst case is $^{148}$Sm, where - according to Table VIII - the corrected spectrum is calculated by:

$$^{148}Sm_{corr.} = {}^{148}Sm_{meas.} - 0.049 \times {}^{147}Sm_{meas.} - 0.070 \times {}^{149}Sm_{meas.} - 0.004 \times {}^{150}Sm_{meas.} - 0.005 \times {}^{152}Sm_{meas.}$$

The capture yields of the samples are about equal except for the $^{149}$Sm sample where it is a factor of two larger. At first glance, the above equation seems to imply that the $^{148}$Sm yield is reduced by ~ 20 %. Actually, the reduction is < 8 % as most of the countrate in the $^{149}$Sm and $^{147}$Sm spectra is located near the binding energy of 8 MeV, a region that is not used for the evaluation of the $^{148}$Sm cross section at all (binding energy 5.8 MeV). It has to be mentioned that in an experiment using the pulse height weighting technique, where no energy information is available [9], and where the efficiency is proportional to the binding energy, the corresponding correction would be about 30% of the observed effect, a factor of 4 larger than in the present case. The isotopic corrections are indicated for three samples in Fig.6, showing the TOF spectra used for the determination of the cross section shape (see below) together with the countrate that is removed by the isotopic correction.

In the corrected spectrum, e.g. of $^{148}$Sm, that was calculated using the matrix elements in Table VIII, not only the isotopic impurities are eliminated, but also the effect of the main isotope is reduced. This is because the spectra measured with the other samples contain $^{148}$Sm as an impurity. In the final analysis, this was considered by a corrected sample thickness, that is given in the last column of Table VIII.

After the correction for isotopic impurities, the background due to capture of sample scattered neutrons was removed from the spectra by means of the data measured with the carbon sample. The scattered neutrons are captured mainly in the barium isotopes of the scintillator. This is shown in Fig. 7, where the sum energy of the events recorded with the graphite sample is plotted. The figure clearly demonstrates the very small capture cross section of $^{138}$Ba, since capture in this isotope is barely visible despite its large abundance of 72 % . The binding energy of the even samarium isotopes being below 5.9 MeV, results in an efficient background reduction because capture in the other barium isotopes are well separated by their sum energy from the true capture events in the

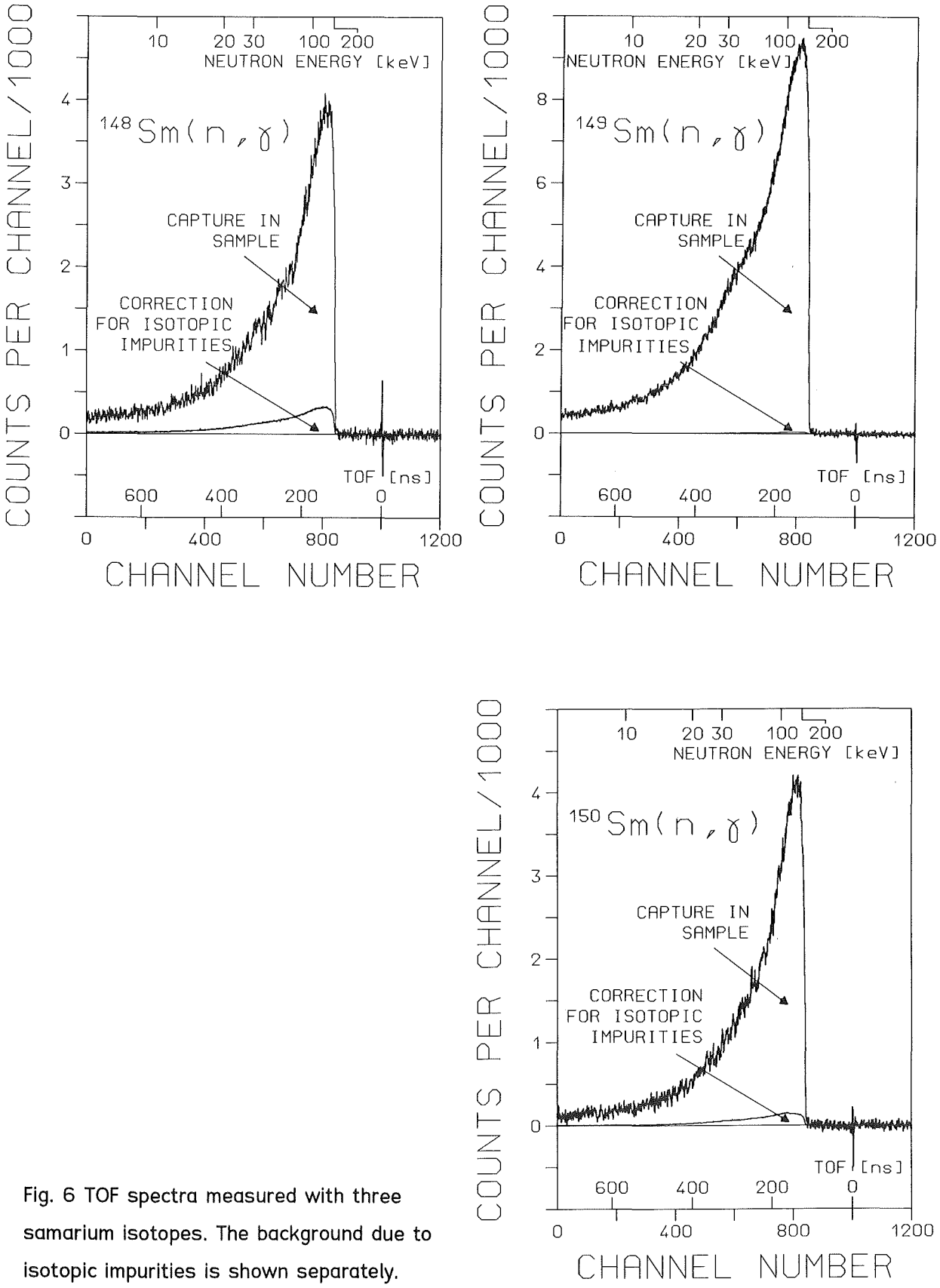


Fig. 6 TOF spectra measured with three samarium isotopes. The background due to isotopic impurities is shown separately.

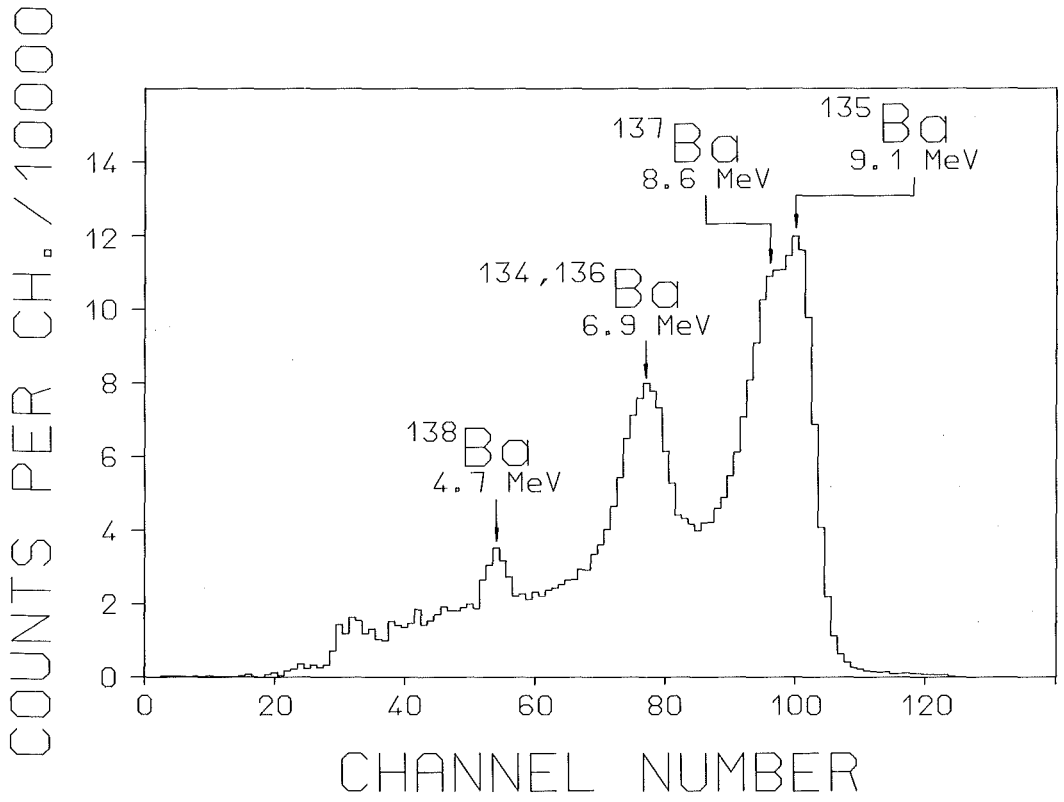


Fig. 7 Sum energy spectrum measured with the graphite sample, showing capture events in the different barium isotopes of the scintillator.

sample (see Fig. 5). Actually, the sum energy range from channels 76 to 106 could be used for normalizing the scattering correction. This normalization is calculated in dependence of the TOF, which is very important for the accuracy of the experimental method. After this correction, the spectra contain true capture events only ( lower part of Fig. 5 ), and can be used to determine the cross sections.

The binding energy of the odd samarium isotopes is 8.1 and 7.9 MeV, respectively, thus the lower end of the normalization interval had to be increased to channel numbers 98 or 100. This comparably small intervall was still sufficient for determination of reliable corrections.

The correction for sample scattered neutrons are illustrated in Fig. 8. The TOF spectra of the $^{148,149,150}$Sm samples are plotted after projection of the two-dimensional data in the sum energy range around the binding energy (see below ) together with the background due to capture of sample scattered neutrons. The data are given for runs I and II with 100 and 200 keV maximum neutron energy. The large cross sections of the samarium isotopes allowed to evaluate the cross section down to 3 keV.

**TABLE IX.** Signal to background ratio versus neutron energy for runs with different maximum neutron energy

| Sample | $\sigma_t/\sigma_\gamma$ at 30 keV | Maximum neutron energy [keV] | Signal to background ratio | | |
|---|---|---|---|---|---|
| | | | Neutron Energy [keV] | | |
| | | | 30 | 20 | 10 |
| $^{147}$Sm | 27 | 100 | 4.9 | 2.5 | 1.7 |
| $^{148}$Sm | 73 | | 4.5 | 2.2 | 1.4 |
| $^{149}$Sm | 11 | | 13.1 | 7.6 | 4.0 |
| $^{150}$Sm | 46 | | 7.8 | 4.0 | 2.2 |
| $^{152}$Sm | 29 | | 10.0 | 4.7 | 2.3 |
| Au | 24 | | 7.5 | 3.5 | 2.2 |
| $^{147}$Sm | | 200 | 4.6 | 2.8 | 1.9 |
| $^{148}$Sm | | | 3.6 | 2.2 | 1.4 |
| $^{149}$Sm | | | 9.0 | 5.1 | 3.5 |
| $^{150}$Sm | | | 5.8 | 3.5 | 1.8 |
| $^{152}$Sm | | | 6.9 | 3.7 | 2.1 |
| Au | | | 5.6 | 3.4 | 2.0 |

In Table IX, the signal to background ratio is compiled for the samarium isotopes as well as for the gold standard in more detail. In spite of the fact that the ratio of total and capture cross sections, $\sigma_t/\sigma_\gamma$, varies by a factor of seven for the individual samarium isotopes, the signal to background ratios differ by a factor 2.5 only. This can be understood, if the different binding energies are taken into account. The signal to background ratio is determined mainly by the interplay of capture cross section and the overlap between capture in the sample and capture in barium. Both quantities are large for the odd but small for the even isotopes. Thus, the signal to background ratio is about equal in both cases.

After subtraction of the background, the TOF spectra shown in Fig. 8 were used to determine the shape of the cross section. For normalization, the two-dimensional spectra were

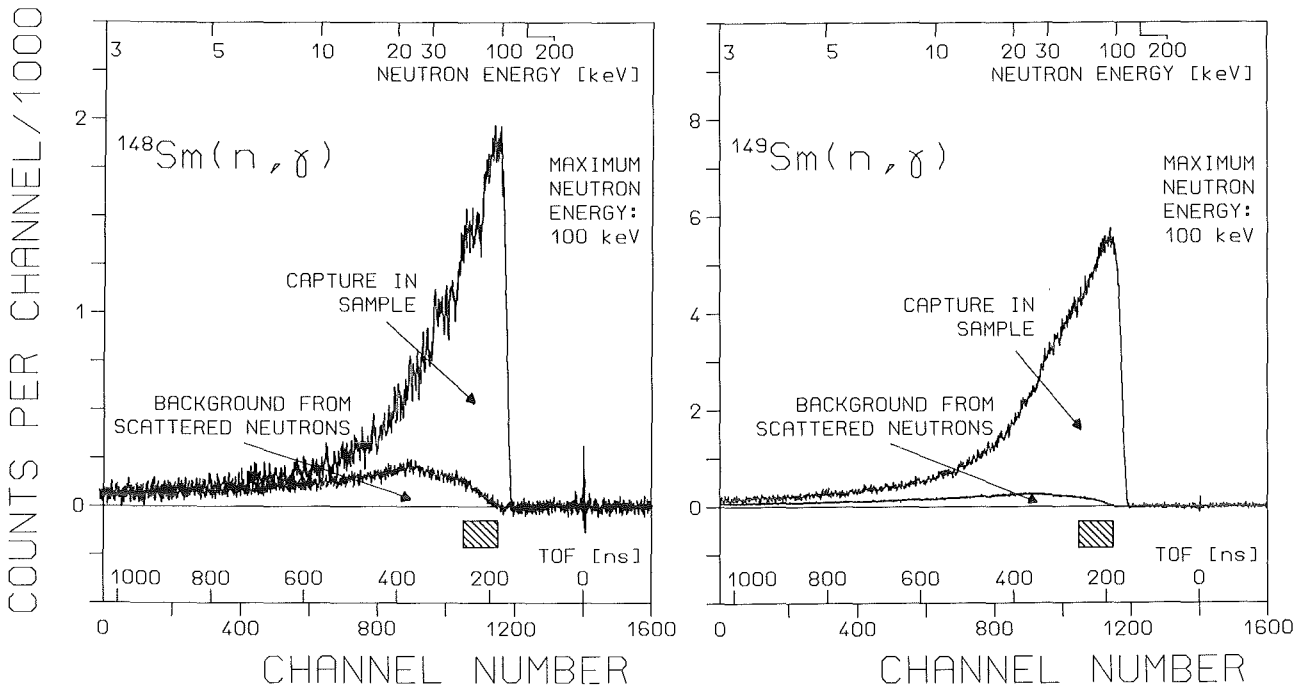


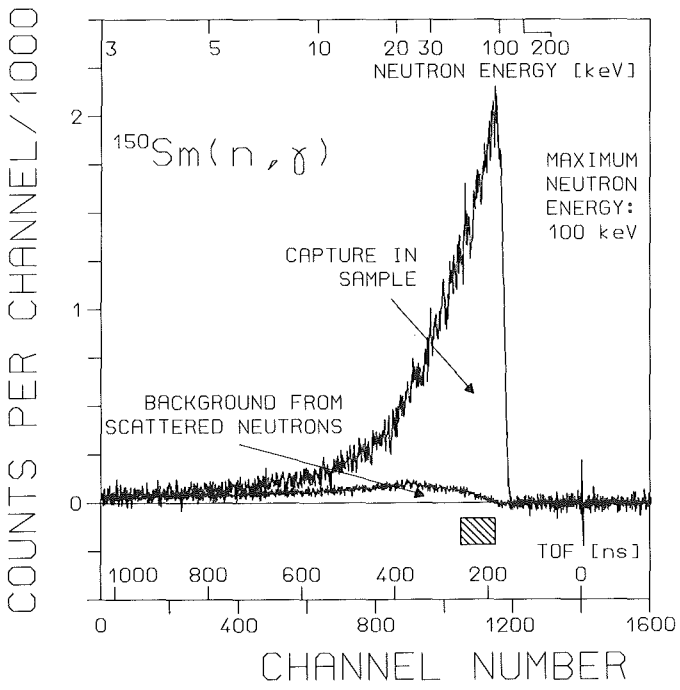


Fig. 8a TOF spectra measured with three samarium samples in run I with 100 keV maximum neutron energy. The background due to capture of sample scattered neutrons is shown separately. The region used for the absolute normalization of the cross section is shown by hatched boxes.

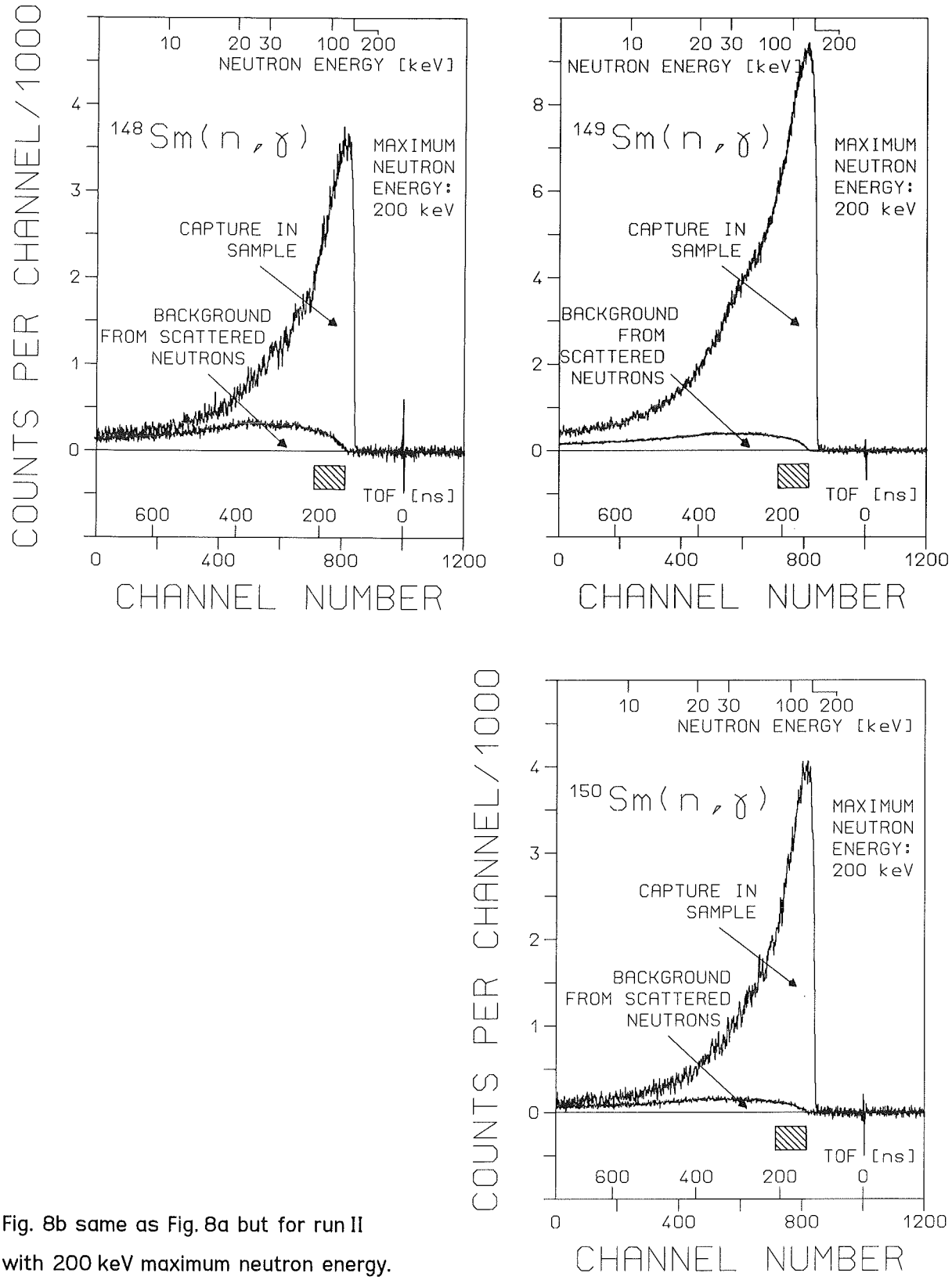


Fig. 8b same as Fig. 8a but for run II with 200 keV maximum neutron energy.

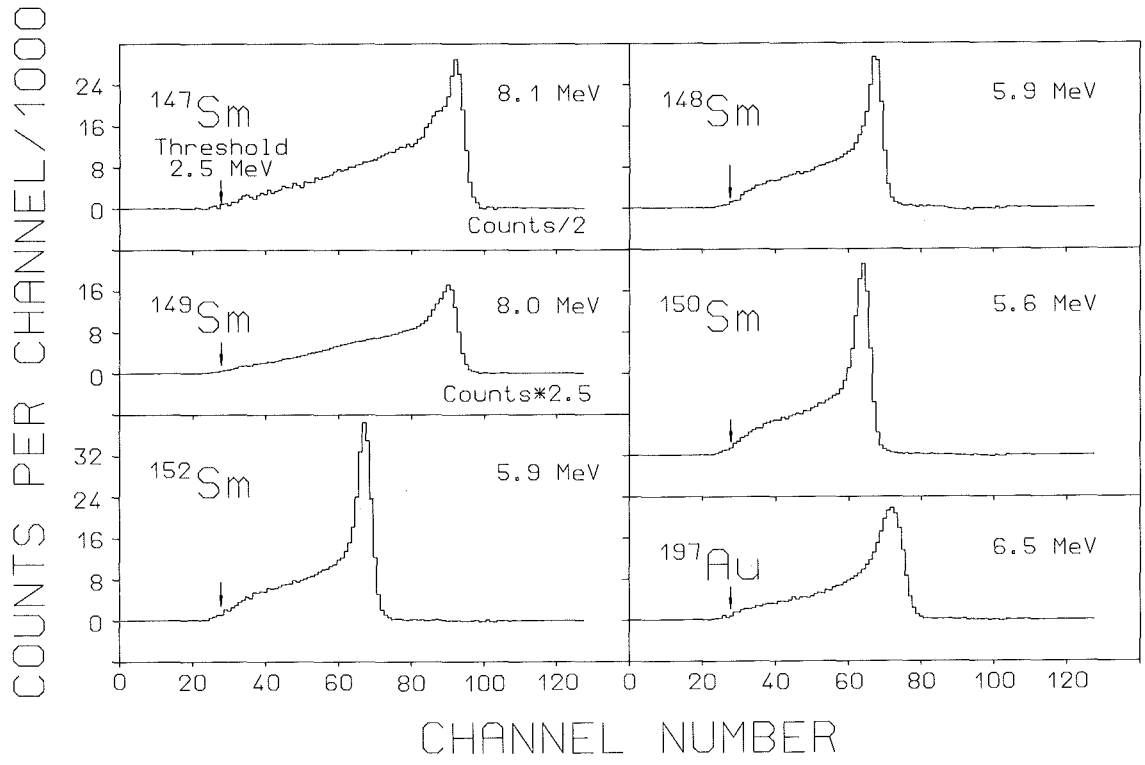


Fig. 9 Sum energy spectra of all isotopes measured in run II containing all events with multiplicity >2. these spectra were obtained by projection of the two-dimensional spectra in the TOF region below the maximum neutron energy as indicated by hached boxes in Fig. 8b.

projected on the sum energy axis in the region of optimum signal to background ratio as indicated by dashed boxes in Fig. 8 . The result is shown in Fig. 9 where the events with multiplicity >2 are plotted for all isotopes.

In Fig. 10 , the sum energy spectra of the s-only isotopes and of the gold standard are shown in dependence of the detector multiplicity. A multiplicity ≧5 is observed for ~40 % of the events in the even and for > 80 % in the odd samarium isotopes. Gamma-ray background affects mainly the spectra with multiplicity 1 and 2, giving rise to large statistical fluctuations below ~3 MeV (channel number 40). These figures demonstrate the potentials of the detector as a multiplicity filter, separating capture events with high multipliciy from gamma-ray background with low multiplicity. An extreme case is found for $^{149}$Sm where the level density is so large that nearly all events are registered with multiplicity ≧5.

The arrows in Fig 10 indicate the range of sum energy channels that were combined to the TOF spectra given in Fig. 8, which were used to determine the cross section shape. Thus the sum energy range below is not used in the evaluation, except in the TOF interval used

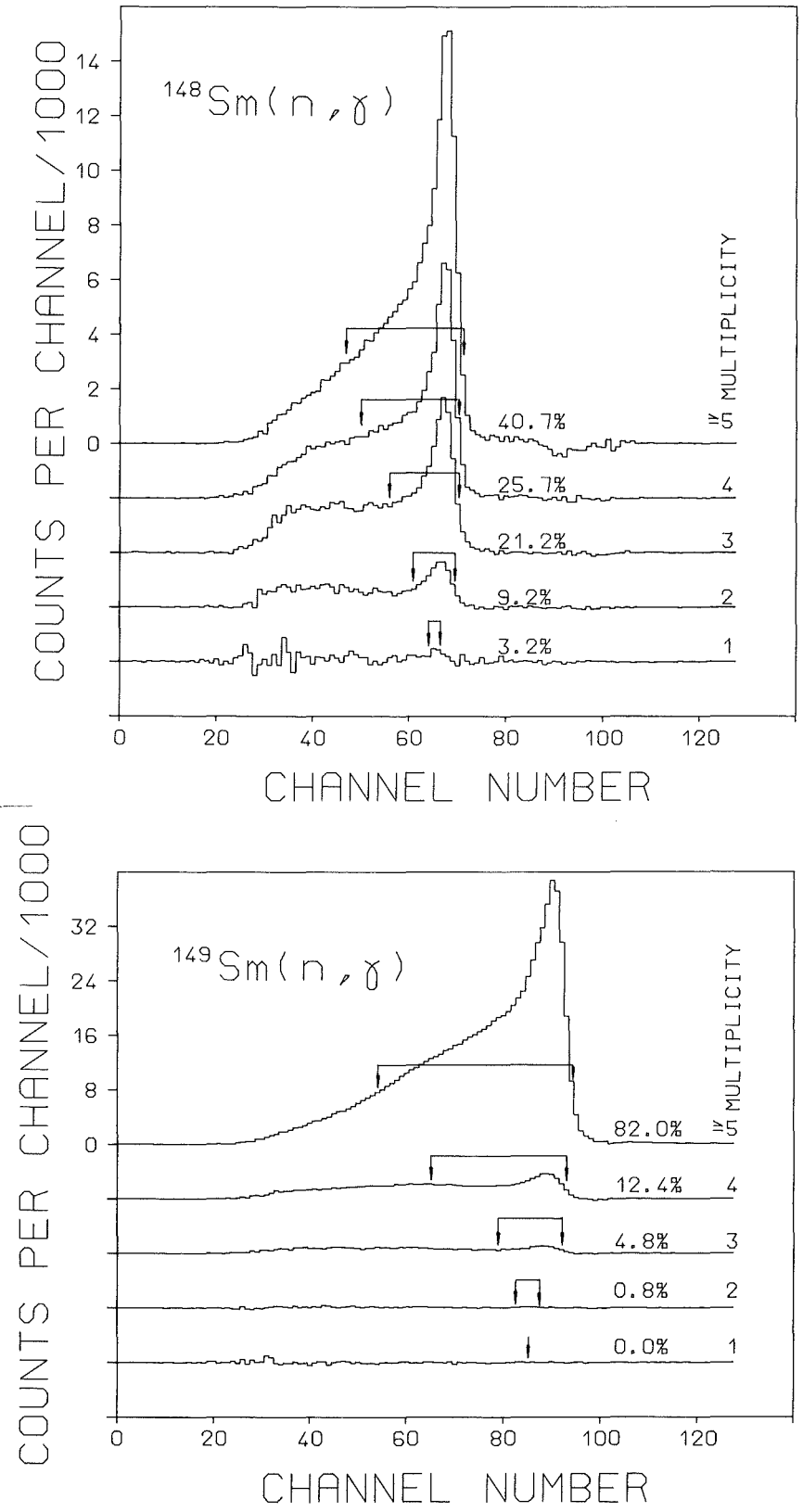


Fig. 10 Sum energy spectra from three samarium isotopes and the gold sample in dependence of detector multiplicity (the same data as shown in Fig. 9). The regions used to determine the cross section shape are indicated by arrows.

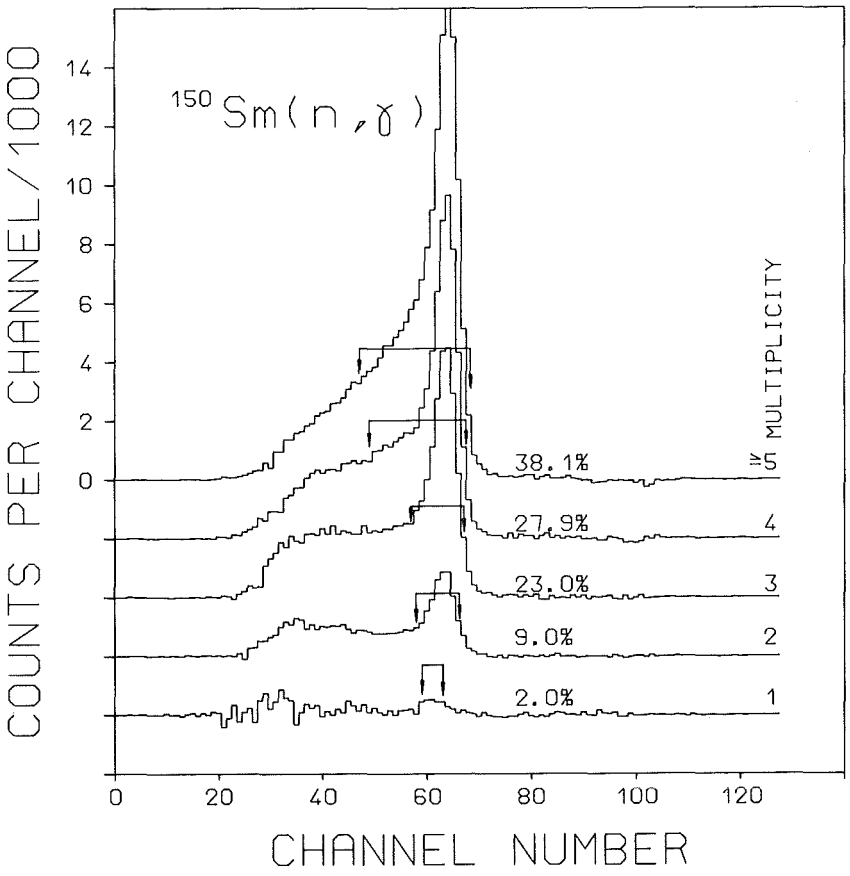
$^{150}$Sm(n,γ)
COUNTS PER CHANNEL/1000
CHANNEL NUMBER
MULTIPLICITY
38.1%
27.9%
23.0%
9.0%
2.0%
5
4
3
2
1

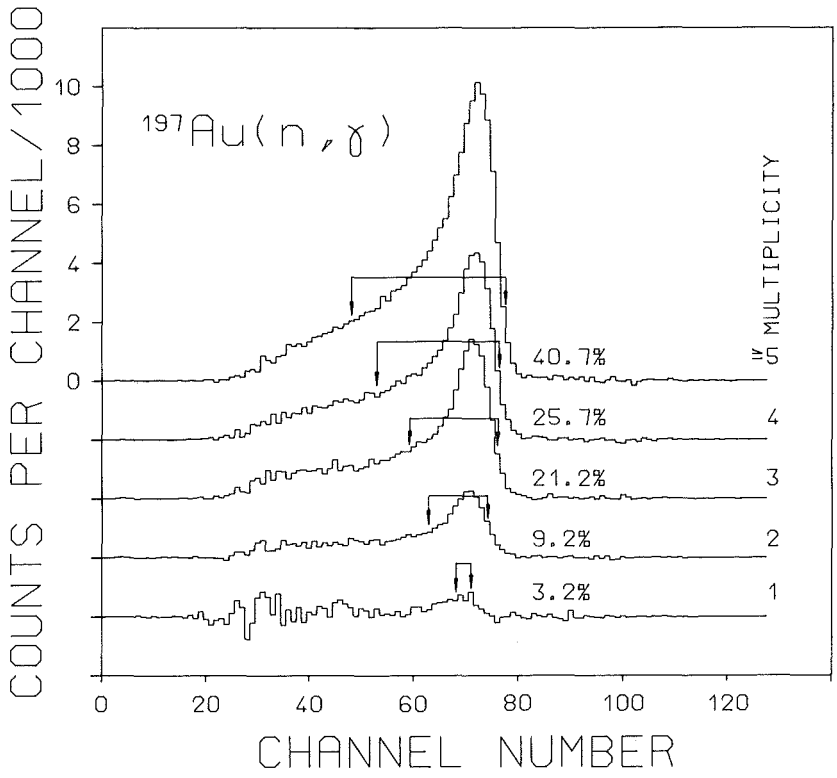
$^{197}$Au(n,γ)
COUNTS PER CHANNEL/1000
CHANNEL NUMBER
MULTIPLICITY
40.7%
25.7%
21.2%
9.2%
3.2%
5
4
3
2
1

for the absolute normalization (dashed box in Fig. 8). The preprocessing of the ADC system rejects these events at low sum energy and large TOF, which are not required for data analysis. In this way, the recorded event rate is reduced by approximately a factor of two (see Fig. 5b).

The cross section ratio of isotope X relative to the gold standard is then:

$$\frac{\sigma_i(X)}{\sigma_i(Au)} = \frac{Z_i(X)}{Z_i(Au)} \times \frac{\Sigma Z(Au)}{\Sigma Z(X)} \times \frac{\Sigma E(X)}{\Sigma E(Au)} \times \frac{m(Au)}{m(X)} \times F_1 \times F_2 . \qquad (1)$$

In this relation, $Z_i$ is the countrate in channel i of the TOF spectrum, $\Sigma Z$ is the integral TOF count rate in the interval used for normalization (see Fig. 8 ), $\Sigma E$ is the total count rate in the sum energy spectrum for all multiplicities summed over the normalization interval (see Fig. 10 ), and m is the sample thickness in atoms/barn. The factor $F_1$ = (100-f(Au))/(100-f(x)) corrects for the capture events f below the experimental threshold in the sum energy, where x refers to the respective samarium sample. (Table X ), and $F_2$ the respective ratio of the multiple scattering and self-shielding corrections (Table XIV ).

The fraction of unobserved capture events, f and the correction factor $F_1$ were calculated as described in detail in Ref. [2] . For this purpose, two informations are necessary: the individual neutron capture cascades and their relative contribution to the total capture cross section as well as the detector efficiency for monoenergetic gamma-rays in the energy range up to 10 MeV.

Capture cascades and capture gamma-ray spectra of the involved isotopes were calculated according to the statistical and optical model [20] . In Table XI, the cross section is given as a function of the cascade multiplicity together with the gamma-ray energies of the 20 most probable cascades. The respective data for gold have been given already in Ref. [2] . The first 20 cascades yield 16 to 23 % of the cross section, but up to 2400 are necessary to cover 95 %. The average multiplicity of the cascades ranges from 3.8 to 5.0 . The corresponding capture gamma-ray spectra are given in Fig. 11 .

The efficiency of a $BaF_2$ shell for monoenergetic gamma-rays was calculated in Ref. [21] with different assumptions for multiple Compton events, resulting in an optimistic and a pessimistic estimate for the peak efficiency, SW(MAX) and SW(MIN). The data given in Ref. [2] were used to calculate the fraction f of unobserved capture events (see Table X).

**TABLE X.** Calculated fraction of unobserved capture events, f (%), and the corresponding correction factors, $F_1$ , for the cross section ratios.

| Sample | Threshold in sum energy [MeV] | | | Assumption for gamma-ray efficiency |
|---|---|---|---|---|
| | 2.0 | 2.4 | 2.5 | |
| Solid angle 94 %, gamma-ray threshold 50 keV | | | | |
| f(Au) | 4.95 | | 6.98 | SW(MAX) |
| f($^{147}$Sm) | 0.55 | | 1.27 | |
| f($^{148}$Sm) | 4.12 | | 7.97 | |
| f($^{149}$Sm) | 1.10 | | 1.76 | |
| f($^{150}$Sm) | 4.69 | | 7.53 | |
| f($^{152}$Sm) | 6.48 | | 8.64 | |
| f(Au) | 5.66 | | 8.11 | SW(MIN) |
| f($^{147}$Sm) | 0.78 | | 1.73 | |
| f($^{148}$Sm) | 5.70 | | 9.50 | |
| f($^{149}$Sm) | 1.29 | | 2.05 | |
| f($^{150}$Sm) | 5.79 | | 9.40 | |
| f($^{152}$Sm) | 7.33 | | 10.22 | |
| $F_1$($^{147}$Sm/Au) | 0.953 | 0.943 | 0.939 | $^1/_2$SW(MAX)+ |
| $F_1$($^{148}$Sm/Au) | 0.996 | 1.008 | 1.013 | $^1/_2$SW(MIN) |
| $F_1$($^{149}$Sm/Au) | 0.958 | 0.947 | 0.943 | |
| $F_1$($^{150}$Sm/Au) | 0.999 | 1.007 | 1.010 | |
| $F_1$($^{152}$Sm/Au) | 1.017 | 1.020 | 1.021 | |

**TABLE XI.** Calculated capture gamma-ray cascades including multiplicities, partial cross sections, $\sigma_p$, and gamma-ray energies of the 20 most significant cascades.

$^{147}Sm$

| | |
|---|---|
| σ(30 keV)=0.950 b | total capture cross section |
| σ(mul 1)=0.0001 b | |
| σ(mul 2)=0.0074 b | |
| σ(mul 3)=0.0949 b | |
| σ(mul 4)=0.2749 b | average multiplicity <m>=4.8 |
| σ(mul 5)=0.3298 b | |
| σ(mul 6)=0.1860 b | |
| σ(mul 7)=0.0568 b | |

calculated number of cascades: 868 (covering 99.5 % of the cross section)

| $\sigma_p$ [mbarn] | $\sigma_p/\sigma_{tot}$ [%] | gamma1 | gamma2 | gamma3 [MeV] | gamma4 | gamma5 |
|---|---|---|---|---|---|---|
| 14.5 | 1.53 | 4.045 | 2.946 | 0.630 | 0.550 | |
| 13.7 | 1.44 | 4.719 | 2.272 | 0.630 | 0.550 | |
| 13.2 | 1.39 | 3.371 | 3.620 | 0.630 | 0.550 | |
| 12.4 | 1.31 | 2.696 | 2.696 | 1.598 | 0.630 | 0.550 |
| 12.0 | 1.26 | 3.371 | 2.696 | 1.554 | 0.550 | |
| 11.7 | 1.23 | 3.371 | 2.022 | 1.598 | 0.630 | 0.550 |
| 11.4 | 1.20 | 4.045 | 3.576 | 0.550 | | |
| 11.3 | 1.19 | 4.719 | 2.902 | 0.550 | | |
| 11.1 | 1.17 | 2.696 | 3.371 | 1.554 | 0.550 | |
| 10.8 | 1.14 | 5.393 | 1.598 | 0.630 | 0.550 | |
| 10.4 | 1.09 | 3.371 | 4.250 | 0.550 | | |
| 10.3 | 1.08 | 4.045 | 2.022 | 1.554 | 0.550 | |
| 10.3 | 1.08 | 2.696 | 4.294 | 0.630 | 0.550 | |
| 10.2 | 1.07 | 5.393 | 2.228 | 0.550 | | |
| 10.0 | 1.05 | 2.696 | 2.696 | 2.228 | 0.550 | |
| 9.74 | 1.03 | 2.696 | 2.022 | 2.272 | 0.630 | 0.550 |
| 9.66 | 1.02 | 3.371 | 2.696 | 0.924 | 0.630 | 0.550 |
| 9.44 | 0.99 | 2.022 | 3.371 | 1.598 | 0.630 | 0.550 |
| 9.02 | 0.95 | 2.022 | 2.696 | 2.272 | 0.630 | 0.550 |
| 8.98 | 0.95 | 3.371 | 2.022 | 2.228 | 0.550 | |
| | Σ 23.2% | | | | | |

**TABLE XI.** (continued)

$^{148}$Sm

σ(30 keV)=0.228 b — total capture cross section
σ(mul 1)=0.0003 b
σ(mul 2)=0.0082 b
σ(mul 3)=0.0507 b
σ(mul 4)=0.0876 b — average multiplicity <m>=4.2
σ(mul 5)=0.0597 b
σ(mul 6)=0.0186 b
σ(mul 7)=0.0029 b

calculated number of cascades: 1000 (covering 95.2 % of the cross section)

| $\sigma_p$ [mbarn] | $\sigma_p/\sigma_{tot}$ [%] | gamma1 | gamma2 | gamma3 [MeV] | gamma4 | gamma5 |
|---|---|---|---|---|---|---|
| 5.58 | 2.45 | 4.780 | 1.098 | 0.023 | | |
| 4.44 | 1.95 | 3.187 | 1.593 | 1.098 | 0.023 | |
| 4.22 | 1.85 | 2.656 | 2.124 | 1.098 | 0.023 | |
| 4.05 | 1.77 | 3.718 | 1.062 | 1.098 | 0.023 | |
| 3.42 | 1.50 | 2.125 | 2.656 | 1.098 | 0.023 | |
| 3.13 | 1.37 | 4.249 | 0.531 | 1.098 | 0.023 | |
| 3.09 | 1.36 | 4.780 | 0.771 | 0.327 | 0.023 | |
| 2.91 | 1.28 | 4.249 | 1.629 | 0.023 | | |
| 2.23 | 0.98 | 3.718 | 2.160 | 0.023 | | |
| 2.22 | 0.97 | 1.593 | 3.187 | 1.098 | 0.023 | |
| 2.09 | 0.92 | 5.551 | 0.327 | 0.023 | | |
| 2.04 | 0.89 | 4.249 | 1.302 | 0.327 | 0.023 | |
| 1.93 | 0.85 | 3.187 | 1.593 | 0.771 | 0.327 | 0.023 |
| 1.91 | 0.84 | 3.187 | 1.593 | 1.121 | | |
| 1.86 | 0.82 | 2.656 | 2.124 | 0.771 | 0.327 | 0.023 |
| 1.84 | 0.81 | 2.656 | 2.124 | 1.121 | | |
| 1.84 | 0.81 | 3.187 | 2.691 | 0.023 | | |
| 1.82 | 0.80 | 3.718 | 1.833 | 0.327 | 0.023 | |
| 1.75 | 0.77 | 3.718 | 1.062 | 0.771 | 0.327 | 0.023 |
| 1.70 | 0.75 | 4.780 | 1.121 | | | |
| | Σ=22.4 % | | | | | |

**TABLE XI.** (continued)

$^{149}$Sm

σ(30 keV)=1.750 b total capture cross section
σ(mul 1)=0.0000 b
σ(mul 2)=0.0073 b
σ(mul 3)=0.1204 b
σ(mul 4)=0.4107 b average multiplicity <m>=5.0
σ(mul 5)=0.6063 b
σ(mul 6)=0.4352 b
σ(mul 7)=0.1705 b

calculated number of cascades: 1442 (covering 95 % of the cross section)

| $\sigma_p$ [mbarn] | $\sigma_p/\sigma_{tot}$ [%] | gamma1 | gamma2 | gamma3 [MeV] | gamma4 | gamma5 |
|---|---|---|---|---|---|---|
| 21.6 | 1.23 | 3.939 | 3.303 | 0.439 | 0.334 | |
| 21.4 | 1.22 | 4.596 | 2.646 | 0.439 | 0.334 | |
| 20.5 | 1.17 | 3.283 | 2.626 | 1.333 | 0.439 | 0.334 |
| 19.7 | 1.13 | 2.626 | 2.626 | 1.990 | 0.439 | 0.334 |
| 19.1 | 1.09 | 3.283 | 3.959 | 0.439 | 0.334 | |
| 18.8 | 1.07 | 2.626 | 3.283 | 1.333 | 0.439 | 0.334 |
| 18.6 | 1.06 | 5.252 | 1.990 | 0.439 | 0.334 | |
| 17.8 | 1.02 | 3.283 | 1.970 | 1.990 | 0.439 | 0.334 |
| 17.4 | 0.99 | 3.939 | 1.969 | 1.333 | 0.439 | 0.334 |
| 15.9 | 0.91 | 3.283 | 2.626 | 1.773 | 0.334 | |
| 15.5 | 0.89 | 1.970 | 3.283 | 1.990 | 0.439 | 0.334 |
| 15.0 | 0.86 | 2.626 | 3.283 | 1.773 | 0.334 | |
| 14.6 | 0.83 | 2.626 | 4.616 | 0.439 | 0.334 | |
| 14.1 | 0.81 | 2.626 | 1.970 | 2.646 | 0.439 | 0.334 |
| 13.5 | 0.77 | 1.970 | 2.626 | 2.646 | 0.439 | 0.334 |
| 13.2 | 0.75 | 3.939 | 1.969 | 1.773 | 0.334 | |
| 13.1 | 0.75 | 1.970 | 3.939 | 1.333 | 0.439 | 0.334 |
| 13.0 | 0.74 | 5.909 | 1.333 | 0.439 | 0.334 | |
| 12.1 | 0.69 | 3.939 | 3.742 | 0.334 | | |
| 12.1 | 0.69 | 4.596 | 3.085 | 0.334 | | |
| | Σ=18.7 % | | | | | |

**TABLE XI.** (continued)

$^{150}Sm$

σ(30 keV)=0.390 b total capture cross section
σ(mul 1)=0.0005 b
σ(mul 2)=0.0154 b
σ(mul 3)=0.0693 b
σ(mul 4)=0.1303 b average multiplicity <m>=4.4
σ(mul 5)=0.1102 b
σ(mul 6)=0.0511 b
σ(mul 7)=0.0132 b

calculated number of cascades: 1740 (covering 95.0 % of the cross section)

| $\sigma_p$ [mbarn] | $\sigma_p/\sigma_{tot}$ [%] | gamma1 | gamma2 | gamma3 [MeV] | gamma4 | gamma5 |
|---|---|---|---|---|---|---|
| 5.79 | 1.48 | 4.797 | 0.824 | 0.005 | | |
| 4.58 | 1.17 | 3.198 | 1.599 | 0.824 | 0.005 | |
| 4.39 | 1.13 | 2.665 | 2.132 | 0.824 | 0.005 | |
| 4.11 | 1.05 | 3.731 | 1.066 | 0.824 | 0.005 | |
| 3.56 | 0.91 | 2.132 | 2.665 | 0.824 | 0.005 | |
| 3.19 | 0.82 | 3.198 | 1.599 | 0.661 | 0.168 | |
| 3.17 | 0.81 | 4.264 | 1.357 | 0.005 | | |
| 3.17 | 0.81 | 4.264 | 0.533 | 0.824 | 0.005 | |
| 3.16 | 0.81 | 4.797 | 0.829 | | | |
| 3.00 | 0.77 | 3.731 | 1.066 | 0.661 | 0.168 | |
| 2.98 | 0.76 | 3.198 | 1.599 | 0.829 | | |
| 2.96 | 0.76 | 2.665 | 2.132 | 0.661 | 0.168 | |
| 2.86 | 0.73 | 2.665 | 2.132 | 0.829 | | |
| 2.85 | 0.73 | 4.797 | 0.661 | 0.168 | | |
| 2.70 | 0.69 | 3.731 | 1.890 | 0.005 | | |
| 2.66 | 0.68 | 3.731 | 1.066 | 0.829 | | |
| 2.44 | 0.63 | 4.264 | 0.533 | 0.661 | 0.168 | |
| 2.35 | 0.60 | 3.198 | 2.423 | 0.005 | | |
| 2.33 | 0.60 | 2.132 | 2.665 | 0.661 | 0.168 | |
| 2.32 | 0.59 | 2.132 | 2.665 | 0.829 | | |
| | Σ=16.5 % | | | | | |

**TABLE XI.** (continued)

$^{152}Sm$

σ(30 keV)=0.480 b total capture cross section
σ(mul 1)=0.0050 b
σ(mul 2)=0.0499 b
σ(mul 3)=0.1459 b
σ(mul 4)=0.1548 b average multiplicity <m>=3.8
σ(mul 5)=0.0876 b
σ(mul 6)=0.0302 b
σ(mul 7)=0.0067 b

calculated number of cascades: 2396 (covering 95.0 % of the cross section)

| $\sigma_p$ [mbarn] | $\sigma_p/\sigma_{tot}$ [%] | gamma1 | gamma2 | gamma3 | gamma4 | gamma5 |
|---|---|---|---|---|---|---|
| | | | | [MeV] | | |
| 5.02 | 1.05 | 5.897 | | | | |
| 4.99 | 1.04 | 5.890 | 0.007 | | | |
| 4.83 | 1.01 | 3.364 | 2.533 | | | |
| 4.77 | 0.99 | 3.364 | 2.526 | 0.007 | | |
| 4.63 | 0.96 | 2.804 | 3.094 | | | |
| 4.59 | 0.96 | 2.804 | 3.087 | 0.007 | | |
| 4.58 | 0.95 | 3.925 | 1.972 | | | |
| 4.54 | 0.95 | 5.784 | 0.113 | | | |
| 4.52 | 0.94 | 3.925 | 1.965 | 0.007 | | |
| 4.22 | 0.88 | 5.046 | 0.851 | | | |
| 4.19 | 0.87 | 4.486 | 1.411 | | | |
| 4.10 | 0.85 | 4.486 | 1.404 | 0.007 | | |
| 4.09 | 0.85 | 5.046 | 0.844 | 0.007 | | |
| 3.99 | 0.83 | 3.364 | 2.420 | 0.113 | | |
| 3.95 | 0.82 | 2.804 | 2.981 | 0.113 | | |
| 3.83 | 0.80 | 2.243 | 3.654 | | | |
| 3.80 | 0.80 | 2.243 | 3.647 | 0.007 | | |
| 3.60 | 0.75 | 3.925 | 1.859 | 0.113 | | |
| 3.34 | 0.70 | 2.243 | 3.541 | 0.113 | | |
| 2.99 | 0.62 | 4.486 | 1.298 | 0.113 | | |
| | Σ=17.6 % | | | | | |

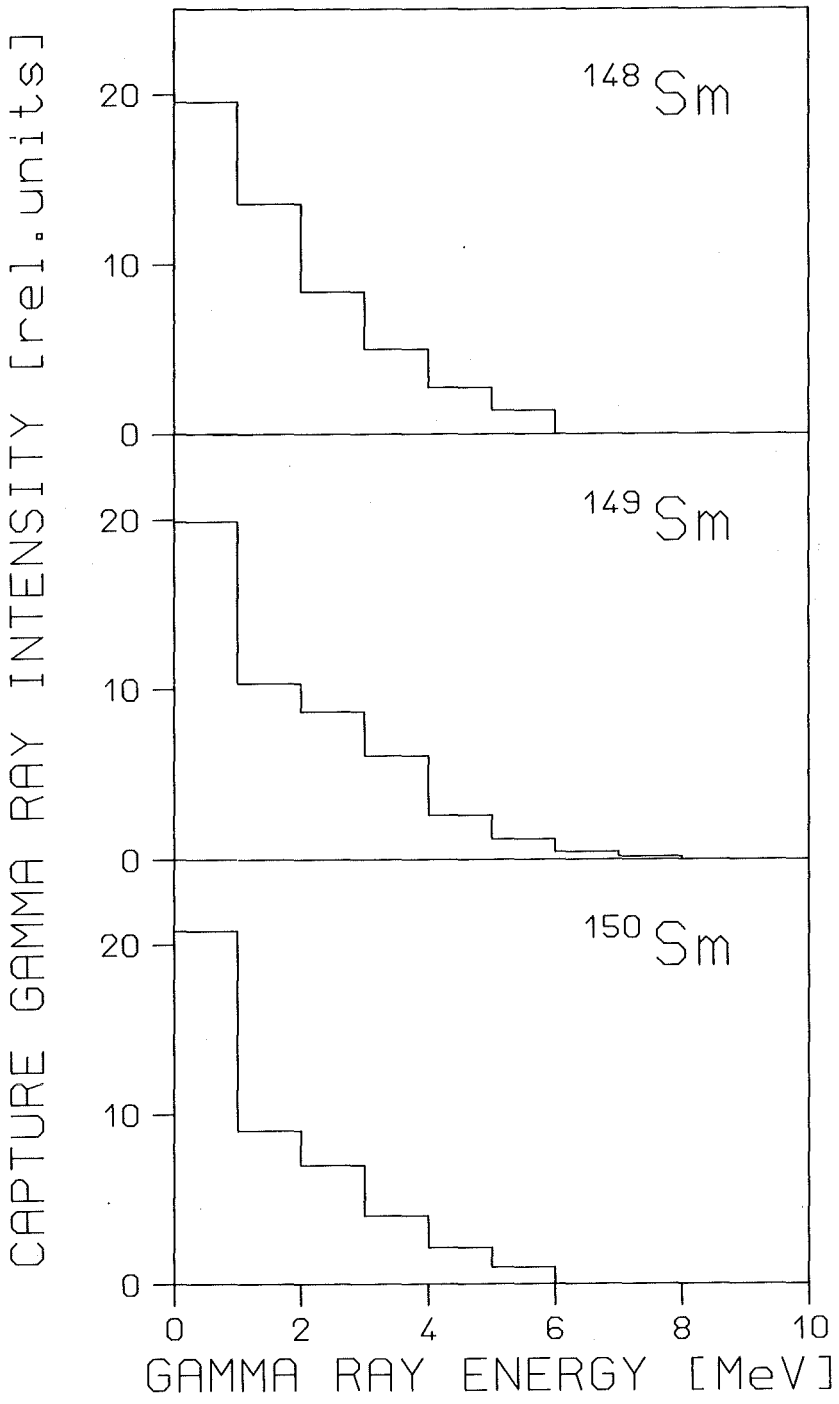


Fig. 11 Calculated capture gamma-ray spectra for three samarium isotopes.

The time to calculate the sum energy spectrum of a capture cascade scales with multiplicity m according to $20^m$ , since each gamma-ray is divided into 20 energy bins [2]. Thus the computer time is completely dominated by the number of cascades with multiplicity 6 and 7. For the tellurium isotopes [6], only a few percent of the cross section is due to cascades with multiplicity 6, but for $^{149}$Sm about ten percent of the cross section involves cascades with multiplicity 7 (see Table XI). Thus the high multiplicity of the capture cascades especially of the odd samarium isotopes prohibited these calculations to be made on the central IBM 3090 M computer of our research centre which was used in the previous work. Instead, we were using a multi-transputer system [22] of our department, which contains 24 T800 transputers each equipped with a working processor and 4 Mbyte RAM memory, sufficient to run rather large codes. The total computing power of this machine is compatible to that of the IBM 3090 M but with the advantage of a single-user machine. Therefore, it was affordable to perform the full calculation for all samarium isotopes. The total computing time for $^{149}$Sm was about 20 days. In addition, it was possible to repeat the calculations for the gold standard with all cascades, which was too expensive in the past [2].

In the actual measurements, we used a threshold in the sum energy of 2.4 MeV in run I and III and of 2.5 MeV in run II . Accordingly, the efficiency of the detector was 98 % for the odd and 92 % for the even isotopes. It has to be noted that for the present experimental method it is not necessary to know the absolute efficiency of the detector, which depends on the efficiency for monoenergetic gamma-rays. As can be seen from Table X , differences of the order of 2 % are observed in the even isotopes for the different assumptions SW(MAX) and SW(MIN). Since sample and standard are measured with the same detector, the final correction factors $F_1$ are practically insensitive to the assumed detector efficiency. For the even isotopes, which have binding energies similar to the gold standard , the correction is very small, and only for the odd isotopes differences in efficiency of several % are found. In Fig. 12, the calculated sum energy spectra are shown separately for the two different assumptions of the detector efficiency. Comparison with Fig. 9 demonstrates that the experimental results are indeed between these two extremes.

The correction for multiple scattering and self-shielding in the sample was calculated with the SESH code [23] . Recently, the code was changed by the author to consider a more accurate formalism for the level density as described in Ref. [2] . In the new version, the nuclear temperature was replaced by the pairing energy $\Delta$ which was taken from Ref. [24] . Now, the level spacings of p- and d-waves are calculated by the program . The main problem is to find parameter sets that reproduce not only the capture cross section, but, the total cross section of each isotope as well.

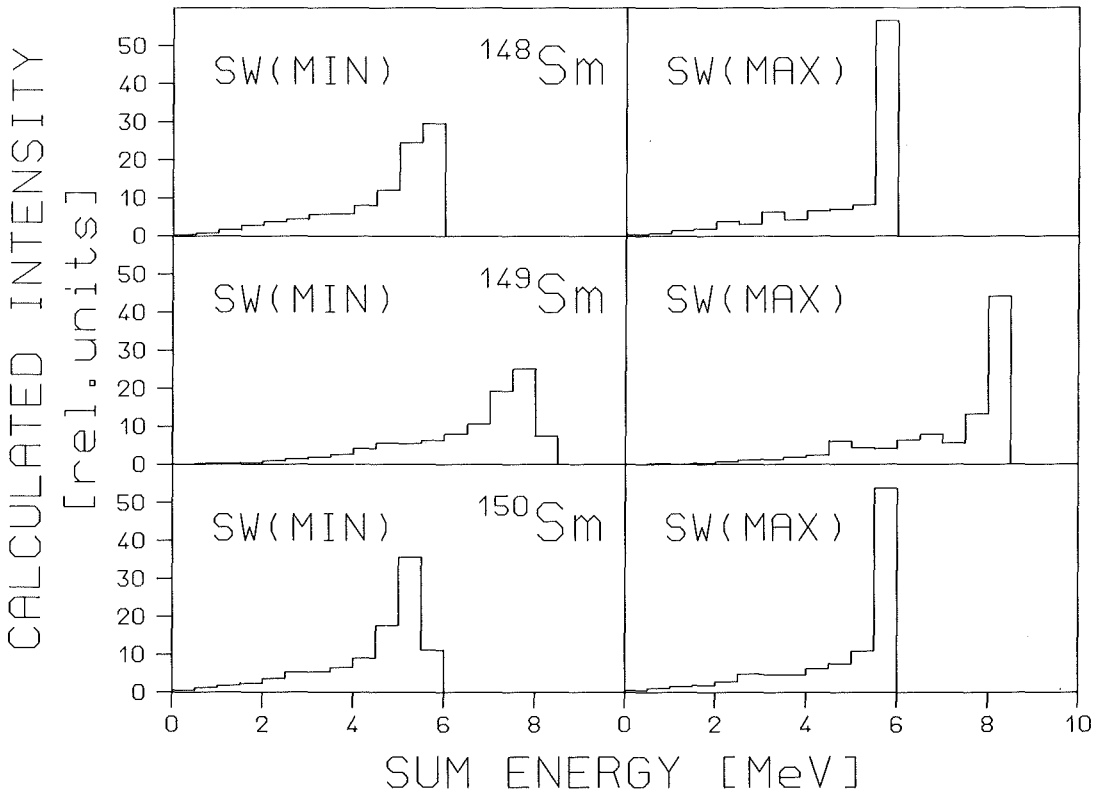


Fig. 12 Calculated sum energy spectra of the $4\pi$ $BaF_2$ detector as obtained under different assumptions on the detector efficiency. These spectra were used to derive the correction $F_1$ for unobserved capture events.

We started from the parameters given by Mughabghab [25] . These data were changed such that the total cross sections of Table VII were reproduced within an uncertainty of ~3 % and our data for the capture cross sections within ~10 %. The respective input parameters as well as the results for the total cross sections are compiled in Table XII . In all calculations oxygen was included assuming the stoichiometry as $Sm_2O_3$. The correction factors MS(X) as well as the correction factors $F_2$ are compiled in Tables XIII and XIV . The comparatively small sample masses used in the present experiment lead to corrections of only ~2 % except for the lowest neutron energies. In the work of Winters et al. [9], the samples were 3 to 4 times more massive, resulting in sizable corrections.

**TABLE XII.** Input parameters for the calculation of neutron multiple scattering and self-shielding corrections with SESH[16].

| Parameter | | Isotope | | | | | | |
|---|---|---|---|---|---|---|---|---|
| | | $^{197}$Au | $^{147}$Sm | $^{148}$Sm | $^{149}$Sm | $^{150}$Sm | $^{152}$Sm | $^{16}$O |
| Nucleon number | | 197 | 147 | 148 | 149 | 150 | 152 | 16 |
| Abundance | | 1 | 1 | 1 | 1 | 1 | 1 | 1.5 |
| Binding energy[MeV] | | 6.513 | 8.141 | 5.871 | 7.985 | 5.596 | 5.867 | 4.144 |
| Pairing energy[MeV] | | 0.0 | 2.14 | 1.22 | 2.21 | 1.22 | 1.22 | 0.0 |
| Effective temperature [K] | | 293 | 293 | 293 | 293 | 293 | 293 | 293 |
| Nuclear spin | | 1.5 | 3.5 | 0 | 3.5 | 0 | 0 | 0 |
| Average | s | 0.128 | 0.069 | 0.045 | 0.065 | 0.120 | 0.100 | 0 |
| radiation width | p | 0.08 | 0.060 | 0.010 | 0.060 | 0.060 | 0.060 | 0 |
| [eV] | d | 0.08 | 0.0062 | 0.014 | 0.0062 | 0.020 | 0.020 | 0 |
| Average | s | 15.5 | 5.7 | 50 | 2.2 | 55 | 51.8 | 0 |
| level spacing | p* | 7.75 | 2.85 | 16.7 | 1.1 | 18.3 | 17.3 | 0 |
| [eV] | d* | 4.96 | 1.9 | 10 | 0.73 | 1.1 | 10.4 | 0 |
| Strength | $S_0$ | 1.8 | 8.0 | 3.0 | 4.8 | 4.5 | 2.2 | 0 |
| function | $S_1$ | 0.4 | 0.8 | 1.9 | 0.5 | 0.2 | 0.55 | 0 |
| [$10^{-4}$] | $S_2$ | 0.4 | 3.0 | 3.5 | 1.53 | 7.0 | 5.3 | 0 |
| Nuclear radius | s | 8.7 | 8.3 | 8.3 | 8.3 | 8.3 | 8.3 | 5.5 |
| [fm] | p,d | 8.0 | 8.3 | 8.3 | 8.3 | 8.3 | 8.3 | |
| Calculated total cross section | | | | | | | | |
| Neutron Energy [keV] | | | | | | | | |
| 3 | | 22.9 | 68.1 | 31.2 | 44.3 | 42.1 | 25.1 | |
| 6 | | 18.8 | 50.0 | 24.5 | 33.4 | 31.8 | 20.0 | |
| 10 | | 16.5 | 39.8 | 20.8 | 27.3 | 26.1 | 17.3 | |
| 20 | | 14.0 | 29.3 | 17.0 | 21.0 | 20.1 | 14.4 | |
| 40 | | 12.1 | 21.2 | 14.1 | 16.1 | 15.5 | 12.1 | |
| 100 | | 9.8 | 13.0 | 11.1 | 10.9 | 10.8 | 9.7 | |
| 200 | | 8.2 | 8.0 | 9.3 | 7.7 | 8.0 | 8.3 | |

* Calculated by SESH code

**TABLE XIII.** Correction factors for neutron multiple scattering and self-shielding, MS.

| Energy range [keV] | MS | | | | | | |
|---|---|---|---|---|---|---|---|
| | Au I | Au II | $^{147}$Sm | $^{148}$Sm | $^{149}$Sm | $^{150}$Sm | $^{152}$Sm |
| 3 - 5 | 0.990 | 0.985 | 1.032 | 0.892 | 1.031 | 0.887 | 0.900 |
| 5 - 7.5 | 1.002 | 1.008 | 1.037 | 0.937 | 1.031 | 0.947 | 0.987 |
| 7.5 - 10 | 1.013 | 1.019 | 1.036 | 0.962 | 1.031 | 0.981 | 0.987 |
| 10 - 12.5 | 1.018 | 1.025 | 1.035 | 0.974 | 1.031 | 0.998 | 1.001 |
| 12.5 - 15 | 1.019 | 1.028 | 1.033 | 0.982 | 1.031 | 0.998 | 1.007 |
| 15 - 20 | 1.019 | 1.028 | 1.031 | 0.991 | 1.031 | 1.010 | 1.014 |
| 20 - 25 | 1.019 | 1.028 | 1.028 | 0.999 | 1.031 | 1.015 | 1.018 |
| 25 - 30 | 1.018 | 1.028 | 1.026 | 1.004 | 1.030 | 1.017 | 1.020 |
| 30 - 40 | 1.016 | 1.026 | 1.023 | 1.009 | 1.030 | 1.019 | 1.021 |
| 40 - 50 | 1.014 | 1.024 | 1.020 | 1.013 | 1.029 | 1.018 | 1.020 |
| 50 - 60 | 1.012 | 1.022 | 1.016 | 1.014 | 1.027 | 1.016 | 1.019 |
| 60 - 80 | 1.010 | 1.019 | 1.013 | 1.014 | 1.024 | 1.013 | 1.017 |
| 80 - 100 | 1.008 | 1.017 | 1.009 | 1.014 | 1.021 | 1.011 | 1.015 |
| 100 - 120 | 1.006 | 1.015 | 1.007 | 1.013 | 1.019 | 1.011 | 1.013 |
| 120 - 150 | 1.005 | 1.013 | 1.006 | 1.012 | 1.017 | 1.011 | 1.012 |
| 150 - 175 | 1.005 | 1.012 | 1.005 | 1.011 | 1.016 | 1.011 | 1.011 |
| 175 - 200 | 1.004 | 1.010 | 1.004 | 1.010 | 1.015 | 1.011 | 1.011 |
| 200 - 225 | 1.004 | 1.009 | 1.004 | 1.009 | 1.015 | 1.010 | 1.010 |

**TABLE XIV.** Correction factor $F_2$ = MS(Au)/MS(X) for the cross section ratio. Two values are given for each ratio corresponding to the gold samples Au I or Au II used in run 1 and runs 2,3, respectively.

| Energy range | Correction for Cross Section Ratio, $F_2$ | | | | |
|---|---|---|---|---|---|
| [keV] | $^{147}$Sm/Au | $^{148}$Sm/Au | $^{149}$Sm/Au | $^{150}$Sm/Au | $^{152}$Sm/Au |
| 3 - 5 | 0.959 0.955 | 1.110 1.104 | 0.960 0.955 | 1.116 1.111 | 1.100 1.094 |
| 5 - 7.5 | 0.966 0.972 | 1.069 1.075 | 0.972 0.978 | 1.058 1.064 | 1.046 1.052 |
| 7.5 - 10 | 0.978 0.984 | 1.053 1.059 | 0.983 0.988 | 1.033 1.039 | 1.026 1.032 |
| 10 - 12.5 | 0.984 0.990 | 1.045 1.052 | 0.987 0.994 | 1.022 1.029 | 1.017 1.024 |
| 12.5 - 15 | 0.986 0.995 | 1.038 1.047 | 0.988 0.997 | 1.021 1.030 | 1.012 1.021 |
| 15 - 20 | 0.988 0.997 | 1.028 1.037 | 0.988 0.997 | 1.009 1.018 | 1.005 1.014 |
| 20 - 25 | 0.991 1.000 | 1.020 1.029 | 0.988 0.997 | 1.004 1.013 | 1.001 1.010 |
| 25 - 30 | 0.992 1.002 | 1.014 1.024 | 0.988 0.998 | 1.001 1.011 | 0.998 1.008 |
| 30 - 40 | 0.993 1.003 | 1.007 1.017 | 0.986 0.996 | 0.997 1.007 | 0.995 1.005 |
| 40 - 50 | 0.994 1.004 | 1.001 1.011 | 0.985 0.995 | 0.996 1.006 | 0.994 1.004 |
| 50 - 60 | 0.996 1.006 | 0.998 1.008 | 0.985 0.995 | 0.996 1.006 | 0.993 1.003 |
| 60 - 80 | 0.997 1.006 | 0.996 1.005 | 0.986 0.995 | 0.997 1.006 | 0.993 1.002 |
| 80 - 100 | 0.999 1.008 | 0.994 1.003 | 0.987 0.996 | 0.997 1.006 | 0.993 1.002 |
| 100 - 120 | 0.999 1.008 | 0.993 1.002 | 0.987 0.996 | 0.995 1.004 | 0.993 1.002 |
| 120 - 150 | 0.999 1.007 | 0.993 1.001 | 0.988 0.996 | 0.994 1.002 | 0.993 1.001 |
| 150 - 175 | 1.000 1.007 | 0.994 1.001 | 0.989 0.996 | 0.994 1.001 | 0.994 1.001 |
| 175 - 200 | 1.000 1.006 | 0.994 1.000 | 0.989 0.995 | 0.993 0.999 | 0.993 0.999 |
| 200 - 225 | 1.000 1.005 | 0.995 1.000 | 0.989 0.994 | 0.994 0.999 | 0.994 0.999 |
| Accuracy [%] | 0.2 | 0.2 | 0.2 | 0.2 | 0.2 |

## IV. RESULTS FOR THE NEUTRON CAPTURE CROSS SECTIONS.

The neutron capture cross section ratios of the samarium isotopes relative to $^{197}$Au are listed together with the respective statistical uncertainties in Tables XV to XIX. The data are given for the three runs and the two evaluations discussed in Sec. III. The last column of the tables contains the weighted average, the weight being determined by the square of the statistical uncertainties. Since the cross section ratios depend weakly on energy, the averages for the energy interval from 30 to 100 keV are also included to allow for a better comparison of the individual results. The statistical uncertainty quoted in this broad energy bin is a lower limit since it is only the uncertainty of the normalization factor from equation 1:

$$N = (\Sigma Z(Au) \times \Sigma E(X)) / (\Sigma Z(X) \times \Sigma E(Au)), \qquad (2)$$

that dominates over the uncertainty of the countrate $Z_i$. No systematic differences can be found in the data as obtained from different evaluations or different runs. This is particularly important for the comparison of runs II and III, which were made with different data acquisition modes.

As in our first experiments [2,6], the results of evaluation 2 were adopted as the final cross section ratios. They are compiled together with statistical, systematic and total uncertainties in Table XX. The chosen energy binning is fine enough to avoid systematic uncertainties in the calculation of the Maxwellian averaged cross sections (see Sec. VI). The final uncertainty in the cross section ratio is of the order of 1 % . This is a significant improvement compared to other experimental techniques.

The experimental ratios were converted into absolute cross sections by means of the gold cross section of Macklin [26] after normalization by a factor of 0.989 to the absolute value of Ratynski and Käppeler[27]. These results are given in Table XXI. If these data are used in further work, their uncertainties can be calculated from the uncertainty of the cross section ratio by adding quadratically the 1.5 % uncertainty of the standard.

If we compare our results with the data known from literature we find the following: The present results are significantly lower compared to the older experiments by Mizumoto for $^{147}$Sm and $^{149}$Sm [28] and by Shaw et al. for $^{149}$Sm [29 ]. In the experiments by Kononov et al. [30,31], all isotopes covered in the present experiment were investigated, and the same behaviour is observed, the discrepancies being up to factors of two. This can not be explained by the systematic uncertainties inherent to different experimental methods but is

**TABLE XV.** The neutron capture cross section ratios $\sigma(^{147}Sm)/\sigma(Au)$, and the respective statistical uncertainties in (%).

| Energy range [keV] | Run I | | Run II | | Run III | | Average | |
|---|---|---|---|---|---|---|---|---|
| Evaluation 1 | | | | | | | | |
| 3 - 5 | 1.3227 | 15.16 | - | - | 1.5088 | 21.0 | 1.3865 | 12.3 |
| 5 - 7.5 | 1.2801 | 8.4 | - | - | 1.4898 | 9.3 | 1.3747 | 6.2 |
| 7.5 - 10 | 1.8322 | 7.0 | 1.7749 | 7.1 | 1.7711 | 7.1 | 1.7931 | 4.1 |
| 10 - 12.5 | 1.5111 | 5.1 | 1.6239 | 5.6 | 1.5575 | 5.7 | 1.5605 | 3.1 |
| 12.5 - 15 | 1.7004 | 4.3 | 1.7284 | 4.7 | 1.9215 | 4.6 | 1.7805 | 2.6 |
| 15 - 20 | 1.6060 | 2.8 | 1.7572 | 2.8 | 1.7547 | 2.9 | 1.7060 | 1.6 |
| 20 - 25 | 1.8429 | 2.4 | 1.8862 | 2.3 | 1.8405 | 2.3 | 1.8576 | 1.3 |
| 25 - 30 | 1.7255 | 2.1 | 1.7506 | 1.9 | 1.8047 | 1.9 | 1.7622 | 1.1 |
| 30 - 40 | 1.6365 | 1.8 | 1.6930 | 1.4 | 1.6884 | 1.5 | 1.6770 | 0.9 |
| 40 - 50 | 1.6718 | 1.8 | 1.7038 | 1.4 | 1.7173 | 1.5 | 1.7004 | 0.9 |
| 50 - 60 | 1.6773 | 1.7 | 1.7503 | 1.4 | 1.7192 | 1.5 | 1.7207 | 0.9 |
| 60 - 80 | 1.6477 | 1.6 | 1.6912 | 1.2 | 1.7138 | 1.3 | 1.6892 | 0.8 |
| 80 - 100 | 1.6729 | 1.7 | 1.6957 | 1.2 | 1.7058 | 1.3 | 1.6945 | 0.8 |
| 100 - 120 | 1.6067 | 2.1 | 1.6594 | 1.2 | 1.6699 | 1.3 | 1.6552 | 0.8 |
| 120 - 150 | - | - | 1.5638 | 1.1 | 1.5792 | 1.2 | 1.5707 | 0.8 |
| 150 - 175 | - | - | 1.5131 | 1.2 | 1.5340 | 1.3 | 1.5226 | 0.9 |
| 175 - 200 | - | | 1.4607 | 1.4 | 1.4857 | 1.3 | 1.4734 | 1.0 |
| 200 - 225 | - | | 1.4411 | 2.0 | 1.5153 | 2.3 | 1.4737 | 1.5 |
| 30 - 100 | 1.6612 | 1.5 | 1.7068 | 0.9 | 1.7089 | 1.1 | 1.6964 | 0.6 |
| Evaluation 2 | | | | | | | | |
| 3 - 5 | 1.4052 | 10.3 | - | - | 1.6331 | 15.3 | 1.4767 | 8.6 |
| 5 - 7.5 | 1.3414 | 6.0 | - | - | 1.5388 | 6.9 | 1.4257 | 4.5 |
| 7.5 - 10 | 1.7402 | 5.1 | 1.8093 | 5.4 | 1.8876 | 5.1 | 1.8118 | 3.0 |
| 10 - 12.5 | 1.4930 | 3.8 | 1.6459 | 4.4 | 1.6263 | 4.1 | 1.5809 | 2.3 |
| 12.5 - 15 | 1.7879 | 3.4 | 1.7913 | 3.7 | 1.9588 | 3.4 | 1.8484 | 2.0 |
| 15 - 20 | 1.6358 | 2.2 | 1.7907 | 2.2 | 1.7781 | 2.1 | 1.7346 | 1.2 |
| 20 - 25 | 1.8142 | 1.9 | 1.9081 | 1.8 | 1.8795 | 1.7 | 1.8687 | 1.0 |
| 25 - 30 | 1.7056 | 1.6 | 1.7417 | 1.5 | 1.7567 | 1.5 | 1.7360 | 0.9 |
| 30 - 40 | 1.6416 | 1.3 | 1.6984 | 1.1 | 1.7036 | 1.2 | 1.6844 | 0.7 |
| 40 - 50 | 1.6662 | 1.3 | 1.6917 | 1.1 | 1.7238 | 1.2 | 1.6954 | 0.7 |
| 50 - 60 | 1.6670 | 1.3 | 1.7462 | 1.1 | 1.7256 | 1.2 | 1.7166 | 0.7 |
| 60 - 80 | 1.6389 | 1.2 | 1.6877 | 0.9 | 1.7220 | 1.0 | 1.6862 | 0.6 |
| 80 - 100 | 1.6601 | 1.2 | 1.6799 | 0.9 | 1.7030 | 1.0 | 1.6829 | 0.6 |
| 100 - 120 | 1.6082 | 1.6 | 1.6469 | 0.9 | 1.6631 | 1.0 | 1.6467 | 0.6 |
| 120 - 150 | - | - | 1.5454 | 0.9 | 1.5717 | 1.0 | 1.5568 | 0.6 |
| 150 - 175 | - | - | 1.4845 | 1.0 | 1.5256 | 1.1 | 1.5028 | 0.7 |
| 175 - 200 | - | - | 1.4294 | 1.1 | 1.4683 | 1.2 | 1.4475 | 0.8 |
| 200 - 225 | - | - | 1.4128 | 1.7 | 1.4763 | 1.8 | 1.4415 | 1.2 |
| 30 - 100 | 1.6548 | 1.0 | 1.7008 | 0.7 | 1.7156 | 0.8 | 1.6931 | 0.5 |

**TABLE XVI.** The neutron capture cross section ratios $\sigma(^{148}Sm)/\sigma(Au)$, and the respective statistical uncertainties in (%).

| Energy range [keV] | Run I | | Run II | | Run III | | Average | |
|---|---|---|---|---|---|---|---|---|
| Evaluation 1 | | | | | | | | |
| 3 - 5 | 0.3422 | 16.2 | - | - | 0.2234 | 33.8 | 0.3199 | 14.8 |
| 5 - 7.5 | 0.3345 | 8.7 | - | - | 0.3369 | 10.3 | 0.3355 | 6.6 |
| 7.5 - 10 | 0.4032 | 7.5 | 0.3569 | 8.0 | 0.2817 | 10.1 | 0.3587 | 4.8 |
| 10 - 12.5 | 0.3282 | 5.6 | 0.3306 | 6.3 | 0.3178 | 6.7 | 0.3260 | 3.5 |
| 12.5 - 15 | 0.3567 | 4.7 | 0.3460 | 5.3 | 0.3596 | 5.4 | 0.3542 | 2.9 |
| 15 - 20 | 0.3807 | 2.8 | 0.3577 | 3.0 | 0.3683 | 3.1 | 0.3695 | 1.7 |
| 20 - 25 | 0.4425 | 2.4 | 0.4271 | 2.2 | 0.4231 | 2.3 | 0.4307 | 1.3 |
| 25 - 30 | 0.3810 | 2.1 | 0.3960 | 1.9 | 0.3953 | 1.9 | 0.3912 | 1.1 |
| 30 - 40 | 0.4122 | 1.6 | 0.4126 | 1.3 | 0.4274 | 1.3 | 0.4179 | 0.8 |
| 40 - 50 | 0.4452 | 1.6 | 0.4469 | 1.2 | 0.4652 | 1.2 | 0.4533 | 0.7 |
| 50 - 60 | 0.4507 | 1.5 | 0.4543 | 1.2 | 0.4602 | 1.2 | 0.4555 | 0.7 |
| 60 - 80 | 0.4598 | 1.4 | 0.4743 | 1.0 | 0.4771 | 1.0 | 0.4725 | 0.6 |
| 80 - 100 | 0.5126 | 1.5 | 0.5310 | 0.9 | 0.5298 | 1.0 | 0.5274 | 0.6 |
| 100 - 120 | 0.5264 | 1.8 | 0.5287 | 0.9 | 0.5421 | 1.0 | 0.5339 | 0.6 |
| 120 - 150 | - | - | 0.5509 | 0.8 | 0.5474 | 0.9 | 0.5493 | 0.6 |
| 150 - 175 | - | - | 0.5541 | 0.9 | 0.5682 | 1.0 | 0.5607 | 0.7 |
| 175 - 200 | - | - | 0.5737 | 1.0 | 0.5825 | 1.1 | 0.5779 | 0.7 |
| 200 - 225 | - | - | 0.5796 | 1.6 | 0.5937 | 1.8 | 0.5857 | 1.1 |
| 30 - 100 | 0.4561 | 1.3 | 0.4638 | 0.6 | 0.4719 | 0.7 | 0.4653 | 0.4 |
| Evaluation 2 | | | | | | | | |
| 3 - 5 | 0.3405 | 11.6 | - | - | 0.2841 | 18.1 | 0.3239 | 9.8 |
| 5 - 7.5 | 0.3114 | 6.7 | - | - | 0.3684 | 6.6 | 0.3401 | 4.7 |
| 7.5 - 10 | 0.3617 | 5.7 | 0.3394 | 6.4 | 0.3281 | 6.0 | 0.3439 | 3.5 |
| 10 - 12.5 | 0.3176 | 4.3 | 0.3485 | 4.7 | 0.3277 | 4.4 | 0.3301 | 2.6 |
| 12.5 - 15 | 0.3718 | 3.7 | 0.3665 | 4.0 | 0.3880 | 3.5 | 0.3763 | 2.1 |
| 15 - 20 | 0.3788 | 2.2 | 0.3707 | 2.4 | 0.3874 | 2.1 | 0.3797 | 1.3 |
| 20 - 25 | 0.4347 | 1.9 | 0.4397 | 1.8 | 0.4355 | 1.6 | 0.4366 | 1.0 |
| 25 - 30 | 0.3785 | 1.6 | 0.3996 | 1.5 | 0.4044 | 1.4 | 0.3953 | 0.9 |
| 30 - 40 | 0.4071 | 1.2 | 0.4183 | 1.0 | 0.4330 | 1.0 | 0.4208 | 0.6 |
| 40 - 50 | 0.4404 | 1.2 | 0.4521 | 1.0 | 0.4680 | 1.0 | 0.4553 | 0.6 |
| 50 - 60 | 0.4452 | 1.2 | 0.4618 | 1.0 | 0.4658 | 1.0 | 0.4588 | 0.6 |
| 60 - 80 | 0.4561 | 1.0 | 0.4721 | 0.8 | 0.4812 | 0.8 | 0.4719 | 0.5 |
| 80 - 100 | 0.5066 | 1.1 | 0.5246 | 0.8 | 0.5298 | 0.8 | 0.5231 | 0.5 |
| 100 - 120 | 0.5182 | 1.5 | 0.5257 | 0.8 | 0.5369 | 0.8 | 0.5295 | 0.5 |
| 120 - 150 | - | - | 0.5446 | 0.7 | 0.5452 | 0.7 | 0.5449 | 0.5 |
| 150 - 175 | - | - | 0.5471 | 0.8 | 0.5641 | 0.8 | 0.5553 | 0.6 |
| 175 - 200 | - | - | 0.5637 | 1.0 | 0.5755 | 0.9 | 0.5696 | 0.6 |
| 200 - 225 | - | - | 0.5719 | 1.4 | 0.5846 | 1.4 | 0.5779 | 1.0 |
| 30 - 100 | 0.4511 | 0.9 | 0.4658 | 0.5 | 0.4756 | 0.5 | 0.4660 | 0.3 |

**TABLE XVII.** The neutron capture cross section ratios $\sigma(^{149}Sm)/\sigma(Au)$, and the respective statistical uncertainties in (%).

| Energy range [keV] | Run I | | Run II | | Run III | | Average | |
|---|---|---|---|---|---|---|---|---|
| Evaluation 1 | | | | | | | | |
| 3 - 5 | 3.3987 | 10.9 | - | - | 3.0969 | 13.8 | 3.2817 | 8.6 |
| 5 - 7.5 | 3.0448 | 6.0 | - | - | 3.2447 | 6.0 | 3.1431 | 4.2 |
| 7.5 - 10 | 3.8852 | 5.7 | 3.4226 | 4.8 | 3.2960 | 5.1 | 3.5073 | 3.0 |
| 10 - 12.5 | 3.2428 | 3.9 | 3.4290 | 3.6 | 3.2744 | 3.8 | 3.3197 | 2.2 |
| 12.5 - 15 | 3.5238 | 3.4 | 3.4015 | 3.1 | 3.5400 | 3.3 | 3.4844 | 1.9 |
| 15 - 20 | 3.4423 | 2.2 | 3.4081 | 1.9 | 3.4755 | 2.0 | 3.4406 | 1.1 |
| 20 - 25 | 3.6613 | 1.9 | 3.4916 | 1.6 | 3.6226 | 1.6 | 3.5811 | 1.0 |
| 25 - 30 | 3.1384 | 1.7 | 3.1949 | 1.3 | 3.2692 | 1.3 | 3.2090 | 0.8 |
| 30 - 40 | 2.9436 | 1.4 | 2.9551 | 0.9 | 3.0026 | 1.0 | 2.9709 | 0.6 |
| 40 - 50 | 2.9421 | 1.4 | 2.9833 | 0.9 | 3.0256 | 1.0 | 2.9914 | 0.6 |
| 50 - 60 | 2.8431 | 1.4 | 2.9113 | 0.9 | 2.9249 | 1.0 | 2.9029 | 0.6 |
| 60 - 80 | 2.8045 | 1.3 | 2.8345 | 0.8 | 2.8545 | 0.8 | 2.8373 | 0.5 |
| 80 - 100 | 2.8411 | 1.3 | 2.8720 | 0.8 | 2.8733 | 0.8 | 2.8678 | 0.5 |
| 100 - 120 | 2.7627 | 1.6 | 2.7821 | 0.8 | 2.8188 | 0.8 | 2.7948 | 0.5 |
| 120 - 150 | - | - | 2.7606 | 0.7 | 2.7716 | 0.8 | 2.7656 | 0.5 |
| 150 - 175 | - | - | 2.7497 | 0.8 | 2.7879 | 0.8 | 2.7672 | 0.6 |
| 175 - 200 | - | - | 2.7838 | 0.9 | 2.8090 | 0.9 | 2.7957 | 0.6 |
| 200 - 225 | - | - | 2.7861 | 1.3 | 2.8715 | 1.5 | 2.8224 | 1.0 |
| 30 - 100 | 2.8749 | 1.2 | 2.9112 | 0.5 | 2.9362 | 0.6 | 2.9141 | 0.4 |
| Evaluation 2 | | | | | | | | |
| 3 - 5 | 3.2525 | 7.7 | - | - | 3.4906 | 9.6 | 3.3462 | 6.0 |
| 5 - 7.5 | 2.9881 | 4.3 | - | - | 3.5022 | 4.3 | 3.2470 | 3.0 |
| 7.5 - 10 | 3.6589 | 4.1 | 3.4887 | 3.7 | 3.6072 | 3.6 | 3.5806 | 2.1 |
| 10 - 12.5 | 3.1960 | 2.9 | 3.4974 | 2.8 | 3.4676 | 2.6 | 3.3920 | 1.6 |
| 12.5 - 15 | 3.6653 | 2.7 | 3.5719 | 2.5 | 3.7073 | 2.4 | 3.6492 | 1.4 |
| 15 - 20 | 3.4849 | 1.7 | 3.5194 | 1.5 | 3.5785 | 1.4 | 3.5323 | 0.9 |
| 20 - 25 | 3.6177 | 1.5 | 3.5750 | 1.3 | 3.6637 | 1.2 | 3.6205 | 0.7 |
| 25 - 30 | 3.1065 | 1.3 | 3.1911 | 1.1 | 3.2431 | 1.0 | 3.1905 | 0.6 |
| 30 - 40 | 2.9528 | 1.0 | 3.0144 | 0.8 | 3.0552 | 0.8 | 3.0174 | 0.5 |
| 40 - 50 | 2.9336 | 1.0 | 3.0023 | 0.8 | 3.0457 | 0.8 | 3.0039 | 0.5 |
| 50 - 60 | 2.8401 | 1.0 | 2.9450 | 0.8 | 2.9584 | 0.8 | 2.9253 | 0.5 |
| 60 - 80 | 2.8065 | 0.9 | 2.8515 | 0.6 | 2.8820 | 0.7 | 2.8542 | 0.4 |
| 80 - 100 | 2.8310 | 0.9 | 2.8721 | 0.6 | 2.8929 | 0.6 | 2.8729 | 0.4 |
| 100 - 120 | 2.7541 | 1.3 | 2.7840 | 0.6 | 2.8033 | 0.6 | 2.7887 | 0.4 |
| 120 - 150 | - | - | 2.7463 | 0.6 | 2.7670 | 0.6 | 2.7562 | 0.4 |
| 150 - 175 | - | - | 2.7324 | 0.7 | 2.7842 | 0.7 | 2.7572 | 0.5 |
| 175 - 200 | - | - | 2.7431 | 0.8 | 2.7911 | 0.8 | 2.7671 | 0.5 |
| 200 - 225 | - | - | 2.7490 | 1.1 | 2.8255 | 1.2 | 2.7841 | 0.8 |
| 30 - 100 | 2.8728 | 0.7 | 2.9371 | 0.4 | 2.9668 | 0.4 | 2.9347 | 0.3 |

**TABLE XVIII.** The neutron capture cross section ratios $\sigma(^{150}Sm)/\sigma(Au)$, and the respective statistical uncertainties in (%).

| Energy range [keV] | Run I | | Run II | | Run III | | Average | |
|---|---|---|---|---|---|---|---|---|
| Evaluation 1 | | | | | | | | |
| 3 - 5 | 0.5817 | 15.4 | - | - | 0.6377 | 20.9 | 0.6014 | 12.4 |
| 5 - 7.5 | 0.5201 | 8.5 | - | - | 0.5817 | 9.3 | 0.5483 | 6.3 |
| 7.5 - 10 | 0.6385 | 7.3 | 0.5877 | 7.2 | 0.5752 | 7.7 | 0.6012 | 4.2 |
| 10 - 12.5 | 0.5650 | 5.1 | 0.5700 | 5.4 | 0.5883 | 5.5 | 0.5739 | 3.1 |
| 12.5 - 15 | 0.6628 | 4.2 | 0.6231 | 4.4 | 0.6482 | 4.7 | 0.6452 | 2.5 |
| 15 - 20 | 0.6579 | 2.6 | 0.6241 | 2.6 | 0.6807 | 2.7 | 0.6540 | 1.5 |
| 20 - 25 | 0.7814 | 2.2 | 0.7459 | 2.0 | 0.7778 | 2.0 | 0.7673 | 1.2 |
| 25 - 30 | 0.6650 | 1.9 | 0.6462 | 1.7 | 0.6731 | 1.7 | 0.6612 | 1.0 |
| 30 - 40 | 0.7016 | 1.5 | 0.6812 | 1.2 | 0.7141 | 1.2 | 0.6982 | 0.7 |
| 40 - 50 | 0.7734 | 1.5 | 0.7789 | 1.1 | 0.7829 | 1.1 | 0.7792 | 0.7 |
| 50 - 60 | 0.7704 | 1.5 | 0.7848 | 1.1 | 0.7921 | 1.1 | 0.7841 | 0.7 |
| 60 - 80 | 0.8129 | 1.3 | 0.8106 | 0.9 | 0.8204 | 0.9 | 0.8147 | 0.6 |
| 80 - 100 | 0.8869 | 1.4 | 0.8942 | 0.8 | 0.9090 | 0.9 | 0.8987 | 0.6 |
| 100 - 120 | 0.9075 | 1.9 | 0.9037 | 0.9 | 0.9210 | 0.9 | 0.9113 | 0.6 |
| 120 - 150 | - | - | 0.9648 | 0.8 | 0.9765 | 0.8 | 0.9703 | 0.6 |
| 150 - 175 | - | - | 0.9765 | 0.9 | 1.0036 | 0.9 | 0.9892 | 0.6 |
| 175 - 200 | - | - | 1.0038 | 1.0 | 1.0424 | 1.0 | 1.0228 | 0.7 |
| 200 - 225 | - | - | 1.0442 | 1.5 | 1.0443 | 1.7 | 1.0442 | 1.1 |
| 30 - 100 | 0.7890 | 1.2 | 0.7899 | 0.6 | 0.8037 | 0.6 | 0.7950 | 0.4 |
| Evaluation 2 | | | | | | | | |
| 3 - 5 | 0.5194 | 12.1 | - | - | 0.5608 | 15.3 | 0.5353 | 9.5 |
| 5 - 7.5 | 0.4887 | 6.7 | - | - | 0.6107 | 6.0 | 0.5561 | 4.5 |
| 7.5 - 10 | 0.6169 | 5.5 | 0.5767 | 5.6 | 0.6243 | 4.9 | 0.6078 | 3.0 |
| 10 - 12.5 | 0.5636 | 3.9 | 0.5934 | 4.2 | 0.6131 | 3.6 | 0.5913 | 2.2 |
| 12.5 - 15 | 0.6863 | 3.4 | 0.6560 | 3.5 | 0.6894 | 3.1 | 0.6783 | 1.9 |
| 15 - 20 | 0.6491 | 2.1 | 0.6522 | 2.1 | 0.6917 | 1.8 | 0.6667 | 1.1 |
| 20 - 25 | 0.7711 | 1.7 | 0.7517 | 1.6 | 0.7844 | 1.4 | 0.7700 | 0.9 |
| 25 - 30 | 0.6569 | 1.5 | 0.6487 | 1.4 | 0.6742 | 1.3 | 0.6610 | 0.8 |
| 30 - 40 | 0.7019 | 1.2 | 0.6947 | 1.0 | 0.7262 | 0.9 | 0.7089 | 0.6 |
| 40 - 50 | 0.7670 | 1.2 | 0.7787 | 1.0 | 0.7849 | 0.9 | 0.7781 | 0.6 |
| 50 - 60 | 0.7664 | 1.1 | 0.7879 | 1.0 | 0.7928 | 0.9 | 0.7840 | 0.5 |
| 60 - 80 | 0.8068 | 1.0 | 0.8104 | 0.8 | 0.8206 | 0.7 | 0.8134 | 0.5 |
| 80 - 100 | 0.8815 | 1.0 | 0.8885 | 0.7 | 0.9078 | 0.7 | 0.8946 | 0.5 |
| 100 - 120 | 0.9013 | 1.5 | 0.9003 | 0.8 | 0.9106 | 0.7 | 0.9048 | 0.5 |
| 120 - 150 | - | - | 0.9548 | 0.7 | 0.9713 | 0.7 | 0.9625 | 0.5 |
| 150 - 175 | - | - | 0.9646 | 0.8 | 0.9982 | 0.8 | 0.9808 | 0.5 |
| 175 - 200 | - | - | 0.9874 | 0.9 | 1.0320 | 0.9 | 1.0100 | 0.6 |
| 200 - 225 | - | - | 1.0261 | 1.3 | 1.0301 | 1.4 | 1.0279 | 0.9 |
| 30 - 100 | 0.7847 | 0.8 | 0.7920 | 0.5 | 0.8065 | 0.5 | 0.7958 | 0.3 |

**TABLE XIX.** The neutron capture cross section ratios $\sigma(^{152}Sm)/\sigma(Au)$, and the respective statistical uncertainties in (%).

| Energy range [keV] | Run I | | Run II | | Run III | | Average | |
|---|---|---|---|---|---|---|---|---|
| Evaluation 1 | | | | | | | | |
| 3 - 5 | 0.6514 | 12.7 | - | - | 0.6290 | 18.4 | 0.6442 | 10.5 |
| 5 - 7.5 | 0.5617 | 7.2 | - | - | 0.6351 | 7.8 | 0.5952 | 5.3 |
| 7.5 - 10 | 0.7509 | 6.3 | 0.7197 | 5.9 | 0.6898 | 6.2 | 0.7199 | 3.5 |
| 10 - 12.5 | 0.6746 | 4.4 | 0.6725 | 4.6 | 0.6851 | 4.7 | 0.6772 | 2.6 |
| 12.5 - 15 | 0.7196 | 3.8 | 0.6972 | 3.9 | 0.7260 | 4.0 | 0.7141 | 2.2 |
| 15 - 20 | 0.7826 | 2.4 | 0.7664 | 2.3 | 0.7886 | 2.3 | 0.7789 | 1.3 |
| 20 - 25 | 0.9222 | 2.1 | 0.8825 | 1.8 | 0.8998 | 1.8 | 0.8996 | 1.1 |
| 25 - 30 | 0.8415 | 1.8 | 0.8522 | 1.5 | 0.8854 | 1.5 | 0.8616 | 0.9 |
| 30 - 40 | 0.8767 | 1.5 | 0.8621 | 1.1 | 0.8956 | 1.0 | 0.8781 | 0.6 |
| 40 - 50 | 0.8917 | 1.5 | 0.8823 | 1.1 | 0.9069 | 1.1 | 0.8936 | 0.6 |
| 50 - 60 | 0.9274 | 1.4 | 0.9434 | 1.1 | 0.9582 | 1.1 | 0.9454 | 0.6 |
| 60 - 80 | 0.9265 | 1.3 | 0.9250 | 0.9 | 0.9487 | 0.9 | 0.9344 | 0.5 |
| 80 - 100 | 0.9903 | 1.4 | 0.9963 | 0.8 | 1.0072 | 0.9 | 0.9995 | 0.5 |
| 100 - 120 | 0.9848 | 1.7 | 0.9882 | 0.8 | 1.0163 | 0.9 | 0.9994 | 0.5 |
| 120 - 150 | - | - | 0.8090 | 0.8 | 0.8443 | 0.9 | 0.8254 | 0.6 |
| 150 - 175 | - | - | 0.6907 | 0.9 | 0.7190 | 1.0 | 0.7040 | 0.7 |
| 175 - 200 | - | - | 0.6492 | 1.1 | 0.6647 | 1.1 | 0.6569 | 0.7 |
| 200 - 225 | - | - | 0.6089 | 1.7 | 0.6400 | 1.8 | 0.6228 | 1.2 |
| 30 - 100 | 0.9225 | 1.2 | 0.9218 | 0.6 | 0.9433 | 0.6 | 0.9302 | 0.4 |
| Evaluation 2 | | | | | | | | |
| 3 - 5 | 0.6327 | 9.3 | - | - | 0.6915 | 12.4 | 0.6537 | 7.4 |
| 5 - 7.5 | 0.5442 | 5.4 | - | - | 0.6404 | 5.4 | 0.5922 | 3.8 |
| 7.5 - 10 | 0.7011 | 4.7 | 0.6822 | 4.7 | 0.7238 | 4.3 | 0.7036 | 2.6 |
| 10 - 12.5 | 0.6545 | 3.3 | 0.6899 | 3.6 | 0.7112 | 3.2 | 0.6858 | 1.9 |
| 12.5 - 15 | 0.7349 | 3.1 | 0.7189 | 3.1 | 0.7439 | 2.8 | 0.7333 | 1.7 |
| 15 - 20 | 0.7704 | 1.9 | 0.7788 | 1.8 | 0.7962 | 1.6 | 0.7829 | 1.0 |
| 20 - 25 | 0.9007 | 1.6 | 0.8873 | 1.5 | 0.9031 | 1.3 | 0.8972 | 0.8 |
| 25 - 30 | 0.8321 | 1.4 | 0.8359 | 1.2 | 0.8727 | 1.1 | 0.8495 | 0.7 |
| 30 - 40 | 0.8684 | 1.1 | 0.8659 | 0.9 | 0.9070 | 0.8 | 0.8829 | 0.5 |
| 40 - 50 | 0.8753 | 1.1 | 0.8787 | 0.9 | 0.9022 | 0.8 | 0.8871 | 0.5 |
| 50 - 60 | 0.9115 | 1.1 | 0.9388 | 0.9 | 0.9564 | 0.8 | 0.9384 | 0.5 |
| 60 - 80 | 0.9146 | 0.9 | 0.9140 | 0.7 | 0.9464 | 0.7 | 0.9264 | 0.4 |
| 80 - 100 | 0.9774 | 1.0 | 0.9797 | 0.7 | 0.9995 | 0.7 | 0.9871 | 0.4 |
| 100 - 120 | 0.9707 | 1.4 | 0.9766 | 0.7 | 1.0008 | 0.7 | 0.9864 | 0.5 |
| 120 - 150 | - | - | 0.7918 | 0.7 | 0.8418 | 0.7 | 0.8161 | 0.5 |
| 150 - 175 | - | - | 0.6749 | 0.8 | 0.7105 | 0.8 | 0.6921 | 0.6 |
| 175 - 200 | - | - | 0.6333 | 1.0 | 0.6531 | 0.9 | 0.6434 | 0.7 |
| 200 - 225 | - | - | 0.5934 | 1.5 | 0.6279 | 1.5 | 0.6101 | 1.0 |
| 30 - 100 | 0.9094 | 0.8 | 0.9154 | 0.5 | 0.9423 | 0.5 | 0.9244 | 0.3 |

**TABLE XX.** The final neutron capture cross section ratios of $^{147}Sm$, $^{148}Sm$, $^{149}Sm$, $^{150}Sm$, and $^{152}Sm$ relative to $^{197}Au$ together with the statistical and systematic uncertainties in (%) [a].

| Energy [keV] | $\sigma(^{147}Sm)/\sigma(^{197}Au)$ | uncertainty stat | sys | tot | $\sigma(^{148}Sm)/\sigma(^{197}Au)$ | uncertainty stat | sys | tot | $\sigma(^{149}Sm)/\sigma(^{197}Au)$ | uncertainty stat | sys | tot |
|---|---|---|---|---|---|---|---|---|---|---|---|---|
| 3 - 5 | 1.4767 | 8.6 | 0.7 | 8.6 | 0.3239 | 9.8 | 0.7 | 9.8 | 3.3462 | 6.0 | 0.7 | 6.0 |
| 5 - 7.5 | 1.4257 | 4.5 | 0.7 | 4.5 | 0.3401 | 4.7 | 0.7 | 4.7 | 3.2470 | 3.0 | 0.7 | 3.1 |
| 7.5 - 10 | 1.8118 | 3.0 | 0.7 | 3.1 | 0.3439 | 3.5 | 0.7 | 3.5 | 3.5806 | 2.1 | 0.7 | 2.2 |
| 10 - 12.5 | 1.5809 | 2.3 | 0.7 | 2.4 | 0.3301 | 2.6 | 0.7 | 2.7 | 3.3920 | 1.6 | 0.7 | 1.7 |
| 12.5 - 15 | 1.8484 | 2.0 | 0.7 | 2.1 | 0.3763 | 2.1 | 0.7 | 2.2 | 3.6492 | 1.4 | 0.7 | 1.6 |
| 15 - 20 | 1.7346 | 1.2 | 0.7 | 1.4 | 0.3797 | 1.3 | 0.7 | 1.5 | 3.5323 | 0.9 | 0.7 | 1.1 |
| 20 - 25 | 1.8687 | 1.0 | 0.7 | 1.2 | 0.4366 | 1.0 | 0.7 | 1.2 | 3.6205 | 0.7 | 0.7 | 1.0 |
| 25 - 30 | 1.7360 | 0.9 | 0.7 | 1.1 | 0.3953 | 0.9 | 0.7 | 1.1 | 3.1905 | 0.6 | 0.7 | 0.9 |
| 30 - 40 | 1.6844 | 0.7 | 0.7 | 1.0 | 0.4208 | 0.6 | 0.7 | 0.9 | 3.0174 | 0.5 | 0.7 | 0.9 |
| 40 - 50 | 1.6954 | 0.7 | 0.7 | 1.0 | 0.4553 | 0.6 | 0.7 | 0.9 | 3.0039 | 0.5 | 0.7 | 0.9 |
| 50 - 60 | 1.7166 | 0.7 | 0.7 | 1.0 | 0.4588 | 0.6 | 0.7 | 0.9 | 2.9253 | 0.5 | 0.7 | 0.9 |
| 60 - 80 | 1.6862 | 0.6 | 0.7 | 0.9 | 0.4719 | 0.5 | 0.7 | 0.9 | 2.8542 | 0.4 | 0.7 | 0.8 |
| 80 - 100 | 1.6829 | 0.6 | 0.7 | 0.9 | 0.5231 | 0.5 | 0.7 | 0.9 | 2.8729 | 0.4 | 0.7 | 0.8 |
| 100 - 120 | 1.6467 | 0.6 | 0.7 | 0.9 | 0.5295 | 0.5 | 0.7 | 0.9 | 2.7887 | 0.4 | 0.7 | 0.8 |
| 120 - 150 | 1.5568 | 0.6 | 0.7 | 0.9 | 0.5449 | 0.5 | 0.7 | 0.9 | 2.7562 | 0.4 | 0.7 | 0.8 |
| 150 - 175 | 1.5028 | 0.7 | 0.7 | 1.0 | 0.5553 | 0.6 | 0.7 | 0.9 | 2.7572 | 0.5 | 0.7 | 0.9 |
| 175 - 200 | 1.4475 | 0.8 | 0.7 | 1.1 | 0.5696 | 0.6 | 0.7 | 0.9 | 2.7671 | 0.5 | 0.7 | 0.9 |
| 200 - 225 | 1.4415 | 1.2 | 0.7 | 1.4 | 0.5779 | 1.0 | 0.7 | 1.2 | 2.7841 | 0.8 | 0.7 | 1.1 |

| Energy [keV] | $\sigma(^{150}Sm)/\sigma(^{197}Au)$ | uncertainty stat | sys | tot | $\sigma(^{152}Sm)/\sigma(^{197}Au)$ | uncertainty stat | sys | tot |
|---|---|---|---|---|---|---|---|---|
| 3 - 5 | 0.5353 | 9.5 | 0.7 | 9.5 | 0.6537 | 7.4 | 0.7 | 7.4 |
| 5 - 7.5 | 0.5561 | 4.5 | 0.7 | 4.5 | 0.5922 | 3.8 | 0.7 | 3.9 |
| 7.5 - 10 | 0.6078 | 3.0 | 0.7 | 3.1 | 0.7036 | 2.6 | 0.7 | 2.7 |
| 10 - 12.5 | 0.5913 | 2.2 | 0.7 | 2.3 | 0.6858 | 1.9 | 0.7 | 2.0 |
| 12.5 - 15 | 0.6783 | 1.9 | 0.7 | 2.0 | 0.7333 | 1.7 | 0.7 | 1.8 |
| 15 - 20 | 0.6667 | 1.1 | 0.7 | 1.3 | 0.7829 | 1.0 | 0.7 | 1.2 |
| 20 - 25 | 0.7700 | 0.9 | 0.7 | 1.1 | 0.8972 | 0.8 | 0.7 | 1.1 |
| 25 - 30 | 0.6610 | 0.8 | 0.7 | 1.1 | 0.8495 | 0.7 | 0.7 | 1.0 |
| 30 - 40 | 0.7089 | 0.6 | 0.7 | 0.9 | 0.8829 | 0.5 | 0.7 | 0.9 |
| 40 - 50 | 0.7781 | 0.6 | 0.7 | 0.9 | 0.8871 | 0.5 | 0.7 | 0.9 |
| 50 - 60 | 0.7840 | 0.5 | 0.7 | 0.9 | 0.9384 | 0.5 | 0.7 | 0.9 |
| 60 - 80 | 0.8134 | 0.4 | 0.7 | 0.8 | 0.9264 | 0.5 | 0.7 | 0.9 |
| 80 - 100 | 0.8946 | 0.4 | 0.7 | 0.8 | 0.9871 | 0.5 | 0.7 | 0.9 |
| 100 - 120 | 0.9048 | 0.5 | 0.7 | 0.9 | 0.9864 | 0.5 | 0.7 | 0.9 |
| 120 - 150 | 0.9625 | 0.5 | 0.7 | 0.9 | 0.8161 | 0.5 | 0.7 | 0.9 |
| 150 - 175 | 0.9808 | 0.5 | 0.7 | 0.9 | 0.6921 | 0.6 | 0.7 | 0.9 |
| 175 - 200 | 1.0100 | 0.6 | 0.7 | 0.9 | 0.6434 | 0.7 | 0.7 | 1.0 |
| 200 - 225 | 1.0279 | 0.9 | 0.7 | 1.1 | 0.6101 | 1.0 | 0.7 | 1.2 |

[a] Energy bins as used for the calculation of the Maxwellian averaged cross sections

**TABLE XXI.** The neutron capture cross section of $^{147}Sm$, $^{148}Sm$, $^{149}Sm$, $^{150}Sm$, and $^{152}Sm$ calculated from the experimental ratios using the gold data from literature [26,27].

| Energy [keV] | σ($^{197}$Au) [mbarn] | σ($^{147}$Sm) [mbarn] | σ($^{148}$Sm) [mbarn] | σ($^{149}$Sm) [mbarn] | σ($^{150}$Sm) [mbarn] | σ($^{152}$Sm) [mbarn] |
|---|---|---|---|---|---|---|
| 3 - 5 | 2266.7 | 3347.3 | 734.3 | 7584.9 | 1213.5 | 1481.9 |
| 5 - 7.5 | 1726.7 | 2461.7 | 587.3 | 5606.5 | 960.1 | 1022.5 |
| 7.5 - 10 | 1215.7 | 2202.6 | 418.1 | 4353.0 | 739.0 | 855.4 |
| 10 - 12.5 | 1066.7 | 1686.4 | 352.2 | 3618.3 | 630.7 | 731.6 |
| 12.5 - 15 | 878.0 | 1622.9 | 330.4 | 3204.0 | 595.5 | 643.8 |
| 15 - 20 | 738.8 | 1281.5 | 280.5 | 2609.5 | 492.6 | 578.4 |
| 20 - 25 | 600.0 | 1121.3 | 262.0 | 2172.4 | 462.0 | 538.3 |
| 25 - 30 | 570.8 | 991.0 | 225.6 | 1821.2 | 377.3 | 484.9 |
| 30 - 40 | 500.4 | 842.9 | 210.6 | 1509.9 | 354.7 | 441.8 |
| 40 - 50 | 433.3 | 734.7 | 197.3 | 1301.7 | 337.2 | 384.4 |
| 50 - 60 | 389.6 | 668.9 | 178.8 | 1139.8 | 305.5 | 365.6 |
| 60 - 80 | 349.4 | 589.1 | 164.9 | 997.2 | 284.2 | 323.7 |
| 80 - 100 | 298.3 | 502.0 | 156.0 | 857.0 | 266.9 | 294.4 |
| 100 - 120 | 290.1 | 477.8 | 153.6 | 809.1 | 262.5 | 286.2 |
| 120 - 150 | 274.1 | 426.8 | 149.4 | 755.6 | 263.9 | 223.7 |
| 150 - 175 | 263.7 | 396.2 | 146.4 | 726.9 | 258.6 | 182.5 |
| 175 - 200 | 252.6 | 365.6 | 143.9 | 698.9 | 255.1 | 162.5 |
| 200 - 225 | 248.5 | 358.2 | 143.6 | 691.7 | 255.4 | 151.6 |

probably due to absorption of water in the samples as it was discussed in Ref. [10]. In more recent experiments, this problem was avoided and consequently better agreement is found. If we normalize the data of Winters et al. [9] in the same way as the present results excellent agreement is found for $^{148}Sm$ and $^{150}Sm$ in the energy range from 15 to 200 keV. However, for $^{149}Sm$ the present data are higher by ~20 % in this range. This discrepancy might be explained by the fact that, as discussed already, $^{149}Sm$ is an isotope with a very high multiplicity of the capture cascades (see Table XI). Consequently, it exhibits a very soft capture gamma-ray spectrum, whereas it is known that the spectrum of gold is comparably hard. Thus recently discovered problems with the weighting function [32] led to a systematic underestimate of the cross section in a relative measurement. It is hard to believe that this effect can cause a difference of 20 %, but one has to keep in mind that discrepancies of this size have also been observed in the opposite direction for the 1.15 keV resonance in iron, where the capture gamma-ray spectrum is known to be extremely hard [33,34]. In the energy range below 15 keV , severe discrepancies were found for all three

**TABLE XXII.** Systematic uncertainties [%].

| | | |
|---|---|---|
| Flight path (cross section ratio): | | 0.1 |
| Neutron flux normalization (cross section ratio): | | 0.2 |
| Sample mass (samarium isotopes): | | 0.2 |
| Isotopic enrichment (samarium isotopes): | | 0.1 |
| Isotopic correction ($^{148}$Sm sample) | | 0.2 |
| Isotopic correction (other Sm samples) | | 0.1 |
| Multiple scattering (cross section ratio) | | 0.2 |
| Unobserved events (cross section ratio Sm/Au) | | 0.6 |
| | (ratio $^{148}$Sm/$^{150}$Sm) | 0.4 |
| total systematic uncertainties: | $\sigma$(Sm)/$\sigma$(Au): | 0.7 |
| | $\sigma(^{148}Sm)/\sigma(^{150}Sm)$ | 0.6 |

isotopes with maximum values up to 30 % at 3 keV. This is due to systematic uncertainties in the subtraction of the scattering background that is problematic in experiments without resolution in gamma-ray energy. Good agreement is found with the recent experiment for $^{147}$Sm and $^{152}$Sm by Bochovko et al. [35], but slight differences in the cross section shape are observed with the tendency that the data are lower compared to the present results at high energy. The unpublished data of Macklin [36] for $^{147}$Sm and $^{149}$Sm are lower by 7 and 10 % , respectively. A recent experiment by Gerstenhöffer [37], using Moxon-Rae detectors, is within the quoted uncertainty of 6 % in good agreement to the present data . In summary, it has to be emphasized that the uncertainties of the present data are significantly lower compared to all previous experiments.

## V. DISCUSSION OF UNCERTAINTIES

The determination of statistical and systematic uncertainties of the present experimental method has been described in Ref. [2,6]. In the following, we briefly consider only new aspects inherent to the present experiment on the samarium isotopes. The individual uncertainties are compiled in Table XXII.

(i) *Background subtraction:* In contrast to the tellurium experiment [6], the large cross sections of the samarium isotopes led to a favorable signal to background ratio . Thus the data could be evaluated down to 3 keV neutron energy. Even assuming a systematic

uncertainty of one percent for the subtracted scattering correction, which is rather conservative, results in a systematic uncertainty in the low energy bins that is still small compared to the statistical uncertainty (see Tables XV to XIX). Therefore, this uncertainty was neglected. This is justified by the fact that very good agreement is found in the shape of the cross section to the data of Bochovko et al. [35].

On the other hand, the experiment of Winters et al. [6], where the same neutron source was used, shows significant deviations in the cross section shape at low energies. Since $C_6D_6$ detectors were used in this experiment, which do not yield information on gamma-ray energy, it was not possible to determine the normalization of the spectrum measured with the carbon sample in dependence of the neutron energy. In Fig. 13 the correction factors are plotted for run I of the present experiment. For easier comparison they are normalized to unity in the energy interval from 50 to 80 keV. From this plot, it is obvious that these corrections depend, indeed, on energy, and are different in shape for the samarium isotopes and the gold standard. Therefore, the assumption of a constant normalization factor made in the work of Ref. [6] must have led to systematic uncertainties at low energies, where the signal to background ratio is small.

(ii) *Flight path:* The flight path was measured several times during the experiment and was found reproducible within ±0.1 mm. Although the sample thickness varied between 0.3 and 2.6 mm, the mean flight path of the samples agreed within ±0.2 mm. Therefore, the uncertainty of 0.1 % quoted in Ref. [2] was found to be a reasonable estimate for the present experiment, too.

(iii) *Sample mass:* The careful analyses of the sample material showed that any water contamination could be excluded when their weight was determined with an uncertainty of 0.17 %. Also no deviations from the assumed stoichiometry could be observed in these analyses. Chemical impurities, mostly due to the rare earth elements neodymium and praseodymium were determined to be less than 0.2 %. Since these isotopes have comparable capture cross sections, a corresponding uncertainty of 0.2 % was assumed for the sample mass.

(iv) *Isotopic enrichment:* In the present experiment, the enrichment of the main isotope was between 95 and 99 %, and isotopic composition quoted by the suppliers was well confirmed by the measurements at KfK (see Table IV). Hence, a systematic uncertainty of 0.1 % is

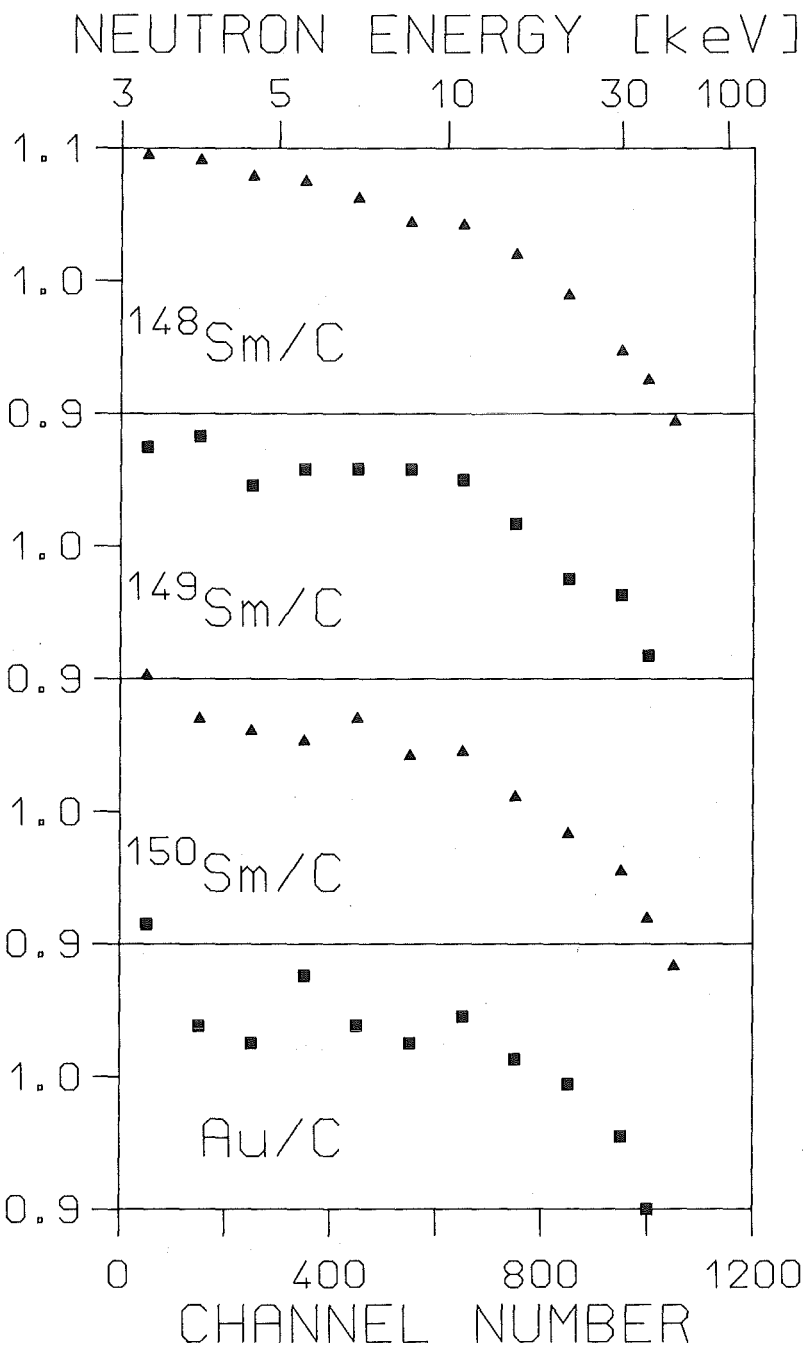


Fig. 13 Ratio of capture events in the scintillator due to neutrons scattered in the different samples and in the graphite sample determined by integrating the two-dimensional spectra in the region around 9 MeV.

assumed for the abundance of the main isotope, respectively. The uncertainties for the isotopic admixtures are negligible, even for the largest corrections in case of the $^{148}$Sm.

(v) *Isotopic correction:* The uncertainty discussed above refers to the number of atoms in the sample m(X) (see equ. 1). An additional uncertainty comes from the fact that part of the count rate $Z_i$ is removed to account for the other isotopes as described in Sec. III.B. In the present experiment, this correction is significant for the even isotopes with a maximum of 8 % at $^{148}$Sm (see Fig. 6). In that case, the 3.6 % isotopic contribution of $^{147}$Sm and $^{149}$Sm carry an uncertainty of 2 %, which results in an uncertainty of 0.2% for the cross section of this isotope. For all other samples, this uncertainty is always less than 0.1 %.

(vi) *Dead-time and pile-up:* Systematic uncertainties correlated with these effects were discussed in Ref. [2], and were found to be negligible.

(vii) *Normalization to equal neutron flux:* The corresponding normalization factors to equal neutron flux are similar to those of the tellurium experiment [6]; therefore, we assume the same systematic uncertainty of 0.2 % for the cross section ratio.

(viii) *Spectrum fraction:* The systematic uncertainty due to the fraction of unobserved capture events, $F_1$ (see equation 1), was discussed in detail in Ref. [2], where a systematic uncertainty of 0.6 % was found. Principally, this discussion is also valid for the present experiment, but with a few improvements. Now, all cascades up to multiplicity 7 were included in the calculations even for the gold sample. Also, the variation of the energy threshold between 0 and 100 keV is irrelevant for capture in the odd samarium isotopes since no transitions below 100 keV are observed in the compound nucleus. Therefore, the previously quoted uncertainty of 0.6 % can also be adopted for the cross section ratios of the samarium isotopes and the gold standard. For the final application of the data in s-process studies (see Sec. VII), where only the cross section ratio $\sigma(^{148}\mathrm{Sm})/\sigma(^{150}\mathrm{Sm})$ is important, this uncertainty is even smaller because the uncertainty due to the gold spectrum cancels out.

The correction $F_1$ is plotted in Fig. 14 versus the difference in binding energy of the respective samarium isotopes and the gold standard. As for the tellurium isotopes, the results show a linear dependence within the quoted uncertainty of 0.6 %, but with a significantly steeper slope. The figure documents that the derived uncertainty is a reasonable estimate.

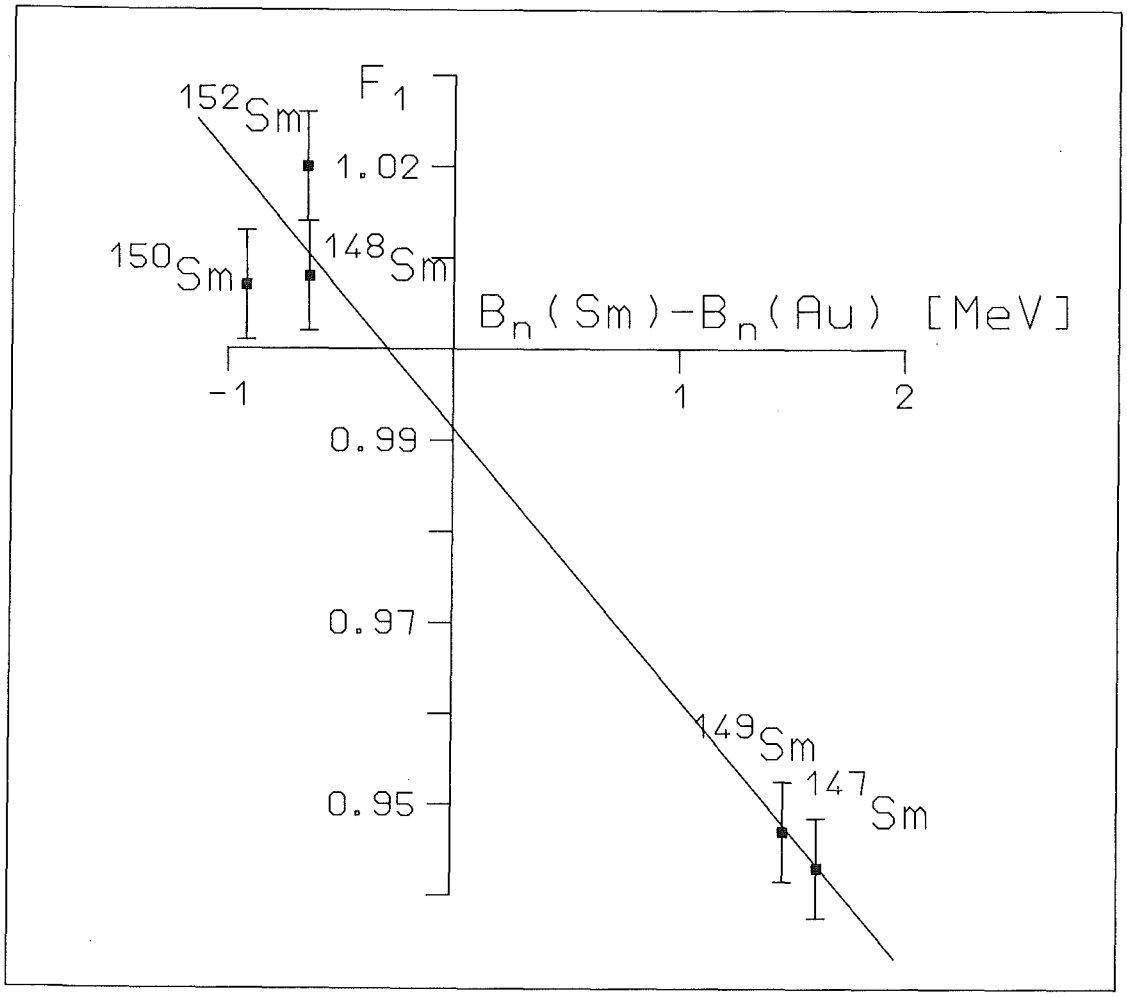


Fig. 14 The correction $F_1$ for unobserved capture events, plotted versus the difference in binding energy between samarium isotopes and the gold standard.

Furthermore, the binding energies of the even samarium isotopes are so similar, that this correction can be completely neglected in calculating the cross section ratio $\sigma(^{148}Sm)/\sigma(^{150}Sm)$ relevant for the astrophysical interpretation. This reduces the uncertainty to 0.4 % according to the slope in Fig. 14.

(ix) *Multiple scattering and self-shielding:* The comparably large cross sections of the samarium isotopes allowed the use of small samples. Consequently, the multiple scattering and self-shielding correction, $F_2$ (see Table XIV) is less than ~1 % for most of the energy range and for all cross section ratios . This is about two to five times smaller than the $F_2$-values for the tellurium isotopes [6]. Since the total cross sections have been determined in this experiment simultaneously with an accuracy of 5 - 10 %, the correlated uncertainties could be reduced by a factor of two.

These estimates of the systematic uncertainties are correct for most of the energy range, but seem somewhat optimistic below ~10 keV neutron energy. In this range, however, the statistical uncertainties are rapidly increasing and dominate the total uncertainty. Thus, an energy-dependent systematic uncertainty for the multiple scattering correction would have no influence in the final results.

(x) *Absorption of water in the samples:* As discussed in Sec.III, the water absorbed at their surface corresponded to 0.2 % of the sample mass. The plastic canning yielded an additional water equivalent of ~0.2 %, but affected the gold reference, too. The respective systematic uncertainties are difficult to estimate, since we are missing an appropriate computer code to follow the moderation effect of this hydrogen contamination. The only quantitative hints come from the work of Mizumoto and Sugimoto [10], who calculated a correction of 17 % at 100 keV neutron energy for a 5.2 % water contamination of a sample that was 2.3 times thicker and 36 times heavier than those of this experiment. According to this comparison and since the effect of the plastic foil cancels out to some extend in the relative measurement, we are sure that the small hydrogen impurity has no noticeable effect on our results.

## VI. MAXWELLIAN AVERAGED CROSS SECTIONS

The Maxwellian averaged cross sections were calculated in the same way as described in Refs. [2] and [38]. The neutron energy range from 0 to 700 keV was divided into three parts according to the cross sections from different sources. The respective contributions $I_x$ are tabulated in Tables XXIII to XXVII. The values $I_2$ were calculated using the cross sections of the present experiment given in Table XXI. The chosen energy bins are fine enough to neglect the correlated systematic uncertainties that may result from a coarse energy grid.

The contributions $I_1$ from the energy range 0 to 3 keV was determined in two different ways. Statistical model calculations were performed and the parameters were adjusted such that the calculated cross sections fitted the data of the present experiment at energies above 3 keV and the data that were calculated from resonance parameters [25] at low energies. In the second calculation we used the cross sections of the Joint Evaluated File [17] which were averaged in the energy range from 0 to 10 keV in 0.5 keV wide bins. These data were normalized to the present experiment in the overlap region from 3 to 10 keV. Though the

**TABLE XXIII.** Maxwellian averaged neutron capture cross sections of $^{147}$Sm. The individual contributions $I_x$ from different energy ranges $\Delta E$ are quoted separately together with their statistical uncertainties $\delta I_x$.

| $\Delta E$: | 0 - 3 keV | | 3 - 225 keV | | 225 - 700 keV | | Total | | | |
|---|---|---|---|---|---|---|---|---|---|---|
| Data: | | | Present Experiment | | from JEF [7] (normalized) | | | | | |
| kT [keV] | $I_1$ [mbarn] | $\delta I_1$ | $I_2$ [mbarn] | $\delta I_2$ | $I_3$ [mbarn] | $\delta I_3$ | $\langle\sigma\rangle$ [mbarn] | $\delta\langle\sigma\rangle$ stat. | syst.[a] | total |
| 10 | 336.1 | 33.6 | 1631.5 | 23.8 | 0.0 | 0.0 | 1967.6 | 41.1 | 13.8 | 43.4 |
| 12 | 241.1 | 24.1 | 1499.3 | 18.7 | 0.0 | 0.0 | 1740.4 | 30.5 | 12.2 | 32.8 |
| 20 | 92.7 | 9.3 | 1156.5 | 9.5 | 0.1 | 0.0 | 1249.3 | 13.3 | 8.7 | 15.9 |
| 25 | 60.5 | 6.0 | 1027.2 | 7.3 | 0.4 | 0.0 | 1088.1 | 9.4 | 7.6 | 12.1 |
| 30 | 42.6 | 4.2 | 931.2 | 6.0 | 1.7 | 0.0 | 975.5 | 7.3 | 6.8 | 10.0 |
| 40 | 24.4 | 2.4 | 793.4 | 4.5 | 8.5 | 0.2 | 826.3 | 5.1 | 5.8 | 7.7 |
| 50 | 15.8 | 1.5 | 693.3 | 3.7 | 21.7 | 0.6 | 730.8 | 4.0 | 5.1 | 6.5 |
| 52 | 14.6 | 1.4 | 675.9 | 3.6 | 25.0 | 0.7 | 715.5 | 3.9 | 5.0 | 6.3 |
| 60 | 11.0 | 1.1 | 613.1 | 3.2 | 39.4 | 1.2 | 663.5 | 3.6 | 4.6 | 5.8 |
| 70 | 8.1 | 0.8 | 545.8 | 2.8 | 59.2 | 2.0 | 613.1 | 3.5 | 4.3 | 5.5 |
| 80 | 6.3 | 0.6 | 488.4 | 2.5 | 79.3 | 2.8 | 574.0 | 3.8 | 4.0 | 5.5 |
| 90 | 5.0 | 0.5 | 438.8 | 2.2 | 98.4 | 3.7 | 542.2 | 4.3 | 3.8 | 5.7 |
| 100 | 4.0 | 0.4 | 395.9 | 2.0 | 115.8 | 4.5 | 515.7 | 4.9 | 3.6 | 6.1 |

[a] The uncertainty of 1.5 % of the gold standard is not included in the systematic uncertainty since it cancels out in most applications of relevance for nuclear astrophysics (see Sec. VII).

**TABLE XXIV.** Maxwellian averaged neutron capture cross sections of $^{148}$Sm. The individual contributions $I_x$ from different energy ranges $\Delta E$ are quoted separately together with their statistical uncertainties $\delta I_x$.

| $\Delta E$: | 0 - 3 keV | | 3 - 225 keV | | 225 - 700 keV | | Total | | | |
|---|---|---|---|---|---|---|---|---|---|---|
| Data: | | | Present Experiment | | from JEF [7] (normalized) | | | | | |
| kT [keV] | $I_1$ [mbarn] | $\delta I_1$ | $I_2$ [mbarn] | $\delta I_2$ | $I_3$ [mbarn] | $\delta I_3$ | $\langle\sigma\rangle$ [mbarn] | $\delta\langle\sigma\rangle$ stat. | syst[a] | total |
| 10 | 60.0 | 6.0 | 360.7 | 5.6 | 0.0 | 0.0 | 420.7 | 8.2 | 2.9 | 8.7 |
| 12 | 42.8 | 4.2 | 336.0 | 4.3 | 0.0 | 0.0 | 378.8 | 6.0 | 2.6 | 6.5 |
| 20 | 16.2 | 1.6 | 274.5 | 2.1 | 0.0 | 0.0 | 290.7 | 2.6 | 2.0 | 3.3 |
| 25 | 10.6 | 1.0 | 252.2 | 1.5 | 0.2 | 0.0 | 263.0 | 1.8 | 1.8 | 2.5 |
| 30 | 7.4 | 0.7 | 236.0 | 1.2 | 0.8 | 0.0 | 244.2 | 1.4 | 1.7 | 2.2 |
| 40 | 4.2 | 0.4 | 212.2 | 0.9 | 3.9 | 0.1 | 220.3 | 1.0 | 1.5 | 1.8 |
| 50 | 2.7 | 0.3 | 193.4 | 0.7 | 10.1 | 0.3 | 206.2 | 0.8 | 1.4 | 1.6 |
| 52 | 2.5 | 0.2 | 189.9 | 0.7 | 11.6 | 0.3 | 204.0 | 0.8 | 1.4 | 1.6 |
| 60 | 1.9 | 0.2 | 176.5 | 0.6 | 18.4 | 0.6 | 196.8 | 0.9 | 1.4 | 1.7 |
| 70 | 1.4 | 0.1 | 161.1 | 0.6 | 27.9 | 0.9 | 190.4 | 1.1 | 1.3 | 1.7 |
| 80 | 1.1 | 0.1 | 146.9 | 0.5 | 37.4 | 1.3 | 185.4 | 1.4 | 1.3 | 1.9 |
| 90 | 0.9 | 0.1 | 134.0 | 0.5 | 46.5 | 1.7 | 181.4 | 1.8 | 1.3 | 2.2 |
| 100 | 0.7 | 0.1 | 122.3 | 0.4 | 54.8 | 2.1 | 177.8 | 2.1 | 1.2 | 2.4 |

[a] The uncertainty of 1.5 % of the gold standard is not included in the systematic uncertainty since it cancels out in most applications of relevance for nuclear astrophysics (see Sec. VII).

**TABLE XXV.** Maxwellian averaged neutron capture cross sections of $^{149}$Sm. The individual contributions $I_x$ from different energy ranges $\Delta E$ are quoted separately together with their statistical uncertainties $\delta I_x$.

| $\Delta E$: | 0 - 3 keV | | 3 - 225 keV | | 225 - 700 keV | | Total | | | |
|---|---|---|---|---|---|---|---|---|---|---|
| Data: | | | Present Experiment | | from JEF [7] (normalized) | | | | | |
| kT [keV] | $I_1$ [mbarn] | $\delta I_1$ | $I_2$ [mbarn] | $\delta I_2$ | $I_3$ [mbarn] | $\delta I_3$ | $\langle\sigma\rangle$ [mbarn] | | $\delta\langle\sigma\rangle$ | |
| | | | | | | | | stat. | syst.[a] | total |
| 10 | 694.3 | 69.4 | 3341.3 | 36.3 | 0.0 | 0.0 | 4035.6 | 78.3 | 28.2 | 83.2 |
| 12 | 494.5 | 49.4 | 3026.1 | 28.1 | 0.0 | 0.0 | 3520.6 | 56.8 | 24.6 | 61.9 |
| 20 | 187.4 | 18.7 | 2232.8 | 13.6 | 0.1 | 0.0 | 2420.3 | 23.1 | 16.9 | 28.6 |
| 25 | 121.8 | 12.1 | 1946.0 | 9.9 | 0.9 | 0.0 | 2068.7 | 15.6 | 14.5 | 21.3 |
| 30 | 85.4 | 8.5 | 1739.7 | 7.8 | 3.3 | 0.1 | 1828.4 | 11.5 | 12.8 | 17.2 |
| 40 | 48.7 | 4.8 | 1456.7 | 5.5 | 16.7 | 0.4 | 1522.1 | 7.3 | 10.7 | 13.0 |
| 50 | 31.4 | 3.1 | 1261.4 | 4.3 | 42.3 | 1.2 | 1335.1 | 5.4 | 9.3 | 10.8 |
| 52 | 29.1 | 2.9 | 1228.4 | 4.2 | 48.6 | 1.4 | 1306.1 | 5.3 | 9.1 | 10.5 |
| 60 | 22.0 | 2.2 | 1110.3 | 3.6 | 76.2 | 2.3 | 1208.5 | 4.8 | 8.5 | 9.8 |
| 70 | 16.2 | 1.6 | 986.3 | 3.1 | 113.7 | 3.7 | 1116.2 | 5.1 | 7.8 | 9.3 |
| 80 | 12.4 | 1.2 | 881.5 | 2.7 | 151.2 | 5.3 | 1045.1 | 6.1 | 7.3 | 9.5 |
| 90 | 9.8 | 1.0 | 791.7 | 2.4 | 186.2 | 6.8 | 987.7 | 7.3 | 6.9 | 10.0 |
| 100 | 8.0 | 0.8 | 714.1 | 2.2 | 217.7 | 8.3 | 939.8 | 8.6 | 6.6 | 10.8 |

[a] The uncertainty of 1.5 % of the gold standard is not included in the systematic uncertainty since it cancels out in most applications of relevance for nuclear astrophysics (see Sec. VII).

**TABLE XXVI.** Maxwellian averaged neutron capture cross sections of $^{150}$Sm. The individual contributions $I_x$ from different energy ranges ΔE are quoted separately together with their statistical uncertainties $\delta I_x$.

| ΔE: | 0 - 3 keV | | 3 - 225 keV | | 225 - 700 keV | | Total | | | |
|---|---|---|---|---|---|---|---|---|---|---|
| Data: | | | Present Experiment | | from JEF [7] (normalized) | | | | | |
| kT [keV] | $I_1$ [mbarn] | $\delta I_1$ | $I_2$ [mbarn] | $\delta I_2$ | $I_3$ [mbarn] | $\delta I_3$ | $\langle\sigma\rangle$ [mbarn] | $\delta\langle\sigma\rangle$ stat. | syst.[a] | total |
| 10 | 121.2 | 12.1 | 621.2 | 9.0 | 0.0 | 0.0 | 742.4 | 15.1 | 5.2 | 16.0 |
| 12 | 86.2 | 8.6 | 578.9 | 6.9 | 0.0 | 0.0 | 665.1 | 11.0 | 4.7 | 12.0 |
| 20 | 32.6 | 3.2 | 472.3 | 3.3 | 0.0 | 0.0 | 504.9 | 4.6 | 3.5 | 5.8 |
| 25 | 21.2 | 2.1 | 433.9 | 2.5 | 0.3 | 0.0 | 455.4 | 3.3 | 3.2 | 4.6 |
| 30 | 14.8 | 1.4 | 406.0 | 2.0 | 1.2 | 0.0 | 422.0 | 2.4 | 3.0 | 3.8 |
| 40 | 8.4 | 0.8 | 365.7 | 1.5 | 6.1 | 0.1 | 380.2 | 1.7 | 2.7 | 3.2 |
| 50 | 5.5 | 0.5 | 333.9 | 1.2 | 15.3 | 0.4 | 354.7 | 1.4 | 2.5 | 2.9 |
| 52 | 5.0 | 0.5 | 328.0 | 1.2 | 17.5 | 0.5 | 350.5 | 1.4 | 2.5 | 2.9 |
| 60 | 3.8 | 0.4 | 305.4 | 1.0 | 27.5 | 0.8 | 336.7 | 1.3 | 2.4 | 2.7 |
| 70 | 2.8 | 0.3 | 279.1 | 0.9 | 41.1 | 1.3 | 323.0 | 1.6 | 2.3 | 2.8 |
| 80 | 2.2 | 0.2 | 254.8 | 0.8 | 54.7 | 1.9 | 311.7 | 2.1 | 2.2 | 3.0 |
| 90 | 1.7 | 0.2 | 232.7 | 0.8 | 67.6 | 2.5 | 302.0 | 2.6 | 2.1 | 3.3 |
| 100 | 1.4 | 0.1 | 212.7 | 0.7 | 79.3 | 3.0 | 293.4 | 3.1 | 2.1 | 3.7 |

[a] The uncertainty of 1.5 % of the gold standard is not included in the systematic uncertainty since it cancels out in most applications of relevance for nuclear astrophysics (see Sec. VII).

**TABLE XXVII.** Maxwellian averaged neutron capture cross sections of $^{152}$Sm. The individual contributions $I_x$ from different energy ranges $\Delta E$ are quoted separately together with their statistical uncertainties $\delta I_x$.

| $\Delta E$: | 0 - 3 keV | | 3 - 225 keV | | 225 - 700 keV | | | Total | | |
|---|---|---|---|---|---|---|---|---|---|---|
| Data: | | | Present Experiment | | from JEF [7] (normalized) | | | | | |
| kT [keV] | $I_1$ [mbarn] | $\delta I_1$ | $I_2$ [mbarn] | $\delta I_2$ | $I_3$ [mbarn] | $\delta I_3$ | $\langle\sigma\rangle$ [mbarn] | $\delta\langle\sigma\rangle$ stat. | syst.[a] | total |
| 10 | 161.2 | 16.1 | 721.2 | 8.6 | 0.0 | 0.0 | 882.4 | 18.3 | 6.2 | 19.3 |
| 12 | 114.3 | 11.4 | 674.6 | 6.7 | 0.0 | 0.0 | 788.9 | 13.2 | 5.5 | 14.3 |
| 20 | 42.9 | 4.3 | 551.2 | 3.3 | 0.0 | 0.0 | 594.1 | 5.4 | 4.2 | 6.8 |
| 25 | 27.8 | 2.8 | 502.1 | 2.5 | 0.2 | 0.0 | 530.1 | 3.8 | 3.7 | 5.3 |
| 30 | 19.4 | 1.9 | 463.6 | 2.0 | 0.7 | 0.0 | 483.7 | 2.8 | 3.4 | 4.4 |
| 40 | 11.1 | 1.1 | 403.7 | 1.5 | 3.8 | 0.1 | 418.6 | 1.9 | 2.9 | 3.5 |
| 50 | 7.1 | 0.7 | 356.1 | 1.3 | 9.5 | 0.3 | 372.7 | 1.5 | 2.6 | 3.0 |
| 52 | 6.6 | 0.6 | 347.5 | 1.2 | 11.0 | 0.3 | 365.1 | 1.4 | 2.6 | 3.0 |
| 60 | 5.0 | 0.5 | 316.0 | 1.1 | 17.3 | 0.5 | 338.3 | 1.3 | 2.4 | 2.7 |
| 70 | 3.7 | 0.4 | 281.5 | 0.9 | 26.0 | 0.8 | 311.2 | 1.3 | 2.2 | 2.6 |
| 80 | 2.8 | 0.3 | 251.6 | 0.8 | 34.7 | 1.2 | 289.1 | 1.5 | 2.0 | 2.5 |
| 90 | 2.2 | 0.2 | 225.8 | 0.7 | 43.0 | 1.6 | 271.0 | 1.8 | 1.9 | 2.6 |
| 100 | 1.8 | 0.2 | 203.3 | 0.7 | 50.5 | 1.9 | 255.6 | 2.0 | 1.8 | 2.7 |

[a] The uncertainty of 1.5 % of the gold standard is not included in the systematic uncertainty since it cancels out in most applications of relevance for nuclear astrophysics (see Sec. VII).

respective normalization factors were ranging from 0.864 to 1.229, the shape of both data sets was found in good agreement except for $^{147}$Sm. That results from the second calculation were systematically higher may be due to the fact that the cross sections calculated from resonance parameters are underestimating the true cross section because of missing resonances. The final data given in Tables XXIII to XXVII are the average of both calculations with agreed in general within the quoted uncertainty of 10 %.

The energy interval from 225 to 700 keV, that contributes only very little to the Maxwellian average at typical s-process temperatures was covered by normalizing again the JEF data to the present experiment in the energy interval from 100 to 200 keV. The quoted uncertainties were calculated under the assumption that the uncertainty of the normalized cross sections increases from 2 % at 225 keV to 10 % at 700 keV.

The systematic uncertainty of the Maxwellian averaged cross section given in Tables XXIII to XXVII corresponds to the uncertainty of the cross section ratio (see Table XXII); it considers the contributions of the summed intensity, $I_2+I_3$ . The 1.5 % uncertainty of the gold standard was not included since it cancels out in most applications of relevance for s-process studies (see Sec. VII ). The total uncertainties are given in the last column; for thermal energies between 30 and 70 keV they are dominated by the systematic contributions. We note that in determining ratios, e.g. $\langle\sigma\rangle(^{148}Sm)/\langle\sigma\rangle(^{150}Sm)$ , it is not allowed to add the uncertainties given in Tables XXIII and XXVII quadratically, because they are strongly correlated. For example, the statistical uncertainties of the cross section ratios are partly determined by the count rate in the gold spectra ( $Z_I$(Au), $\Sigma$Z(Au), $\Sigma$E(Au) in Eq.1) which cancels out in the cross section ratio of two samarium isotopes. The same holds for the systematic uncertainties for multiple scattering and for the spectrum fraction of the gold sample. The proper uncertainty of the ratio of Maxwellian averaged cross sections of two samarium isotopes was evaluated explicitly for the s-only isotopes $^{148}$Sm and $^{150}$Sm, and was found to be ~30 % lower than expected from a quadratic summation (Table XXVIII).

If the present results at kT=30 keV are compared with the data given in the compilation of Bao and Käppeler [11], one finds the same discrepancies as discussed above. That our data for $^{148}$Sm and $^{150}$Sm are lower by 9 and 6 % compared to the results of Winters et al. [9] are somewhat surprising in view of the good agreement in the energy range from 15 to 200 keV; indicating the significant contribution of the low energy region to the Maxwellian

**TABLE XXVIII.** The ratio of the Maxwellian averaged neutron capture cross sections of $^{148}Sm$ and $^{150}Sm$ and the correlated uncertainty.

| kT | $\langle\sigma\rangle(^{148}Sm)/\langle\sigma\rangle(^{150}Sm)$ |
|---|---|
| 10 | 0.567 ± 2.8 % |
| 12 | 0.570 ± 2.3 % |
| 20 | 0.576 ± 1.4 % |
| 25 | 0.578 ± 1.1 % |
| 30 | 0.579 ± 1.0 % |
| 40 | 0.579 ± 0.8 % |
| 50 | 0.581 ± 0.8 % |
| 52 | 0.582 ± 0.8 % |
| 60 | 0.585 ± 0.8 % |
| 70 | 0.589 ± 0.9 % |
| 80 | 0.595 ± 1.1 % |
| 90 | 0.601 ± 1.4 % |
| 100 | 0.606 ± 1.7 % |

average. It should be noted, however, that the ratio $\langle\sigma\rangle(^{148}Sm)/\langle\sigma\rangle(^{150}Sm)$, the quantity of astrophysical importance is in agreement at kT=30 keV within the quoted uncertainties . In any case, the uncertainty of this ratio has been improved by a factor of 4 by the present results.

It is also interesting to see the good agreement with to the pioneering work of Macklin and Gibbons [39], who were the first to measure these samarium cross sections about 30 years ago. Their results are given with uncertainties of 15 to 20 %, but within these limits the data agree for all five measured isotopes with the present values. The result of Beer et al.[40] obtained in an activation experiment for $^{152}Sm$ is significantly lower than the present value.

## VII. IMPLICATIONS FOR THE CLASSICAL s-PROCESS AND FOR A STELLAR MODEL

With the accurate (n,γ)-cross sections of the samarium isotopes of the present work, three aspects of s-process nucleosynthesis can be improved: The reaction flow in the s-process is expressed by the smooth $\langle\sigma\rangle N_s(A)$-curve, and can be normalized to the corresponding empirical product for $^{150}$Sm, since this isotope experiences the entire s-process flow. Together with a similar normalization point at $^{124}$Te, which has been investigated in a previous study [6], it is now possible to define the step-like decrease of the $\langle\sigma\rangle N_s$-curve at the neutron magic nuclei with N = 82 - and hence the mean neutron exposure, $\tau_0$, with better reliability. The second aspect concerns the information on neutron density, which can be inferred from the s-process branchings at A = 147, 148, and 149. The strength of these branchings is reflected by the $\langle\sigma\rangle N_s$-ratio of $^{148}$Sm and $^{150}$Sm (see Fig. 1). Since the abundance ratio is practically given by the isotopic ratio of the two nuclei, the present cross sections allow for an improved value for the neutron density in the s-process, which is the determining parameter in these branchings. Finally, the present data can be used for testing the neutron density and temperature profiles predicted by a stellar model for helium shell burning in low mass stars, that originates from the work of Iben and Renzini [41] and Hollowell and Iben [42, 43], and that has been used successfully for nucleosynthesis studies by Gallino et al. [3, 4, 44].

### A. NORMALIZATION OF THE $\langle\sigma\rangle N_s$-CURVE

The discussion in this and the next subsection refers to the classical approach for the s-process. The general formalism and the respective terminology have been outlined in Ref. [5], and the particular problem of the Nd - Pm - Sm region was addressed in full detail in Ref. [9]. Therefore, the discussion will be restricted here to the most essential features.

For A > 90, the mass flow along the s-process nucleosynthesis path between iron and bismuth is dominated by the so-called main component. This main component was found to be the result of an exponential distribution of neutron exposures, $\rho(\tau)$, to which a fraction G of the observed iron abundance, $N_\odot$, was exposed. For this main component, one obtains

$$\langle\sigma\rangle N_s(A) = \frac{G\, N_{Fe,\odot}}{\tau_0} \prod_{i=56}^{A} \left(1 + \frac{1}{\langle\sigma\rangle_i \cdot \tau_0}\right)^{-1},$$

where the free parameters are determined by a least square fit to the emprical $\langle\sigma\rangle N_s$ values of all s-only nuclei that are experiencing the entire s-process flow, which means that they are not bypassed by a significant branching in the synthesis path. In this fit, the uncertainties of the respective $\langle\sigma\rangle N_s$ values are to be considered. The relative contributions from the observed abundances vary from < 2 % for the lanthanides up to ~10 % for more volatile elements [45]. In practically all cases, the respective cross section uncertainties are comparable or lower. Since there are about 10 such normalization points for fitting only two parameters, the system is overdetermined and the problem of uncertainties is correspondingly reduced. So far, the mean exposure was determined in Ref. [3] to

$$\tau_0 = (0.306 \pm 0.010) \left(\frac{kT\ [keV]}{30}\right)^{1/2} \text{ mbarn}^{-1} .$$

With the availability of cross sections that are accurate to ±1 %, it will be possible to improve the fit of the normalization points on the $\langle\sigma\rangle N_s$ curve correspondingly. The first two nuclei in this category are $^{124}$Te [6] and $^{150}$Sm, one below and the other above the step in the $\langle\sigma\rangle N_s$ curve at N = 82. Since the mean neutron exposure, $\tau_0$, is most sensitive to the height of this step, these two isotopes were sufficient to derive an improved value for $\tau_0$, if the Te and Sm abundances were sufficiently accurate. The mean exposure that results from the $\langle\sigma\rangle N_s$ values of $^{124}$Te and $^{150}$Sm alone is

$$\tau_0 = 0.297 \pm 0.009 \text{ mbarn}^{-1},$$

in excellent agreement with the value of Ref. [6]. However, the uncertainty assigned to the Te abundance is 10 % [45]. Therefore, the only conclusion to be be drawn at this point is that the uncertainty of the Te abundance may have been overestimated in Ref. [45], and could be reduced to about 3 % according to the observed $\langle s\rangle N_s$ systematics.

## B. THE s-PROCESS NEUTRON DENSITY

As illustrated in Fig. 1, the s-process path in the Nd - Pm - Sm region exhibits branchings due to the competition between neutron captures and beta decays at $^{147}$Nd and at the Pm-isotopes. The combined strength of these branchings manifests itself in the difference of the $\langle\sigma\rangle N_s$ values of $^{148}$Sm (which is partly bypassed) and $^{150}$Sm (which experiences the entire s-process flow). The respective branching factors

$$f_- = \frac{\lambda_\beta}{\lambda_\beta + \lambda_n}$$

can schematically be combined to an effective factor that is expressed by

$$f_{-}^{eff} = \frac{\langle\sigma\rangle N_s(^{148}Sm)}{\langle\sigma\rangle N_s(^{150}Sm)} \quad .$$

Since the beta decay rates, $\lambda_\beta = \ln 2/t_{1/2}$, of the branching points in Fig. 1 are practically not affected by temperature, the set of equations summarized in the above expressions (for an explicit delineation see Ref. [9]) can be solved for the neutron capture rate $\lambda_n = \langle\sigma\rangle \cdot v_T \cdot n_n$ in order to obtain an estimate for the s-process neutron density, $n_n$.

Compared to the previous result of Winters et al. [9] (0.92 ± 0.04), the present measurement yields a considerably improved value of

$$f_{-}^{eff} = 0.882 \pm 0.009,$$

with a 4 times smaller uncertainty. Adopting all other quantities from Ref. [9] and considering complete thermal equilibrium in the population of isomer and ground state in $^{148}$Pm [3], one arrives at a neutron density

$$n_n = (3.4 \pm 0.6) \cdot 10^8 \text{ cm}^{-3},$$

in excellent agreement with the result of Ref. [3], where $(3.4 \pm 1.1) \cdot 10^8$ cm$^{-3}$ were reported. At this level of accuracy, p-process corrections may no longer be negligible. Since quantitative p-process models are still missing, such a correction can best be made by the semi-empirical estimates of the p-corrections to the abundances of s-only isotopes proposed by Beer [46]. For $^{148}$Sm and $^{150}$Sm, these corrections are 1.1 and 1.7 %, respectively, leading to a marginal effect in the result for the neutron density ( $n_n = (3.5 \pm 0.6) \cdot 10^8$ cm$^{-3}$ ).

A remaining uncertainty concerns the (n,γ) cross sections of the unstable promethium isotopes. Recently, the capture cross section of $^{147}$Pm has been measured for the first time [37]. Despite of several difficulties, un uncertainty of 15 % could be claimed for this cross section, which was a factor of 2 smaller than the existing statistical model calculation in Ref. [9]. Using this new cross section results in a rather small change of the neutron density, yielding $n_n = 3.8 \cdot 10^8$ cm$^{-3}$. However, this discrepancy rises a more severe problem, since it questions the reliabilty of the cross section calculation in the vicinity of the closed neutron shell with N = 82 in general. If, for instance, the cross sections for the other promethium cross sections were scaled by the same factor of 2, the neutron density would rise to $5.1 \cdot 10^8$ cm$^{-3}$! Therefore, it will be necessary to verify this cross section measurement of $^{147}$Pm and to study the parameter space used in the statistical model calculations in more detail, as well.

## C. COMPARISON TO A STELLAR MODEL

The stellar model that has been shown to reproduce the s-process abundances quite well [3, 4, 41 - 44], refers to helium shell burning in low mass stars with about 1/3 of the solar metallicity. In this scenario, relatively short helium burning episodes, where neutrons are released in $(\alpha,n)$ reactions on $^{13}C$ and $^{22}Ne$ alternate with much longer periods when the consumed helium is replenished by hydrogen burning. An exponential distribution of neutron exposures is achieved in this model by the fractional overlap of zones containing freshly synthesized material. (For a detailed discussion see the references quoted above).

Effective neutron density and temperature profiles during the helium burning episodes have been deduced from the more detailed model [47] and were used with the network code NETZ [48] to follow the s-process flow in the entire mass region from Fe to Bi. On average, the s-only isotopes are well reproduced for $A > 90$ in this calculation. However, with the accurate cross sections now available for the tellurium and samarium isotopes, significant discrepancies are emerging in the calculated abundance patterns of the respective branchings. In the present case, the model yields an overproduction of 6 % for $^{148}Sm$, corresponding to 6 standard deviations in terms of the cross section uncertainty. Since this discrepancy is also not very sensitive to the above mentioned problem of the promethium cross sections, it may be a hint that the neutron density is underestimated by the model. In view of these problems, it will be interesting to see the results of current attempts to improve this picture for helium shell burning in low mass stars [47] or to search for alternative possibilities for a stellar s-process scenario [49].

## VIII. CONCLUSIONS

This second application of the Karlsruhe $4\pi$ $BaF_2$ Detector confirmed the possibility for determining differential neutron capture cross sections in the range of astrophysical interest with an accuracy of $\pm 1$. It was the intention of this report, to discuss all difficulties and possible pitfalls thoroughly and to present in great detail the approaches and solutions of the present work in order to justify the achieved accuracy. This report will, therefore, be the extended version of a later publication that must necessarily be more concise.

In this investigation, the $(n,\gamma)$ cross sections were measured for a sequence of samarium isotopes, which define the s-process branchings at A = 147, 148, 149. The measurement was carried out on $^{147}Sm$, $^{148}Sm$, $^{149}Sm$, $^{150}Sm$, and $^{152}Sm$ and covered the energy range

from 3 to 225 keV. It was performed in different runs with modified experimental parameters. The good agreement in the respective regions of overlap is an important confirmation for the evaluation of corrections and systematic uncertainties. A novelty in the present measurement was the implementation of an ADC system for analysing energy and time-of-flight information for each individual detector module. In this way, background corrections were improved and additional information was obtained on the energy spectrum and multiplicity of the capture gamma-ray cascades.

As in the previous experiment on the tellurium isotopes [6], a considerable effort was made for a reliable characterization of the samples. Careful preparations and repeated analyses were found to be important in order to eliminate water contamination and to define sample mass and stoichiometry. Otherwise, significant effects could not be excluded; possibly, part of the discrepancies between the present data and previous results may have to do with this type of problems. Another reason for these discrepancies might result from the very high gamma-ray multiplicity observed in the odd isotopes. Accordingly, these isotopes exhibit a very soft gamma-ray spectrum, in contrast to the much harder spectrum of gold. Therefore, this difference may have caused a problem in measurements using the pulse height weighting technique.

The Maxwellian averaged cross sections that were calculated from the differential data are of twofold importantance for s-process nucleosynthesis. First, $^{150}$Sm represents one of the major normalization points for the definition of the $\langle\sigma\rangle N_s$ curve, and hence of the s-process abundance distribution. Secondly, the strength of the s-process branchings at A = 147, 148, and 149 can be quantified by comparison of the $\langle\sigma\rangle N$ values of the s-only pair $^{148}$Sm and $^{150}$Sm. Therefore, the accurate determination of the cross section ratio for these two nuclei removed the main uncertainty in the s-process neutron density, allowing for a significantly improved estimate of the neutron density via the classical approach. In addition, the new cross sections can also be used as a sensitive test for the neutron density profile provided by stellar s-process models.

These studies have shown that more work is required to investigate the remaining uncertainties. The main problem results from the discrepancy between a recent measurement of the $(n,\gamma)$ cross section of one of the unstable branch point nuclei, $^{147}$Pm, and the existing calculations based on the statistical model. On the other hand, more work is certainly required on the stellar models to understand the present difficulty in reproducing the abundance pattern in the samarium isotopes correctly.

## IX. REFERENCES


[1] K. Wisshak, K. Guber, F. Käppeler, J. Krisch, H. Müller, G. Rupp, and F. Voß, Nucl. Instr. Meth. **A292**, 595 (1990).

[2] K. Wisshak, F. Voß, F. Käppeler, and G. Reffo, Phys. Rev. **C42**, 1731 (1990) and report KfK-4674 Kernforschungszentrum Karlsruhe 1990.

[3] F. Käppeler, R. Gallino, M. Busso, G. Picchio, and C.M. Raiteri, Astrophys. J. **354**, 630 (1990).

[4] R. Gallino, M. Busso, G. Picchio, C.M. Raiteri, and A. Renzini, Astrophys. J. **334**, L45 (1988).

[5] F. Käppeler, H. Beer, and K. Wisshak, Rep. Prog. Phys. **52**, 945 (1989).

[6] K. Wisshak, F. Voss, F. Käppeler, and G. Reffo, Phys. Rev. **C45**, 2470 (1992) and report KfK-4899, Kernforschungszentrum Karlsruhe 1991.

[7] D.D. Clayton, W.A. Fowler, P.E. Hull, and B.A. Zimmerman, Ann. Phys. **12**, 331 (1961).

[8] N. E. Holden, R.L. Martin, and I.L. Barnes, Pure Appl. Chem. **56**, 675 (1984). and IUPAC International Union of Pure and Applied Chemistry, Pure Appl. Chem. **63**, 991 (1991).

[9] R.R. Winters, F. Käppeler, K. Wisshak, A. Mengoni, and G. Reffo, Astrophys. J. **300**, 41 (1986).

[10] M. Mizumoto and M. Sugimoto, Nucl. Instr. Meth. **A282**, 324 (1989).

[11] Z.Y. Bao and F. Käppeler At. Data Nucl. Data Tables **36**, 411 (1987).

[12] K. Guber Thesis university of Karlsruhe 1993 unpublished.

[13] K. Guber, K. Wisshak, F. Voss, and F. Käppeler, Nucl. Instrum. Methods submitted

[14] G. Winkler, Nucl. Instr. Meth. **A282**, 317 (1989)

[15] H. Ottmar, H. Eberle, L. Koch, R. de Meester, and E. Kuhn, Proc. Int. Symp on Nuclear Material Safeguards Vienna 10-14 Nov.1986, International Atomic Energy Agency, Vienna 1987. p 201.

[16] R. de Meester, H. Eberle, S. Johnson, L. Koch, I. Michel-Piper, H. Nackaerts, and H. Ottmar, Proc. Int. Symp on Nuclear Material Safeguards Vienna 10-14 Nov.1986, International Atomic Energy Agency, Vienna 1987, p 233.

[17] C. Nordborg, H. Gruppelaar, and M. Salvatores, Proc. Int. Conf. on Nuclear Data for Science and Technology, Jülich, Germany, 13-17 may 1991, p 782.

[18] V. McLane, C.L. Dunford, and P.F. Rose, Neutron Cross Sections (Academic , New York, 1988) Vol. 2.

[19] K.K. Seth, Phys. Let. **16**, 306 (1965).

[20] G. Reffo, F. Fabbri, K. Wisshak, and F. Käppeler, Nucl. Sci. Eng. **80**, 630 (1982).

[21] K. Wisshak, F. Käppeler, and G. Schatz, Nucl. Instr. Meth. **221**, 385 (1984).

[22] H.J. Gils, D. Heck, J. Oehlschläger, G. Schatz, T. Thouw, and A. Merkel, Computer Physics Communications **56**, 105 (1989).

[23] F.H. Fröhner, SESH- A Fortran IV Code for Calculating the Self-Shielding and Multiple Scattering Effects for Neutron Cross Section Data Interpretation in the Unresolved Resonance Region, report GA-8380, Gulf General Atomic (1968).

[24] A. Gilbert and A.G.W. Cameron, Can. J. of Phys. **43**, 1446 (1965).

[25] S.F. Mughabghab, M. Divadeenam, and N.E. Holden, Neutron Cross Sections, (Academic Press, New York, 1981). Vol. 1, Part A.

[26] R.L. Macklin, private communication (1982)

[27] W. Ratynski and F. Käppeler, Phys. Rev. C **37**, 595 (1988).

[28] M. Mizumoto, Nucl. Phys. **A357**, 90 (1981).

[29] R.A. Shaw, W.R. Koste, and R.W. Hockenbury, unpublished.

[30] V.N. Kononov, B.D. Yurlov, G.E. Manturov, E.D. Poletaev, and V.M. Timokhov, Yad. Fiz. **26**, 947 (1977).

[31] V.N. Kononov, B.D. Yurlov, E.D. Poletaev, and V.M. Timokhov, Yad. Fiz. **27**, 10 (1978).

[32] F. Corvi, A. Prevignano, H. Liskien, and P.B. Smith, Nucl. Instr. Methods **A265**, 475 (1988).

[33] R.L. Macklin, Nucl. Sci. Eng., **83**, 309 (1983).

[34] R.L. Macklin, Nucl. Sci. Eng., **95**, 200 (1987).

[35] M.W. Bochovko, A.A. Woewodskij, V.N. Kononov, T.N. Manturov, E.D. Poletaev, and V.M. Timokhov, report FEI-2168, Fiziko Energetscheskij Institut, Obninsk 1991.

[36] R.L. Macklin, unpublished (EXFOR 12966.003 and .004).

[37] T.W. Gerstenhöfer, Thesis, University of Heidelberg 1992, unpublished.

[38] H. Beer, F. Voss, and R.R. Winters, Astrophys. J. Suppl. **80**, 403 (1992).

[39] R.L. Macklin and J.H. Gibbons, Astrophys. J. **149**, 577 (1967).

[40] H. Beer, F. Käppeler, K. Yokoi, and K. Takahashi, Astrophys. J. **278**, 388 (1984).

[41] I. Iben, Jr. and A. Renzini, Astrophys. J. **259**, L79 (1982) and **263** L23 (1982).

[42] D. E. Hollowell and I. Iben, Jr., Astrophys. J. **333**, L25 (1988).

[43] D. E. Hollowell and I. Iben, Jr., Astrophys. J. **340**, 966 (1989).

[44] R. Gallino, M. Busso, and C.M. Raiteri, in *Nuclei in the Cosmos '92*, ed. F. Käppeler and K. Wisshak (Bristol: IOP) in print.

[45] E. Anders and N. Grevesse, Geochim. Cosmochim. Acta **53**, 197 (1989).

[46] H. Beer, Kernforschungszentrum Karlsruhe, internal report (1985), unpublished.

[47] R. Gallino, private communication (1992).

[48] S. Jaag, Diplom thesis, University of Karlsruhe (1990).

[49] I.-J. Sackmann, private communication (1992).

## X. ACKNOWLEDGMENTS

The present work profited by the help of many collegues from KfK. In particular we would like to thank Ch. Adelhelm, G. Streib and M. Mackert from the Institute of Material Research for their careful analyses of the water and samarium content of the samples. We also appreciated the spontaneous help of E. Gantner, H. Deutsch and H. Klewe-Nebenius from the Institute of Radiochemistry who determined the isotopic composition. We have to thank F.H. Fröhner and B. Krieg from the Institute of Neutron Research who provided us with the data from the JEF evaluation. We greatfully acknowledge the analyses by K X-ray absorptiometry by H. Ottmar and H. Eberle as well as the calculations with the transputer system by J. Oehlschläger. The Van de Graaff crew, D. Roller, E.-P. Knaetsch and W. Seith did a great job in keeping the accelerator running at optimum conditions. Last not least, the continuous support of G. Rupp in optimizing the experimental setup is greatfully acknowledged.